

Hard X-ray microtomography for virtual histology of the brain with cellular resolution

Inauguraldissertation

zur

Erlangung der Würde eines Doktors der Philosophie
vorgelegt der

Philosophisch-Naturwissenschaftlichen Fakultät
der Universität Basel

von

Griffin Rodgers

Basel, 2021

Originaldokument gespeichert auf dem Dokumentenserver der Universität Basel edoc.unibas.ch

Genehmigt von der Philosophisch-Naturwissenschaftlichen Fakultät

auf Antrag von:

Prof. Dr. Bert Müller, Erstbetreuer
Prof. Dr. Ernst Meyer, Zweitbetreuer
Prof. Dr. Julia Herzen, externe Expertin

Basel, den 19. Oktober 2021

Prof. Dr. Marcel Mayor, Dekan

Contents

Summary	v
Zusammenfassung	vii
List of Publications	ix
1 Introduction	1
Magnetic resonance imaging	1
Optical microscopy and conventional histology	1
Electron microscopy	2
X-ray virtual histology	2
Towards brain atlases with X-ray virtual histology	4
Contributions	7
2 Optimizing spatial and density resolution for X-ray virtual histology	9
3 Impact of fixation and paraffin embedding on mouse brain morphology and X-ray contrast	15
Part 1: Data acquisition, anatomical feature segmentation, tracking global volume and density changes	16
Part 2: Volumetric strain fields and local contrast changes	27
4 X-ray virtual histology for the investigation of temporal lobe epilepsy in a mouse model	39
Manuscript in preparation	39
4.1 Abstract	39
4.2 Introduction	40
4.3 Materials and methods	41
4.3.1 Animals and kainate injection	41
4.3.2 Tissue preparation	41
4.3.3 Synchrotron radiation-based microtomography	41
4.3.4 Immunohistochemistry and histology	42
4.3.5 Segmentation and rendering of the volumetric data	42
4.4 Results	43
4.4.1 Visualizing pathological changes associated with epilepsy	43
4.4.2 Comparing virtual histology with histology and immunohistochemistry	45
4.4.3 Volume and density changes associated with the progression of mTLE	46
4.5 Discussion	50
4.6 Conclusion	51
4.7 Acknowledgements	52

5	Microtomography of the entire mouse brain with sub-micrometer voxels	53
5.1	Introduction	53
5.2	Materials and methods	54
5.2.1	Animals and tissue preparation	54
5.2.2	Extended-field microtomography acquisition	55
5.2.3	Reconstruction of mosaic-style tomography data	55
5.3	Results and discussion	61
5.4	Conclusion	64
5.5	Acknowledgements	64
6	Conclusions and Outlook	67
	Bibliography	69
	Acknowledgments	81
	Curriculum Vitae	83

Summary

Mammalian brains are extremely complex: even the rather small mouse brain contains around one hundred million neurons. Mapping the three-dimensional cytoarchitecture from the nanometer- to centimeter-scale within the context of the entire brain is a key step towards understanding brain function. This thesis presents developments in neuroimaging with virtual histology based on hard X-ray microtomography. This emerging technique holds great promise for non-destructive three-dimensional analysis of centimeter-sized *post mortem* brain tissue with true micrometer resolution.

The brain is composed of soft tissue with inherently low contrast for absorption-based X-ray imaging. Phase contrast has been suggested to boost contrast by several orders of magnitude. The most common method is single-distance phase retrieval by Fourier-space filtering. The trade-off between spatial resolution and contrast-to-noise ratio was characterized for Paganin's widespread phase retrieval and simple Gaussian filtering for synchrotron radiation-based microtomography. Both provided substantial contrast gains at the expense of spatial resolution. Surprisingly, Gaussian filtering outperformed Paganin filtering at equal spatial resolution. *A priori* information was not known and model assumptions for single-distance phase retrieval such as monochromaticity and sample homogeneity were violated for the measured soft tissues. Therefore, filter selection should be based on an image quality factor to optimize both contrast and spatial resolution.

Conventional histology requires fixation and embedding of *post mortem* brain tissue. Performing virtual histology at an intermediary preparation step allows for subsequent validation and a combination the two modalities. However, preparation changes tissue composition and generates inhomogenous shrinkage. Virtual histology datasets of an entire mouse brain at each step of preparation were non-rigidly registered to characterize volumetric strain fields and compare X-ray contrast of corresponding anatomical features. Brain volume changed by -40% and -60% from formalin-fixed to ethanol dehydrated and paraffin embedded, respectively. Volumetric strain fields depended on both anatomical boundaries and distance to the brain's surface, for example the cerebral cortex volume changed by -55% and -75% while the thalamus changed by -25% and -45% for ethanol dehydration and paraffin embedding, respectively. Selection of preparation provides differential tissue contrast, for example fiber tracts are enhanced through ethanol dehydration while the cerebellum has high inter-layer contrast when paraffin embedded.

Virtual histology can also reveal structural changes caused by neurological disorders. Epilepsy is among the most prevalent neurological disorders, with mesial temporal lobe epilepsy (mTLE) the most common form among adults. The three-dimensional pathological changes are poorly accessible with magnetic resonance imaging or conventional histology. Synchrotron radiation-based phase contrast microtomography of kainate induced mTLE in a mouse model allowed for the identification of hippocampal sclerosis. The polymorph, granular, and molecular layers of the dentate gyrus were segmented for a unique quantification of morphological changes during epileptogenesis. Granule cell dispersion was associated with an increase in granule

cell layer volume from 2.9 to $11.4 \times 10^{-3} \text{ mm}^3$. Thus, virtual histology complements gold standard conventional histology by providing three-dimensional, cellular resolution histopathological analysis for mTLE.

For microtomography with $0.65 \mu\text{m}$ pixel size, field-of-view (FOV) is typically limited to about 2.2 mm^3 . FOV must to be significantly extended for full brain mapping, e.g. to 450 mm^3 for a mouse brain. Mosaic tiling of multiple FOVs has been demonstrated based on a dedicated pipeline to process these tera-voxel sized datasets. Here, the entire mouse brain was imaged with $0.65 \mu\text{m}$ -wide voxels. The datasets, which are 6 TB in size at 16-bit depth, contain a wealth of microanatomical information but present challenges for registration and segmentation. The question arises: can virtual histology be used to visualize the 3000 times larger entire human brain at $1 \mu\text{m}$ resolution?

Zusammenfassung

Die Gehirne der Säugetiere haben eine komplexe anatomische Struktur – selbst das relativ kleine Mäusehirn umfasst etwa 100 000 000 Neuronen. Die Abbildung der dreidimensionalen Zellarchitektur in der entsprechenden Umgebung über Längenskalen vom Nano- zum Zentimeter ist wesentlich für das Verständnis der Hirnfunktion. Die vorliegende Arbeit stellt Entwicklungen zur Neurobildgebung mittels virtueller Histologie vor, die sich auf Mikrotomographie mit harten Röntgenstrahlen gründet. Diese neu entstehende Technik verspricht die zerstörungsfreie, dreidimensionale Untersuchung von totem, zentimetergroßem Hirngewebe mit Mikrometerauflösung.

Aufgrund seiner chemikalischen Zusammensetzung liefert das Hirn kaum Absorptionskontrast. Der Vorteilsfaktor der Phasenmessung in Bezug auf den Kontrast beträgt etwa 1 000. Deshalb wird heute häufig die sogenannte Methode der Phasenrückgewinnung mittels Filter im Fourier-Raum eingesetzt. Die vorliegende Arbeit nutzt Paganin's Algorithmus und den Gauss-Filter, um Ortsauflösung und das Signal-Rausch-Verhältnis auszutarieren. Beide Ansätze verstärken den Kontrast auf Kosten der Ortsauflösung. Für das menschliche Gehirn findet man bei vergleichbarer Ortsauflösung erstaunlicherweise einen besseren Kontrast unter Verwendung des Gaussfilters. Erfahrungsabhängige Informationen und Modellannahmen für die Phasenrückgewinnung wie Monochromatismus und Homogenität der Probe sind nicht nötig, weil sich die Filterauswahl nur auf die Bildqualität, gegeben durch Kontrast und Ortsauflösung, gründet.

Herkömmliche Histologie erfordert die Gewebefixierung und -einbettung. Virtuelle Histologie lässt sich bereits während der Gewebepräparation durchführen und erlaubt Bewertungen der Zwischenschritte sowie die Kombination der Ergebnisse. Wir wissen, dass die Präparation der herkömmlichen Histologie das Gewebe in seiner Zusammensetzung modifiziert und das lokalen Formveränderungen entstehen. Um diese Schrumpfungsprozesse lokal für das Mäusehirn bei jeder Präparationsstufe zu quantifizieren, wurden die Datensätze elastisch registriert. Das Formalinfixierte Mäusehirn verlor 40 bzw. 60% an Volumen durch die Überführung in Alkohol bzw. Paraffineinbettung. Die dreidimensionalen Verzerrungen hängen sowohl von der lokalen Anatomie als auch vom Abstand zur Oberfläche ab. Die Grosshirnrinde beispielsweise schrumpfte um 55 bzw. 75%, während der Thalamus nur 25 bzw. 45% durch Dehydrierung bzw. Paraffineinbettung verlor. Je nach anatomischem Merkmal und Präparationsschritt erhält man einen charakteristischen Gewebekontrast. Faserabschnitte beispielsweise sind besonders gut sichtbar in Alkohol, während die Trennschichten im Paraffin-eingebetteten Kleinhirn hervortreten.

Virtuelle Histologie hilft auch strukturelle Veränderungen des Gehirns, die durch neurologische Störungen verursacht werden, sichtbar zu machen. Epilepsie gehört zu den gängigen neurologischen Störungen. Schläfenlappenepilepsie ist dabei die häufigste Form bei Erwachsenen. Die bildgebende Kernspintomographie und die konventionelle Histologie sind wenig geeignet, die dreidimensionalen pathologischen Veränderungen zu detektieren. Demgegenüber ermöglicht die synchrotronstrahlungsbasierte Mikrotomographie das Erkennen der Ammonshornsklerose in einem Mausmodell. Die Entstehungsmechanismen von Epilepsien in dem gewählten Mausmodell.

wurden untersucht, indem wir die morphologischen Veränderungen der polymorphen, der granulären und der molekularen Schichten der gezahnten Hirnwindung in den Daten segmentiert haben. Die Ausbreitung der granulären Zellen ist mit einer Volumenzunahme von 2.9 auf $11.4 \times 10^{-3} \text{ mm}^3$ verbunden. In dieser Art und Weise ergänzt die virtuelle Histologie die bisher benutzte zweidimensionale Methode.

Mikrotomographie mit $0.65 \mu\text{m}^3$ Pixeln ist üblicherweise auf ein Blickfeld beschränkt, das einem Volumen von 2.2 mm^3 entspricht. Um das gesamte Mäusehirn mit einem Volumen von 450 mm^3 abzubilden, wurden die erhaltenen radiographischen Daten wie ein Mosaik zusammengesetzt. Somit konnte das Mäusehirn aus isotropen Submikrometer-grossen Voxeln dargestellt werden. Dieser Terabyte-grosse Datensatz enthält eine Fülle anatomischer Informationen. Ihre Auswertung erfordert jedoch einen automatischen Ansatz, der Segmentierung und Registrierung einschliesst. Die Frage bleibt, ob man mittels virtueller Histologie das menschliche Hirn, das 3 000 mal grösser als das Mäusehirn ist, mit einer Voxelgrösse von einem Mikrometer abbilden kann.

List of Publications

Journal Articles (first author)

G. Rodgers, C. Tanner, G. Schulz, A. Migga, W. Kuo, C. Bikis, M. Scheel, V. Kurtcuoglu, T. Weitkamp, B. Müller, “Virtual histology of an entire mouse brain from formalin fixation to paraffin embedding. Part 2: Volumetric strain fields and local contrast changes”, *Journal of Neuroscience Methods* 365 (2022) 109385, doi:10.1016/j.jneumeth.2021.109385

G. Rodgers, W. Kuo, G. Schulz, M. Scheel, A. Migga, C. Bikis, C. Tanner, V. Kurtcuoglu, T. Weitkamp, B. Müller, “Virtual histology of an entire mouse brain from formalin fixation to paraffin embedding. Part 1: Data acquisition, anatomical feature segmentation, tracking global volume and density changes”, *Journal of Neuroscience Methods*, 364 (2021) 109354, doi:10.1016/j.jneumeth.2021.109354

G. Rodgers, G. Schulz, H. Deyhle, W. Kuo, C. Rau, T. Weitkamp, B. Müller, “Optimizing contrast and spatial resolution in hard X-ray tomography of medically relevant tissues”, *Applied Physics Letters* 116 (2020) 023702, doi:10.1063/1.5133742

Peer-Reviewed Conference Proceedings (first author)

G. Rodgers, C. Tanner, G. Schulz, A. Migga, T. Weitkamp, W. Kuo, M. Scheel, M. Osterwalder, V. Kurtcuoglu, B. Müller, “Impact of fixation and paraffin embedding on mouse brain morphology: a synchrotron radiation-based tomography study”, *Proceedings of SPIE* 11840 (2021) 118400P, doi:10.1117/12.2595144

G. Rodgers, G. Schulz, W. Kuo, M. Scheel, V. Kurtcuoglu, T. Weitkamp, B. Müller, C. Tanner, “Non-rigid registration to determine strain fields during mouse brain fixation and embedding”, *Proceedings of SPIE* 11586 (2021) 115860I, doi:10.1117/12.2583632

G. Rodgers, G. Schulz, H. Deyhle, S. Marathe, C. Bikis, B. Müller, T. Weitkamp, “Correction of phase wrapping artifacts in grating-based hard x-ray tomography”, *Proceedings of SPIE* 11113 (2019) 1111308, doi:10.1117/12.2530709

Journal Articles (co-author)

E. Cörek, **G. Rodgers**, S. Siegrist, T. Einfalt, P. Detampel, C. M. Schlepütz, S. Sieber, P. Fluder, G. Schulz, H. Unterweger, C. Alexiou, B. Müller, M. Puchkov, J. Huwyler, “Shedding light on metal-based nanoparticles in zebrafish by computed tomography with micrometer resolution”, *Small* 16(31) (2020) 2000746, doi:10.1002/smll.202000746

C. Bikis, **G. Rodgers**, H. Deyhle, P. Thalmann, A. Hipp, F. Beckmann, T.

Weitkamp, S. Theocharis, C. Rau, G. Schulz, B. Müller, “Sensitivity comparison of absorption and grating-based phase tomography of paraffin-embedded human brain tissue”, *Applied Physics Letters* 114 (2019) 083702, doi:10.1063/1.5085302

Peer-Reviewed Conference Proceedings (co-author)

C. Tanner, **G. Rodgers**, G. Schulz, M. Osterwalder, G. Mani-Caplazi, G. Hotz, M. Scheel, T. Weitkamp, B. Müller, “Extended-field synchrotron microtomography for non-destructive analysis of incremental lines in archeological human teeth cementum”, *Proceedings of SPIE* 11840 (2021) 1184019, doi:10.1117/12.2595180

A. Migga, G. Schulz, **G. Rodgers**, M. Osterwalder, C. Tanner, H. Blank, I. Jerjen, P. Salmon, W. Twengtröm, M. Scheel, T. Weitkamp, C. Schlepütz, J. S. Bolten, J. Huwyler, G. Hotz, S. Madduri, B. Müller, “Laboratory-based phase tomography for micro-imaging of annual layers in human tooth cementum, paraffin-embedded nerve and zebrafish embryo”, *Proceedings of SPIE* 11840 (2021) 118400T, doi:10.1117/12.2597926

B. Müller, A. Khimchenko, **G. Rodgers**, M. Osterwalder, C. Tanner, G. Schulz, “X-ray imaging of human brain tissue down to the molecule level”, *Proceedings of SPIE* 11886 (2021) 1188613, doi:10.1117/12.2592603

M. Osterwalder, J. S. Bolten, **G. Rodgers**, M. Humbel, G. Schulz, C. Tanner, J. Huwyler, B. Müller, “Hard X-ray microtomography of zebrafish larvae”, *Proceedings of SPIE* 11886 (2021) 1188614, doi:10.1117/12.2593119

M. Osterwalder, J. S. Bolten, **G. Rodgers**, G. Schulz, C. Tanner, E. Cörek, J. Huwyler, B. Müller, “Three-dimensional X-ray microscopy of zebrafish larvae”, *Proceedings of SPIE* 11586 (2021) 115860J, doi:10.1117/12.2583639

1 Introduction

Mapping brain cytoarchitecture plays a critical role in understanding the structure-function relationship of the brain and decoding neurological disorders [1]. However, the number of cells in mammalian brains is staggering: the mouse brain contains around 10^8 cells including neurons [2] and the human brain around 10^{11} [3]. These cells belong to a diverse range of cell types and are three-dimensionally organized across multiple length scales [1]. The challenging task of brain mapping therefore relies on multi-modal imaging, combining macroscopic information of the full brain with micro- or nanoscale information from smaller regions.

This chapter reviews the three imaging techniques most commonly employed for neuroimaging: magnetic resonance imaging, optical microscopy, and electron microscopy. Though powerful, especially in their combination, a gap remains for mesoscale brain mapping—three-dimensional imaging of the entire brain with detail on the micrometer scale. The emerging field of X-ray virtual histology holds great promise for this task. This technique is introduced and compared with well-established neuroimaging modalities in Table 1.1. Finally, current challenges for virtual histology-based brain mapping are presented to motivate and outline the present thesis.

Magnetic resonance imaging

Magnetic resonance imaging (MRI) is a technique that probes the relaxation of nuclear spins, usually those of hydrogen atoms. Briefly, MRI involves application of both static and spatially varying magnetic fields to generate magnetization, which is then probed with radio frequency pulses and the resulting evolution is read out with radio frequency coils. A variety of acquisition sequences are used [4], many of which generate excellent contrast for neuroimaging. MRI does not rely on ionizing radiation and can provide *in vivo* or *in situ* volumetric imaging [4]. MRI is the gold standard for mapping macroscopic brain structure, but only reaches voxel sizes of a fraction of a mm [4]. Still, MRI is used extensively in brain atlases on its own or as a reference frame for alignment and correction of subsequent higher resolution imaging, see the well-known *BigBrain* human brain atlas in Ref. 5.

Variants of MRI can also be used to assess microscopic brain structure: Magnetic resonance microscopy can reach voxel sizes of several tens of μm [4] and has been applied to the study of the mouse [6–8] and human brain [9, 10], though cellular resolution is not achieved. Diffusion MRI probes the diffusion of water molecules and allows for deduction of microanatomical properties such as fiber trajectories or axon diameters within mm-sized voxels [11].

Optical microscopy and conventional histology

Conventional histology is the gold standard for evaluation of brain tissue with sub-cellular resolution. This *post mortem* or *ex vivo* technique involves tissue fixation, embedding, sectioning, staining, and imaging with optical microscopy [12, 13]. Histology provides sub- μm in-plane resolution and relies on relatively accessible materi-

als and equipment. There are a wealth of well-established staining protocols such as hematoxylin and eosin, which targets cell nuclei (hematoxylin), cytoplasm (eosin), and connective tissue fibers (eosin) [13]. Immunohistochemistry can be used to label specific antigens, for example with immunofluorescence [13]. Minor variations in tissue processing, staining protocol, and section thickness, however, can result in changes in slide appearance that make automatic analysis difficult [14,15]. Additionally, physical sectioning is irreversible, strain-inducing, and artefact-prone [16,17].

Due to absorption and scattering of light by tissue, serial sectioning and three-dimensional reconstruction of two-dimensional optical micrographs are used for volumetric imaging with conventional histology [16]. Prior blockface photographs or MRI can guide this complex reconstruction problem [16]. Out-of-plane spatial resolution is limited by section thickness, which is typically on the order of tens of μm for serial sectioning. For example, the highest resolution atlas of the entire human brain is based on histology and has sectioning-limited out-of-plane resolution of $20\ \mu\text{m}$ [5].

Several alternatives have been presented to overcome the limited out-of-plane resolution associated with serial sectioning. The combination of two-photon, light-sheet, or confocal microscopy with sectioning *via* microtome or laser ablation [18–20] has allowed for volumetric imaging of the entire mouse brain with isotropic $1\ \mu\text{m}$ -voxels [21,22]. Light scattering can also be reduced by tissue clearing, allowing volumetric imaging with high out-of-plane resolution based on optical sectioning [23–25]. Downsides of these approaches include time-consuming acquisition and specialized sample preparation.

Electron microscopy

Electron microscopy (EM) offers far higher spatial resolution than optical microscopy thanks to electron wavelengths that are around six orders of magnitude shorter than of visible light. Electron microscopes are typically based on electromagnetic lenses to focus beams of electrons with a diffraction limit well below $1\ \text{nm}$. Both scanning and transmission EM are used extensively in the dense reconstruction of neuroanatomy with nm resolution [1,26]. EM is applied only for *post mortem* or *ex vivo* brain tissue. Preparation of biological samples for EM is complex and includes embedding, staining, and physical sectioning [27]. For both scanning and transmission EM, specialized serial sectioning techniques provide sufficient out-of-plane resolution to trace the finest synaptic connections in three dimensions [28]. Research towards automated, high speed, volumetric EM is ongoing, though currently available techniques are limited to volumes of about $1\ \text{mm}^3$ [28–30]. Challenges include costly, time consuming acquisition and processing of datasets ranging from tera- to petabytes in size [28–30].

X-ray virtual histology

Hard X-rays offer deep penetration through brain tissue, bypassing the need for tissue sectioning or clearing. X-rays wavelengths in the angstrom range can also access spatial resolutions below the diffraction limit of visible light microscopy. However, the X-ray absorption of soft tissues is weak, therefore optimizing contrast has been a main challenge for neuroimaging.

Table 1.1: Comparison of neuroimaging techniques. In this table, X-ray virtual histology is defined as hard X-ray microtomography. Note that X-ray nanotomography provides spatial resolution on the nm scale but also restricts imaged volume and sample preparation. This table is intended to show general trends and does not represent all specific cases.

	Magnetic resonance imaging	X-ray virtual histology	Conventional histology	Electron microscopy
Imaging method				
Physical principle	relaxation of nuclear spins	X-ray absorption or refraction	light scattering or fluorescence	electron scattering
Contrast related to	proton density ^a	electron density ^b	immunohistochemical & histochemical stains	electron density, heavy metal stains
Preparation				
State	<i>in vivo</i>	<i>post mortem</i>	<i>post mortem</i>	<i>post mortem</i>
Environment	<i>in situ</i>	extracted	extracted	extracted
Fixation	native	fixed ^c	fixed, embedded	fixed, embedded
Cutting	none	trimmed	sectioned	sectioned, milled
Spatial resolution				
in-plane	0.25 mm ^d	1 μm	0.3 μm	1 nm
out-of-plane	variable, to isotropic	isotropic	variable, to $\approx 10 \mu\text{m}$	variable, to $\approx 1 \text{ nm}$
Volumetric imaging				
Method	<i>k</i> -space reconstruction	tomography	serial sectioning	serial sectioning
Penetration depth	entire organ	entire organ ^e	100 μm	1 μm
Field-of-view	entire organ	100's of mm ³	entire organ	1 mm ³
Compatibility				
Prior imaging	none	MRI	MRI, VH	MRI, VH
Subsequent imaging	CH, EM, VH	CH, EM	none	none

^aA diverse range of MRI sequences are available to probe far more than proton density. Additionally, contrast agents are used in clinical MRI, for example gadolinium-based contrast agents shorten relaxation times and appear bright in T1-weighted imaging.

^bWhile high-*Z* stains are available for virtual histology, they are not required and this thesis will focus on label-free neuroimaging.

^cEmbedding may provide benefits for virtual histology, but is not a requirement.

^dThis refers to standard magnetic resonance imaging. Magnetic resonance microscopy can reach spatial resolution of tens of μm .

^ePenetration increases with increasing photon energy. For penetration of the entire human brain, a photon energy of around 50 keV is needed, while for a mouse brain, 20 keV is sufficient.

This thesis focuses on hard X-ray microtomography [31]. Both microtomography and standard computed tomography rely on the reconstruction of three-dimensional images from a series of two-dimensional radiographs, often called projections [32]. Microtomography refers to tomographic imaging with few- μm resolution, which requires dedicated instrumentation [31]. High resolution is typically achieved with geometric magnification or through high resolution X-ray detectors based on scintillating screens coupled *via* visible light optics to digital sensors. Both laboratory X-ray sources and highly brilliant synchrotron radiation sources can be used for microtomography. The latter generates higher image quality, however access is limited and only granted on the basis of proposals or at high cost.

As an X-ray wavefront travels through matter, it is both attenuated and phase shifted. This process can be described with a photon energy-dependent complex index of refraction, $n = 1 - \delta + i\beta$. For imaging, attenuation or absorption contrast is related to the imaginary part β , while the phase contrast is related to the decrement of the real part δ . Note that X-ray detectors measure the only beam intensity, therefore dedicated approaches are needed to access phase information.

For a detailed discussion of contrast mechanisms and recent developments X-ray microtomography, see e.g. Ref. 33.

Absorption-based imaging is the simplest form of X-ray imaging, although soft tissues are only weakly absorbing. Therefore, contrast agents based on high- Z elements are commonly employed. Staining for cells with heavy metal compounds such as silver nitrate has allowed for impressive visualization of the cytoarchitecture of the brain [34]. Many protocols have been suggested including osmium-based [35–37], iodine-based [38], and Golgi-Cox mercury-based impregnation [39, 40]. Unfortunately, the selection and application of contrast agents is complex and can involve toxic chemicals, therefore it is generally restricted to experts. Development of contrast agents in an active research field, with newly developed contrast agents providing uniform, full-organ coverage and compatibility with subsequent histology [41, 42].

An alternative approach is to utilize phase contrast methods for label-free neuroimaging down to the cellular level [43]. Since the Bonse-Hart crystal interferometer was demonstrated in 1965 [44], a variety of phase-sensitive imaging methods have emerged—particularly since a strong resurgence of interest in the 1990’s [45]. These include but are not limited to grating- [46–49], speckle- [50–53], coded aperture- [54, 55], analyzer- [56–58], as well as propagation-based approaches [59–64].

While each offers specific benefits, single-distance propagation-based phase contrast is among the most commonly used because it offers a simple setup, impressive contrast gains, and high spatial resolution. Recently, propagation-based phase tomography of neuronal volumes up to tens of mm^3 in size have allowed for quantitative analysis of cytoarchitecture in mice and humans [65–68]. Unique possibilities such as capillary-level visualization of amyloid-angiopathy were demonstrated in a mouse brain model of Alzheimer’s disease [69]. These results are contributing to the emerging field of *X-ray virtual histology* [70].

Synchrotron radiation facilities offer higher brilliance than laboratory-based X-ray sources, but accessibility is reduced. To increase the availability of virtual histology, cellular-resolution neuroimaging has been demonstrated at laboratory sources with absorption contrast, taking advantage of standard histological tissue embedding [71]. State-of-the-art laboratory X-ray sources have also demonstrated promising results for virtual histology including cellular-resolution neuroimaging based on propagation-based phase contrast [67, 68, 72].

It should be noted that complementary hard X-ray nanotomography has allowed for dense neuronal reconstruction with sub-100 nm resolution [73], even for unstained tissue [74]. This approach offers volumetric data comparable to EM without the need for physical sectioning. Efforts are underway to expand the field-of-view of nanotomography towards macroscopic specimens [75].

Towards brain atlases with X-ray virtual histology

X-ray virtual histology based on microtomography is a promising tool for cellular-resolution full-brain mapping, where an understanding of mesoscale cytoarchitecture can link our microscopic and macroscopic understanding of brain organization [76]. It offers label-free, dense visualization of the brain’s cytoarchitecture and is compatible with subsequent histology for validation and as part of a multi-modal imaging strategy.

This thesis aims to address several challenges for the generation of future brain atlases based on X-ray virtual histology. These include optimizing soft tissue contrast at high spatial resolution, understanding morphological effects of tissue fixation and embedding, demonstrating medically relevant findings and benchmarking virtual histology with gold-standard conventional histology, and developing protocols for large volume imaging and processing the related teravoxel-sized datasets. Each chapter of this thesis addresses one of these challenges:

Chapter 2 discusses the optimization of contrast and spatial resolution for X-ray microtomography of physically soft tissues. Highlights:

- Hard X-ray microtomography of two biomedically relevant tissues: human brain and mouse kidney
- Quantifying the trade-off between spatial resolution and contrast-to-noise as a function of applied filter kernel
- Surprisingly, simple Gaussian filtering was advantageous for high spatial resolution
- Introduced a figure-of-merit for image quality: $QF = \frac{\tanh(CNR)}{(SR/SR_0)}$

Chapter 3 demonstrates a method to quantify morphology and X-ray contrast changes within an entire mouse brain as a result of histological tissue preparation. Highlights:

- Virtual histology with $(3\ \mu\text{m})^3$ -voxels of a single mouse brain over the course of standard histological preparation
- Segmentation to quantify non-uniform brain shrinkage
- Non-rigid registration of embedding-dependent local microanatomy shrinkage
- Quantification of volumetric strain fields within the mouse brain
- X-ray contrast improves by ethanol dehydration and paraffin embedding

Chapter 4 presents a complementary conventional- and virtual-histology approach to study the healthy and epileptic mouse brain. Highlights:

- X-ray microtomography of healthy and epileptic mouse brains with $1.6\ \mu\text{m}$ pixel size prior to conventional histopathological investigation
- Label-free virtual histology allows for identification hippocampal sclerosis
- Virtual histology benchmarked with well-established histochemical and immunohistochemical stains
- Quantified pathological changes in morphology and density based on segmentation of the volumetric data

Finally, **Chapter 5** presents a data acquisition and processing approach as well as first results for microtomography of the entire mouse brain with $0.65\ \mu\text{m}$ pixel size. Highlights:

- Built a reconstruction pipeline for mosaic-style extension of field-of-view for microtomography
- Implemented ring correction, filtering or phase retrieval, and teravoxel reconstruction within a reasonable time frame
- Experimental realization of mosaic imaging with $64\times$ larger reconstructed area

compared to standard acquisition

- Visualization of an entire mouse brain with 0.65 μm pixel sizes
- Employed for mosaic tomography of paraffin-embedded nerve bundles [77], human teeth from Natural History Museum of Basel [78], and entire mouse brains [79]

Contributions

The results presented in Chapters 2 - 5 were the product of strong, interdisciplinary collaborations. While the author of this thesis (G.R.) was the primary author of these sections, numerous scientists made important contributions. The roles each of the co-authors are listed below. Roles are given according to the CRediT (Contributer Roles Taxonomy). Where applicable, the order of the co-authors matches the related manuscripts.

Chapter 2: contributions from Georg Schulz (G.S.), Hans Deyhle (H.D.), Willy Kuo (W.K.), Christoph Rau (C.R.), Timm Weitkamp (T.W.), and Bert Müller (B.M.). The contribution of each co-author was:

Co-author	Role
G.R.	Conceptualization, Methodology, Software, Validation, Formal analysis, Investigation, Writing - Original Draft, Writing - Review & Editing, Visualization
G.S.	Methodology, Investigation, Writing - Review & Editing, Visualization, Supervision, Funding acquisition
H.D.	Software, Investigation, Writing - Review & Editing
W.K.	Investigation, Resources
C.R.	Resources, Writing - Review & Editing, Funding acquisition
T.W.	Conceptualization, Writing - Review & Editing
B.M.	Conceptualization, Methodology, Investigation, Writing - Review & Editing, Visualization, Supervision, Project administration, Funding acquisition

Chapter 3: contributions from Willy Kuo (W.K.), Georg Schulz (G.S.), Mario Scheel (M.S.), Alexandra Migga (A.M.), Christos Bikis (C.B.), Christine Tanner (C.T.), Vartan Kurtcuoglu (V.K.), Timm Weitkamp (T.W.), Bert Müller (B.M.).

Co-author	Roles
G.R.	Conceptualization, Methodology, Software, Formal analysis, Investigation, Data curation, Writing - Original Draft, Writing - Review & Editing, Visualization, Funding acquisition
W.K.	Methodology, Validation, Investigation, Resources, Writing - Review & Editing
G.S.	Conceptualization, Methodology, Investigation, Writing - Review & Editing, Visualization, Supervision
M.S.	Formal analysis, Investigation, Resources, Writing - Review & Editing
A.M.	Validation, Formal analysis, Writing - Review & Editing, Visualization
C.B.	Methodology, Formal analysis, Writing - Review & Editing
C.T.	Software, Formal analysis, Investigation, Writing - Review & Editing, Visualization, Supervision

V.K.	Writing - Review & Editing, Supervision, Project administration, Funding acquisition
T.W.	Investigation, Resources, Writing - Review & Editing, Funding acquisition
B.M.	Conceptualization, Methodology, Investigation, Resources, Writing - Review & Editing, Visualization, Supervision, Project administration, Funding acquisition

Chapter 4: contributions to this manuscript in preparation come from Christos Bikis (C.B.), Philipp Janz (P.J.), Georg Schulz (G.S.), Christine Tanner (C.T.), Melissa Osterwalder (M.O.), Peter Thalmann (P.T.), Carola Haas (C.H.), Bert Müller (B.M.):

Co-author	Role
G.R.	Conceptualization, Software, Formal analysis, Data curation, Writing - Original Draft, Writing - Review & Editing, Visualization
C.B.	Conceptualization, Methodology, Validation, Investigation
P.J.	Methodology, Validation, Investigation, Resources
G.S.	Investigation, Resources, Visualization, Supervision
C.T.	Writing - Review & Editing, Visualization, Supervision
M.O.	Writing - Review & Editing
P.T.	Software, Investigation
C.H.	Conceptualization, Methodology, Resources, Supervision, Project administration, Funding acquisition
B.M.	Conceptualization, Methodology, Resources, Writing - Review & Editing, Visualization, Supervision, Project administration, Funding acquisition

Chapter 5: the presented work is a collaborative effort involving Christine Tanner (C.T.), Melissa Osterwalder (M.O.), Georg Schulz (G.S.), Timm Weitkamp (T.W.), Mario Scheel (M.S.), Marta Girona-Alarcón (M.G.-A.), Willy Kuo (W.K.), Vartan Kurtcuoglu (V.K.), and Bert Müller (B.M.).

Contributor	Role
G.R.	Conceptualization, Methodology, Software, Formal analysis, Investigation, Data curation, Writing - Original Draft, Writing - Review & Editing, Visualization, Funding acquisition
C.T.	Software, Validation, Investigation, Data curation, Writing - Review & editing, Visualization, Supervision
M.O.	Investigation, Data curation
G.S.	Methodology, Investigation, Visualization, Supervision
T.W.	Investigation, Resources
M.S.	Investigation, Resources
M.G.-A.	Investigation, Resources
W.K.	Resources
V.K.	Resources, Supervision, Project administration, Funding acquisition
B.M.	Conceptualization, Methodology, Investigation, Supervision, Project administration, Funding acquisition

2 Optimizing spatial and density resolution for X-ray virtual histology

High contrast-to-noise ratio (CNR) is needed to distinguish the minute native tissue density differences within the brain or other soft tissue. In synchrotron radiation-based microtomography, single distance phase retrieval is often employed to boost CNR. Image quality, however, is a function of both CNR and spatial resolution (SR). In this study, we explore the trade-off between CNR and SR with the application of the most common phase retrieval, Paganin's filter, and with simple Gaussian filtering, well-known from image processing. This report focuses on two synchrotron radiation-based microtomography measurements, one of a mouse kidney and the other of a biopsy punch from a paraffin-embedded human cerebellum. For small filter kernels, the CNR generated by Gaussian filtering beat Paganin filtering at equal SR. Paganin filtering produced better results when large filter kernels were applied. We also introduce a dimensionless quality factor, which can be used to select an appropriate filter kernel. Our results underline that understanding the SR-CNR trade-off is critical to discussions of image quality and can help in the optimization of virtual histology for medically relevant tissues.

Published in *Applied Physics Letters*

Optimizing contrast and spatial resolution in hard x-ray tomography of medically relevant tissues

Cite as: Appl. Phys. Lett. **116**, 023702 (2020); doi: 10.1063/1.5133742

Submitted: 25 October 2019 · Accepted: 26 December 2019 ·

Published Online: 16 January 2020



View Online



Export Citation



CrossMark

Griffin Rodgers,¹ Georg Schulz,¹ Hans Deyhle,^{1,2} Willy Kuo,^{1,3} Christoph Rau,² Timm Weitkamp,^{4,a)} and Bert Müller¹

AFFILIATIONS

¹Biomaterials Science Center, University of Basel, 4123 Allschwil, Switzerland

²Diamond Light Source Ltd., Didcot OX11 0DE, United Kingdom

³The Interface Group, Institute of Physiology, University of Zurich, 8057 Zurich, Switzerland

⁴Synchrotron Soleil, 91192 Gif-sur-Yvette, France

^{a)}Electronic mail: weitkamp@synchrotron-soleil.fr

ABSTRACT

Hard x-ray tomography with Paganin's widespread single-distance phase retrieval filter improves the contrast-to-noise ratio (CNR) while reducing spatial resolution (SR). We demonstrate that a Gaussian filter provided larger CNR at high SR with interpretable density measurements for two medically relevant soft tissue samples. Paganin's filter produced larger CNR at low SR, though *a priori* assumptions were generally false and image quality gains diminish for CNR > 1. Therefore, simple absorption measurements of low-Z specimens combined with Gaussian filtering can provide improved image quality and model-independent density measurements compared to single-distance phase retrieval.

Published under license by AIP Publishing. <https://doi.org/10.1063/1.5133742>

Hard x-ray microtomography non-destructively provides a three-dimensional map of a wide range of samples.¹ Medically relevant tissues are composed primarily of low-Z elements and therefore have low x-ray absorption. Phase contrast methods have been proposed because the phase cross section is orders of magnitude larger than the absorption cross section for photon energies on the order of 10 keV.²

The simplest phase contrast techniques are propagation-based, where Fresnel diffraction from the free-space propagation of the x-ray wavefront makes phase information detectable in intensity measurements.³ Sufficient coherence and the propagation distance allow for the wavefront phase shift to be extracted from radiographs at one or more positions downstream.^{4,5} Exact phase retrieval for samples with non-negligible absorption may require several downstream positions or multiple energies.⁶ Still, single-distance approaches can provide semi-quantitative phase retrieval, reduce edge enhancement, and in some cases improve the contrast-to-noise ratio (CNR).⁷ The single-distance phase retrieval filter introduced by Paganin *et al.* is among the most used thanks to its simplicity and large CNR gains.⁸ This method has found many applications, for example, low-dose medical imaging and virtual histology.^{9–12}

However, the image quality is a function of both the CNR and the spatial resolution (SR),^{13,14} which Paganin filtering reduces.¹⁵ It is often unclear if CNR gains should be attributed to phase sensitivity or

the low-pass effects. Previous experiments have shown that the pixel binning of tomography measurements improves the CNR at the expense of SR.^{14,16} The question now arises if the low-pass filtering of absorption datasets¹⁷ outperforms Paganin phase retrieval when both CNR and SR are taken into account.

In this study, we present two synchrotron radiation-based microtomography (SR μ CT) measurements of biological tissues: a cylinder of the paraffin-embedded human cerebellum and a formalin-fixed mouse kidney. Gaussian filtering was applied to the projections prior to reconstruction in the absorption contrast mode, while Paganin filtering was used for the phase retrieval of the projections before reconstruction. The CNR and SR were measured for a range of filter kernels to optimize the image quality.

The human cerebellum tissue was extracted post-mortem with informed consent for scientific use and embedded according to the standard procedure for pathological analysis, i.e., transferred to 4% histological-grade buffered paraformaldehyde, ascending ethanol solutions, and xylene and finally embedded in a paraffin mixture. A stainless-steel punch was used to produce the final 6 mm diameter sample.

One seven-month old female C57BL/6J mouse was anesthetized with Ketamine/Xylazine, and the kidneys were perfused retrogradely via the abdominal aorta¹⁸ at 150 mm Hg with 10 ml phosphate-buffered

saline (PBS), 100 ml 4% formaldehyde/1% glutaraldehyde/PBS, 20 ml PBS, 50 ml glycine solution (5 mg/ml in PBS), and 40 ml PBS. 4 ml of x-ray contrast agent solution (75 mg iodine/ml) was injected into the vasculature to distinguish blood vessels from tubules. The abdominal cavity was then filled with 4% glutaraldehyde/PBS to cross link the contrast agent, and the kidneys excised and kept in 4% glutaraldehyde/PBS. The right kidney was mounted in 1% Agar/PBS in a 0.5 ml plastic tubes intended for polymerase chain reaction (PCR tubes) to avoid movement during scanning.

The SR μ CT measurements were performed at the Diamond Manchester Imaging Beamline (I13-2, Diamond Light Source, Didcot, UK), where an undulator source is used.¹⁹ Table I shows the acquisition parameters for both measurements.

The optimal photon energy criteria for an absorption contrast measurement are given by $\mu(E) \times D = 2$ (equivalent to 13% transmission), where $\mu(E)$ is the linear attenuation coefficient and D the sample diameter.¹³ Both the brain and kidney samples have $\mu \times D < 2$, higher than optimal photon energies.

The conditions for the validity of the Paganin phase retrieval are as follows: (i) a single homogenous material or constant δ/β throughout the specimen, (ii) a monochromatic plane wave, and (iii) the detector in the near-field.²⁰ It should be noted negligible sample absorption is not required. Previous x-ray grating interferometry measurements of the brain sample confirm the constant δ/β ratio;¹⁷ however, the δ/β ratio is unknown for the mouse kidney. Condition (ii) is valid for the brain measurement with a double-crystal monochromator, and previous experimental results have shown that Paganin's method is robust for

polychromaticity such as filtered "pink beam" radiation.²¹ Condition (iii) can be expressed by the critical propagation distance $z_c = (2a)^2/\lambda$, with pixel size a and x-ray wavelength λ . For the brain, the 7 cm propagation distance is well within $z_c = 137$ cm. The kidney had 9 cm distance and $z_c = 9.4$ cm. Therefore, the SR for both measurements will not be limited by propagation effects.²⁰ Both measurements showed edge enhancement at the outer boundaries of the sample.

The initial SR of the kidney reconstruction was around 6 pixels, while the initial SR of the brain measurement was near the Nyquist limit (measured with the method proposed in Ref. 22.) These SR

TABLE I. Summary of the acquisition parameters for the human cerebellum and mouse kidney samples measured at the Diamond Manchester Imaging Beamline (I13-2, Diamond Light Source, Didcot, UK). z_c is the critical distance for the single distance phase retrieval as defined by Weitkamp *et al.*²⁰

Sample	Brain	Kidney
Mode	Monochromatic	Filtered pink beam
Mean photon energy	20 keV	23 keV
Camera	pco.4000 ^a	pco.4000
Bit depth	14	14
Objective	PLAPON 2X ^b	PLAPON 4X
Numerical aperture	0.08	0.16
Hardware binning	2 × 2	1 × 1
Effective pixel size	4.6 μ m	1.125 μ m
Scintillator	LuAG	LuAG
	500 μ m	500 μ m
Detector distance	7 cm	9 cm
z_c	137 cm	9.4 cm
Sample transmission ^c	75%	56%
Acquisition mode	Standard	Off-axis
	Step scan	Fly scan
Number of projections	1201	2501
Exposure time	2 s	0.5 s
Mean flat-field counts	10 000	1700

^aPCO AG, Kelheim, Germany.

^bOlympus Corporation, Tokyo, Japan.

^cMean over ROI in the sample center.

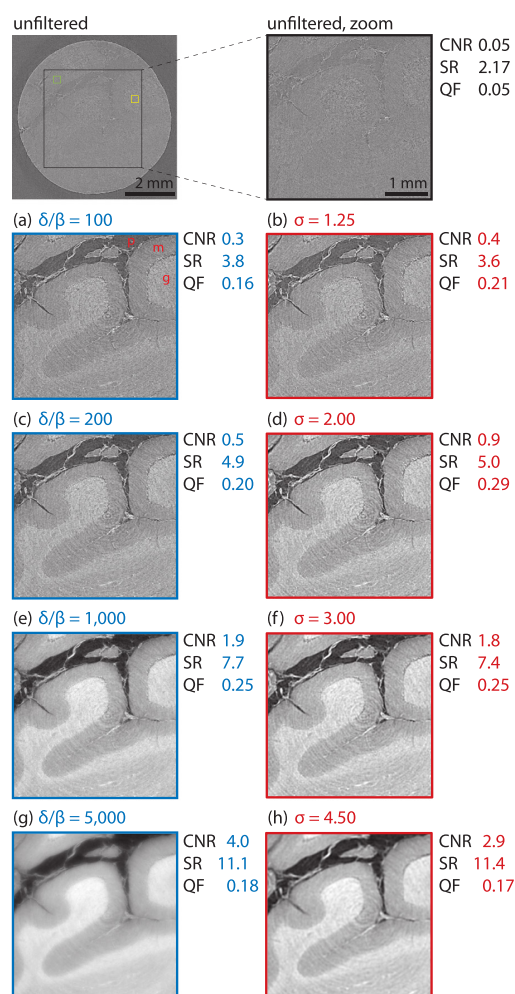


FIG. 1. Reconstructed slices of the human cerebellum after Paganin phase retrieval (left, blue) and Gaussian filtering (right, red) of the transmission projections. Filter kernel, SR (in pixels), CNR, and QF are indicated. Regions for the CNR measurement are given in the unfiltered slice (green and yellow). The grayscale is given by the intersection of the histogram of each zoom with a threshold.

values are relatively consistent with the expected resolution of the detection system according to the formalism developed by Koch *et al.* in Ref. 23. If the attenuation lengths in LuAG ($40\ \mu\text{m}$ for 20 keV and $60\ \mu\text{m}$ for 23 keV) are considered as effective scintillator depths, the values thus obtained for the expected resolution in terms of the full width of the line-spread function containing 90% of the intensity response are $9\ \mu\text{m}$ (i.e., approximately 2 pixels) for the brain samples and $5\ \mu\text{m}$ (approximately 5 pixels) for the kidney measurements.

Both the Paganin and Gaussian filters can be described as a convolution of the transmission projection $T(x, y) = I(x, y)/I_0(x, y)$. The Paganin filtered projection is given by

$$P(x, y) = \mathcal{F}^{-1} \left\{ \frac{1}{1 + \frac{\lambda z \delta}{4\pi\beta}(u^2 + v^2)} \times \mathcal{F}\{T(x, y)\} \right\}, \quad (1)$$

where \mathcal{F} (\mathcal{F}^{-1}) denotes a two-dimensional (inverse) Fourier transform, u and v are the Fourier-space coordinates (in units of inverse pixels) dual to x and y , and z is the propagation distance.^{8,20} The Gaussian filtered projections are interpreted as software-blurred transmission projections and are defined by

$$G(x, y) = \mathcal{F}^{-1} \{ e^{-2\pi^2\sigma^2(u^2 + v^2)} \times \mathcal{F}\{T(x, y)\} \}, \quad (2)$$

where σ is the standard deviation of the real-space Gaussian filter (in pixels). Thus, Paganin filtering is multiplication with a Lorentzian in Fourier space, while Gaussian filtering is multiplication with a Gaussian in Fourier space. Taking the logarithm of Eq. (1) and multiplying by $\delta/2\beta$ provide a projected phase shift map, while taking the logarithm of Eq. (2) and multiplying by $1/(2ka)$ provide the projected β map.

For this study, a filtered back-projection with the standard Ram-Lak filter was used for tomographic reconstruction. All analysis steps were implemented in Matlab (The MathWorks, Inc., Natick, USA).

CNR and SR were measured in the reconstructed slices. CNR is defined as $|\mu_1 - \mu_2|/\sqrt{\sigma_1^2 + \sigma_2^2}$ based on the mean (μ) and standard deviation (σ) within equal-sized, uniform regions of interest (see green and yellow boxes of Figs. 1 and 2). For reference, the difference of the linear attenuation coefficient between these regions of interest is $1.33\ \text{m}^{-1}$ ($43.1\ \text{m}^{-1}$) for the brain (kidney) sample. The SR was measured with the method proposed by Mizutani *et al.*,²² which does not require a noise criterion. Large values of SR correspond to low spatial resolution. Here, SR is normalized by pixel size.

We define the image quality factor (QF) as

$$\text{QF} = \frac{\tanh(\text{CNR})}{\text{SR}/\text{SR}_0}, \quad (3)$$

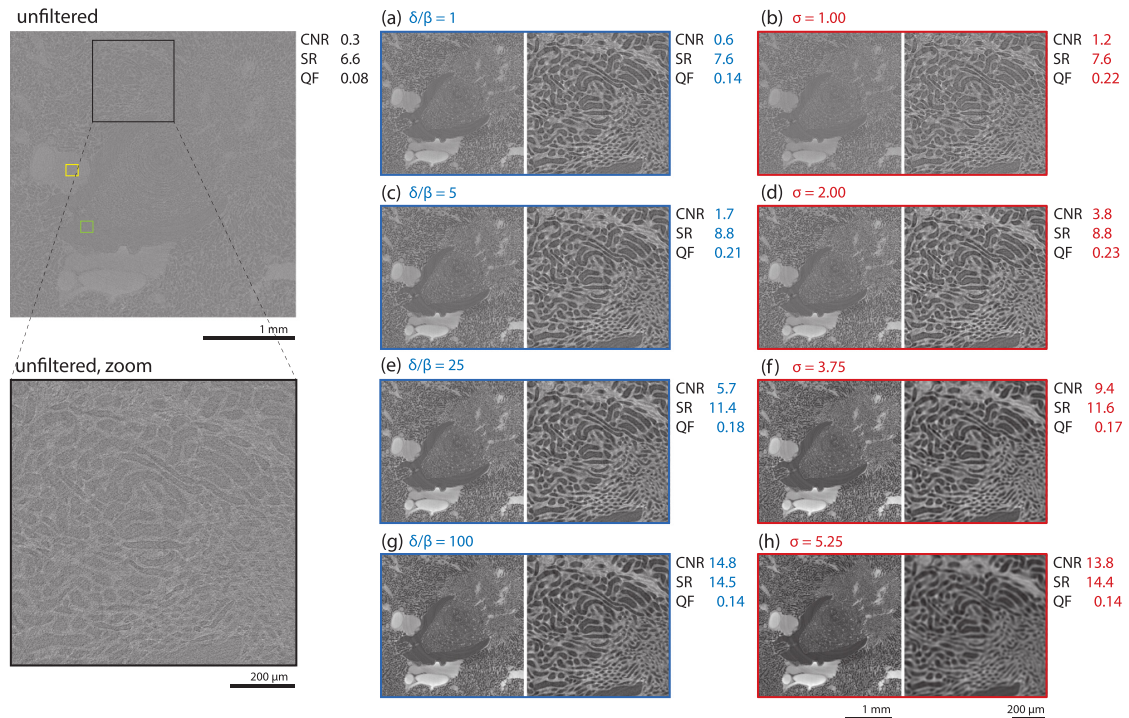


FIG. 2. Reconstructed slices of the mouse kidney after Paganin phase retrieval (left, blue) and Gaussian filtering (right, red) of transmission projections. Filter kernel, CNR, SR (pixels), and QF are indicated. Zooms help us to identify reduced SR and improved CNR with the increasing filter size. Regions for the CNR measurement are given in the unfiltered slice (green and yellow). The grayscale is based on the intersection of the histogram of each zoom with a threshold.

where $SR_0 = 2$ pixels is the Nyquist limit for the minimum SR. Here, QF is used as an image quality metric that is maximized at $QF = 1$ for Nyquist-limited spatial resolution and $CNR \rightarrow \infty$. The hyperbolic tangent provides diminishing increases in QF for large CNR.

Figure 1 shows characteristic reconstructed slices of the cerebellum sample after Paganin and Gaussian filtering with increasing kernel sizes. The unfiltered reconstruction is given in the top row for reference. Paraffin (p, black), the molecular layer (m, darker gray), and the granular layer (g, lighter gray) can be identified in all reconstructions. With increasing filter size, both CNR and SR values increase. Each row has approximately equal spatial resolution. The largest QF is achieved with Gaussian filtering (d), though both filters significantly improve the image quality (d)–(f). At low (high) values of SR, Gaussian (Paganin) produces higher QF images. It should be noted that all Gaussian filters produced accurate β values, while only the Paganin filter with $\delta/\beta = 10^3$ gave accurate δ as confirmed by previous experiments.¹⁷

Figure 2 shows the characteristic reconstructed slices and zooms of the mouse kidney, including the unfiltered datasets (left). Tubular lumina (background, black), tubular tissue (darker gray), and contrast agent in the vascular lumina (lighter gray) can all be identified, particularly after filtering. The highest QF image is produced with the Gaussian filter of $\sigma = 2$ pixels. For all SR values, the QF of Gaussian filtering is greater or equal to Paganin filtering. Measured β does not depend on the Gaussian filter, while δ is linear to the δ/β of the Paganin filter. The correct δ/β was unknown for this sample.

The CNR is plotted against the SR for both samples in Fig. 3. At small values of SR, Gaussian filtering provides greater CNR. At larger values of SR, Paganin filtering produces greater CNR. For the brain, the crossover is at $\delta/\beta = 10^3$, where accurate δ values are given by Paganin filtering. For the kidney, the crossover point was at $\delta/\beta = 10^2$. The QF in these larger filter kernel regions is lower because $CNR > 1$, and therefore, the increasing SR is the dominant factor. For the brain specimen, the results of data binning^{14,16} are given, though CNR is lower than for Gaussian filtering for any SR. For convenience, the software binned data were nearest-neighbor interpolated back to their original size prior to reconstruction to have equal pixel size to the other filtered datasets.

The maximum QF reached for the brain (kidney) dataset was 0.29 (0.24) for Gaussian filtering, 0.25 (0.21) for Paganin filtering, and 0.23 for software binning. The maximum QF for the kidney dataset was achieved at $\delta/\beta = 5$, while for the brain, it was achieved at $\delta/\beta = 500$ and 1000. For context, the full width at half maximum of the Paganin filter for the kidney dataset at $\delta/\beta = 5$ is nearly equal to that in the brain dataset at $\delta/\beta = 100$ [from Eq. (1) and the measurement parameters in Table I.] Still, the δ/β optimizing QF for the Paganin filter has no inherent physical meaning. The trade-off between SR and CNR for Paganin filtering will depend on the noise and spatial resolution of the imaging system rather than the accuracy of the phase retrieval.

It should be noted that while software binning shows smaller QF compared to Gaussian filtering for any SR, it provides the benefit of reducing the three-dimensional dataset's size by the cube of the binning factor. For this study, a two-dimensional Gaussian filter was applied to the projections to make an analogy with the Paganin filter. Three-dimensional Gaussian filtering of the reconstructed data provided similar results with the maximum quality factor within 1% of

two-dimensional filtering, although previous studies have shown that binning prior to reconstruction provides benefits over binning reconstructed data.¹⁴ The combination of Gaussian filtering before binning can provide the benefits of both strategies. Mean and median filters also provided lower QF at any SR compared with Gaussian filtering, and therefore, they are not presented here. Further studies should determine how Gaussian filtering compares with more advanced filters such as bilateral filtering.^{24,25}

For reference, the difference in the linear attenuation coefficient between the regions of interest is 1.33 m^{-1} in Fig. 1 and 43.1 m^{-1} in Fig. 2. The density resolution varies with filter kernel size and can be calculated considering the CNR. Interpreting density resolution for the

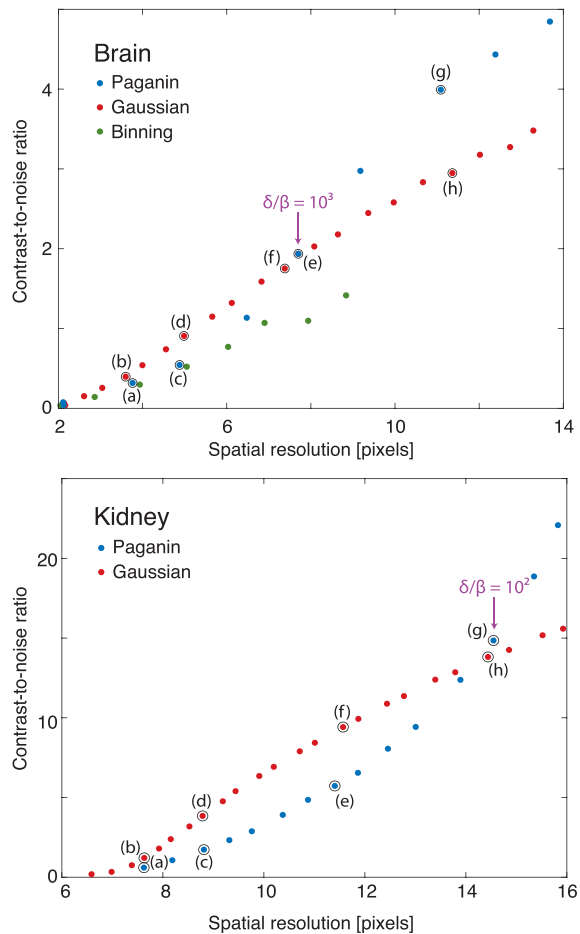


FIG. 3. Measured CNR and SR (in pixels) for the reconstructed slices of the human brain (top) and the mouse kidney (bottom) after Paganin phase retrieval (orange) and Gauss filtering (blue). Binning up to 8×8 pixels is also given for the brain for reference (green). Both filters show a sigmoidal relationship between CNR and SR until at very large SR, uniform regions of interest (ROIs) become difficult to select. Slices shown in Figs. 1(a)–1(h) and 2(a)–2(j) are indicated.

Paganin phase retrieval is more challenging. For a comparison with other techniques such as grating interferometry, several other factors must be considered in addition to the trade-off between CNR and SR.¹⁷

Future studies are needed to determine the effects of the noise level of the projections, sample composition, and propagation distance. Previous results have shown that certain single-distance phase retrieval results are robust against noise,⁷ though the initial noise level will limit the maximum achievable CNR and the slope of the SR vs CNR curve. We expect increasing the propagation distance will benefit the performance of the Paganin filter over Gaussian filtered absorption, although the latter may still perform better than previously expected. Characterizing the beam coherence^{26–28} will help quantify the contributions of phase information vs low pass filtering to CNR gains. Paganin's approach likely proves more advantageous when absorption is negligible.

Gaussian filtering produces higher quality images at high spatial resolution (low SR values) for the two biomedically relevant samples considered here. Being model-independent, it also allows for the quantitative interpretation of gray values. Paganin filtering, though more commonly used, only outperformed Gaussian filtering at low spatial resolution where CNR was already large. These results suggest that for certain medically relevant specimens, the density resolution improvements from phase retrieval can be matched or exceeded by suitably low-pass filtered absorption measurements. These results are especially meaningful for samples with non-negligible absorption. We conclude that both the SR and CNR must be considered when comparing the quality of tomography data.

The authors thank S. Marathe, K. Wanelik, and A. Bodey, Diamond Light Source I13-2, for their support during the beam time. The authors thank C. Bikis, University of Basel, and S. Theocharis, National and Kapodistrian University of Athens, for providing the brain specimen. This project was supported by Diamond Light Source Projects Nos. MT 19829-1 and MT 20746. T.W. acknowledges the support from the French National Research Agency through the EQUIPEX investment program, project NanoimagesX, Grant No. ANR-11-EQPX-0031. The authors acknowledge the support from the Swiss National Science Foundation through NCCR Kidney.CH and Project Nos. 185058 and 153523.

REFERENCES

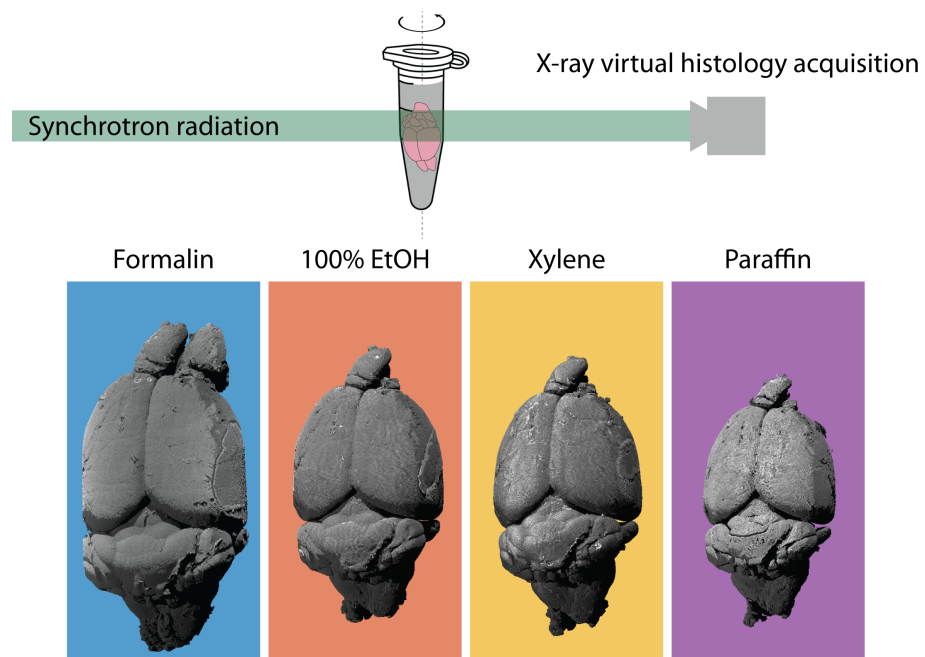
- ¹S. R. Stock, *Microcomputed Tomography: Methodology and Applications* (CRC Press, 2008).
- ²A. Momose, *Jpn. J. Appl. Phys., Part 1* **44**, 6355 (2005).
- ³D. Paganin, *Coherent X-Ray Optics* (Oxford University Press, 2006), Vol. 6.
- ⁴P. Cloetens, W. Ludwig, J. Baruchel, D. Van Dyck, J. Van Landuyt, J. Guigay, and M. Schlenker, *Appl. Phys. Lett.* **75**, 2912 (1999).
- ⁵A. V. Bronnikov, *Opt. Commun.* **171**, 239 (1999).
- ⁶T. E. Gureyev, S. Mayo, S. Wilkins, D. Paganin, and A. W. Stevenson, *Phys. Rev. Lett.* **86**, 5827 (2001).
- ⁷M. N. Boone, Y. De Witte, M. Dierick, A. Almeida, and L. Van Hoorebeke, *Microsc. Microanal.* **18**, 399 (2012).
- ⁸D. Paganin, S. Mayo, T. E. Gureyev, P. R. Miller, and S. W. Wilkins, *J. Microsc.* **206**, 33 (2002).
- ⁹F. Arfelli, M. Assante, V. Bonvicini, A. Bravin, G. Cantatore, E. Castelli, L. Dalla Palma, M. Di Michiel, R. Longo, A. Olivo *et al.*, *Phys. Med. Biol.* **43**, 2845 (1998).
- ¹⁰M. Töpferwien, F. van der Meer, C. Stadelmann, and T. Salditt, *Proc. Natl. Acad. Sci. U. S. A.* **115**, 6940 (2018).
- ¹¹J. Albers, S. Pacilé, M. A. Markus, M. Wiart, G. Vande Velde, G. Tromba, and C. Dullin, *Mol. Imaging Biol.* **20**, 732 (2018).
- ¹²S. E. Hieber, C. Bikis, A. Khimchenko, G. Schweighauser, J. Hench, N. Chicherova, G. Schulz, and B. Müller, *Sci. Rep.* **6**, 32156 (2016).
- ¹³L. Grodzins, *Nucl. Instrum. Methods Phys. Res.* **206**, 541 (1983).
- ¹⁴P. Thurner, F. Beckmann, and B. Müller, *Nucl. Instrum. Methods Phys. Res., Sect. B* **225**, 599 (2004).
- ¹⁵M. Boone, "New imaging modalities in high resolution X-ray tomography," Ph.D. thesis (Ghent University, 2013).
- ¹⁶P. Thalman, C. Bikis, A. Hipp, B. Müller, S. Hieber, and G. Schulz, *Appl. Phys. Lett.* **110**, 061103 (2017).
- ¹⁷C. Bikis, G. Rodgers, H. Deyhle, P. Thalman, A. Hipp, F. Beckmann, T. Weitkamp, S. Theocharis, C. Rau, G. Schulz *et al.*, *Appl. Phys. Lett.* **114**, 083702 (2019).
- ¹⁸J. Czogalla, F. Schweda, and J. Löffing, *J. Visualized Exp.* **117**, e54712 (2016).
- ¹⁹C. Rau, U. Wagner, Z. Pešić, and A. De Fanis, *Phys. Status Solidi A* **208**, 2522 (2011).
- ²⁰T. Weitkamp, D. Haas, D. Wegrzynek, and A. Rack, *J. Synchrotron Radiat.* **18**, 617 (2011).
- ²¹C. Rau, T. Weitkamp, A. Snigirev, C. G. Schroer, J. Tümmeler, and B. Lengeler, *Nucl. Instrum. Methods Phys. Res., Sect. A* **467–468**, 929 (2001).
- ²²R. Mizutani, R. Saiga, S. Takekoshi, C. Inomoto, N. Nakamura, M. Itokawa, M. Arai, K. Oshima, A. Takeuchi, K. Uesugi *et al.*, *J. Microsc.* **261**, 57 (2016).
- ²³A. Koch, C. Raven, P. Spanne, and A. Snigirev, *J. Opt. Soc. Am. A* **15**, 1940 (1998).
- ²⁴C. Tomasi and R. Manduchi, in Sixth International Conference on Computer Vision (IEEE Cat. No.98CH36271) (1998), pp. 839–846.
- ²⁵A. Manduca, L. Yu, J. D. Trzasko, N. Khaylova, J. M. Kofler, C. M. McCollough, and J. G. Fletcher, *Med. Phys.* **36**, 4911 (2009).
- ²⁶J. Lin, D. Paterson, A. G. Peele, P. J. McMahon, C. T. Chantler, and K. A. Nugent, *Phys. Rev. Lett.* **90**, 074801 (2003).
- ²⁷F. Pfeiffer, O. Bunk, C. Schulze-Briesche, A. Diaz, T. Weitkamp, C. David, J. Van Der Veen, I. Vartanyants, and I. Robinson, *Phys. Rev. Lett.* **94**, 164801 (2005).
- ²⁸Y. Kashyap, H. Wang, and K. Sawhney, *Phys. Rev. A* **92**, 033842 (2015).

3 Impact of fixation and paraffin embedding on mouse brain morphology and X-ray contrast

Cellular-resolution neuroimaging with conventional histology typically relies on formalin fixation and paraffin embedding of *post mortem* tissue. This tissue preparation is gaining popularity for virtual histology because it is compatible with conventional histology. The standard protocol involves fixation in formalin, dehydration in ethanol, clearing in xylene, and embedding into a paraffin block [13], which alters the densities of physically soft tissues and induces non-uniform strain at each step. On one hand, density changes can be taken advantage of to improve X-ray contrast [71, 72]. On the other hand, the morphology changes should be corrected to more accurately reflect the physiological state. Here, we present the non-rigid registration of volumetric data from X-ray microtomography of a single mouse brain at each intermediate step of the standard paraffin embedding protocol. This approach produces volumetric strain fields and directly corrects induced deformations to align microanatomical features.

This chapter presents a two-part manuscript published in *Journal of Neuroscience Methods*. Before each manuscript, the graphical abstract and highlights are given. Though not given in full in this chapter, two first-author conference proceedings manuscripts have also been published on this topic: reference 80 discusses the non-rigid registration pipeline in more detail and reference 79 compares ethanol dehydration and paraffin embedding based on follow-up measurements with $0.65\ \mu\text{m}$ pixel size.

Part 1: Data acquisition, anatomical feature segmentation, tracking global volume and density changes



- Three-dimensional imaging with $(3\ \mu\text{m})^3$ -voxels of a murine brain *post mortem*
- Hard X-ray virtual histology of one entire mouse brain in four embedding media
- Segmentation to quantify non-uniform brain shrinkage
- X-ray contrast improves by ethanol dehydration and paraffin embedding

Published in *Journal of Neuroscience Methods*



ELSEVIER

Contents lists available at ScienceDirect

Journal of Neuroscience Methods

journal homepage: www.elsevier.com/locate/jneumeth

Virtual histology of an entire mouse brain from formalin fixation to paraffin embedding. Part 1: Data acquisition, anatomical feature segmentation, tracking global volume and density changes

Griffin Rodgers^{a,b}, Willy Kuo^{c,d}, Georg Schulz^{a,b}, Mario Scheel^e, Alexandra Migga^{a,b}, Christos Bikis^{a,b,f}, Christine Tanner^{a,b,*}¹, Vartan Kurtcuoglu^{c,d}, Timm Weitkamp^e, Bert Müller^{a,b}

^a Biomaterials Science Center, Department of Biomedical Engineering, University of Basel, 4123 Allschwil, Switzerland

^b Biomaterials Science Center, Department of Clinical Research, University Hospital Basel, 4031 Basel, Switzerland

^c The Interface Group, Institute of Physiology, University of Zurich, 8057 Zurich, Switzerland

^d National Centre of Competence in Research, Kidney.CH, 8057 Zurich, Switzerland

^e Synchrotron Soleil, 91192 Gif-sur-Yvette, France

^f Integrierte Psychiatrie Winterthur – Zürcher Unterland, 8408 Winterthur, Switzerland

ARTICLE INFO

Keywords:

Hard X-ray computed tomography
Synchrotron radiation-based microtomography
Virtual histology
Ethanol dehydration
Paraffin embedding
Volume shrinkage

ABSTRACT

Background: Micrometer-resolution neuroimaging with gold-standard conventional histology requires tissue fixation and embedding. The exchange of solvents for the creation of sectionable paraffin blocks modifies tissue density and generates non-uniform brain shrinkage.

New method: We employed synchrotron radiation-based X-ray microtomography for slicing- and label-free virtual histology of the mouse brain at different stages of the standard preparation protocol from formalin fixation via ascending ethanol solutions and xylene to paraffin embedding. Segmentation of anatomical regions allowed us to quantify non-uniform tissue shrinkage. Global and local changes in X-ray absorption gave insight into contrast enhancement for virtual histology.

Results: The volume of the entire mouse brain was 60%, 56%, and 40% of that in formalin for, respectively, 100% ethanol, xylene, and paraffin. The volume changes of anatomical regions such as the hippocampus, anterior commissure, and ventricles differ from the global volume change. X-ray absorption of the full brain decreased, while local absorption differences increased, resulting in enhanced contrast for virtual histology. These trends were also observed with laboratory microtomography measurements.

Comparison with existing methods: Microtomography provided sub-10 μm spatial resolution with sufficient density resolution to resolve anatomical structures at each step of the embedding protocol. The spatial resolution of conventional computed tomography and magnetic resonance microscopy is an order of magnitude lower and both do not match the contrast of microtomography over the entire embedding protocol. Unlike feature-to-feature or total volume measurements, our approach allows for calculation of volume change based on segmentation.

Conclusion: We present isotropic micrometer-resolution imaging to quantify morphology and composition changes in a mouse brain during the standard histological preparation. The proposed method can be employed to identify the most appropriate embedding medium for anatomical feature visualization, to reveal the basis for the dramatic X-ray contrast enhancement observed in numerous embedded tissues, and to quantify morphological changes during tissue fixation and embedding.

* Corresponding author at: Biomaterials Science Center, Department of Biomedical Engineering, University of Basel, 4123 Allschwil, Switzerland.

E-mail address: christine.tanner@unibas.ch (C. Tanner).

¹ www.bmc.unibas.ch

<https://doi.org/10.1016/j.jneumeth.2021.109354>

Received 15 July 2021; Received in revised form 1 September 2021; Accepted 4 September 2021

Available online 13 September 2021

0165-0270/© 2021 The Authors. Published by Elsevier B.V. This is an open access article under the CC BY license (<http://creativecommons.org/licenses/by/4.0/>).

1. Introduction

The micro- and nano-morphology of the neuronal network is closely related to brain function. Therefore, (sub-)cellular imaging plays a crucial role in understanding the brain in health and disease. The gold standard for sub-micrometer histological analysis involves tissue fixation, embedding, sectioning, staining, and imaging with light or electron microscopy (Culling, 1974). Benefits of optical microscopy include fast imaging in two dimensions and well-established histochemical staining protocols for function-related contrast and differentiation of anatomical features. A drawback is that physical slicing is irreversible and introduces artifacts (Pichat et al., 2018; Germann et al., 2008). Volumetric histological imaging relies on serial sectioning, which typically provides anisotropic spatial resolution limited by the section thickness and true micrometer resolution is time consuming (Amunts et al., 2013; Gong et al., 2013).

Thanks to the penetration of hard X-rays through matter, micro-tomography offers a complementary three-dimensional neuroimaging approach that generates isotropic micrometer resolution without serial sectioning. The X-ray absorption of soft tissues is weak, which is why microtomography of brain tissue has traditionally relied on contrast agents. Staining for cells with heavy metal compounds such as silver nitrate has allowed for impressive visualization of the cytoarchitecture of the brain (Mizutani et al., 2008; Mizutani and Suzuki, 2012). Many protocols have been suggested including osmium-based (Böhm et al., 2019; Barbone et al., 2020), iodine-based (Anderson and Maga, 2015; Saccomano et al., 2018), and Golgi-Cox mercury-based impregnation (Fonseca et al., 2018; Jiang et al., 2021). Unfortunately, selection and usage of X-ray contrast agents is sample- and target-specific, hence presenting a barrier for non-experts.

X-ray phase contrast methods at synchrotron radiation facilities offer higher density resolution than absorption contrast (Momose, 2005), allowing for imaging of the minute native density differences in brain tissue without staining (Schulz et al., 2010; Pinzer et al., 2012). This has enabled label-free imaging of cyto- and angioarchitecture of whole rodent brains (Zhang et al., 2018; Barbone et al., 2018). It has also been used for the quantitative analysis of cytoarchitecture within neuronal volumes up to tens of mm^3 in size for mice and humans (Dyer et al., 2017; Hieber et al., 2016; Töpperwien et al., 2018). Unique possibilities such as capillary-level visualization of amyloid-angiopathy were demonstrated in a mouse brain model of Alzheimer's disease (Massimi et al., 2019). Advances in computing power and acquisition techniques have allowed for imaging of the full mouse brain at around $1 \mu\text{m}$ resolution, though the related datasets are not thoroughly presented in the literature (Vescovi, 2018; Miettinen et al., 2019). These developments are contributing to the rise of X-ray virtual histology (Albers et al., 2018a), which can complement standard histology as part of a multi-modal imaging strategy (Uludağ and Roebroek, 2014; Katsamenis et al., 2019). Still, the limited accessibility of synchrotron radiation sources prevents more widespread use. Recently, state-of-the-art laboratory X-ray sources have demonstrated promising results for virtual histology (Albers et al., 2018b; Vågberg et al., 2018; Busse et al., 2018; Zdora et al., 2020) including cellular-resolution neuroimaging (Töpperwien et al., 2018; Töpperwien and van der Meer, 2020), but these systems are still not commonplace.

Fortunately, the modified electron density of brain tissue fixed in ethanol or embedded in paraffin (Töpperwien et al., 2019) allows for the use of conventional laboratory-based absorption-contrast systems for virtual histology (Khimchenko et al., 2016). Paraffin embedding is used in standard histology, meaning well-established preparation protocols exist and virtual histology can be incorporated into the workflow of conventional histology. This allows for validation of virtual histology with well-selected histochemical stains (Töpperwien and van der Meer, 2020) and extension of conventional histology to the third dimension with slice-to-volume registration (Khimchenko et al., 2016; Chicherova et al., 2018). Thus, paraffin embedding is becoming increasingly popular

among the X-ray imaging community, even for imaging beyond the optical limit (Khimchenko et al., 2018; Kuan et al., 2020).

Each step of the paraffin embedding protocol introduces significant tissue shrinkage. This effect is well known, but quantification of shrinkage has previously been based on length measurements of dissected tissue (Quester and Schröder, 1997). Volume change measurements based on computed tomography and magnetic resonance imaging (MRI) have been reported (Wehrl et al., 2015), however higher spatial and density resolution are needed for the quantification of morphology change of smaller anatomical regions within the brain.

The objective of this two-part study is to quantify morphological and density changes within the mouse brain as a result of tissue embedding. To this end, we employ synchrotron radiation-based X-ray micro computed tomography to visualize an entire mouse brain over the course of paraffin embedding, i.e. in formalin, five ascending ethanol solutions (50%, 70%, 80%, 90%, and 100%), xylene, and finally paraffin; see Fig. 1 for the workflow. In this Part 1 manuscript, we report the brain preparation, image acquisition procedure, and semi-automatic segmentation of anatomical features before describing the measured changes in volume and density of selected anatomical regions. Part 2 of this publication (Rodgers et al., 2021a) provides details and validation of the image registration method which is used to extract volumetric strain fields, and reports on the local volume and contrast changes.

2. Materials and methods

2.1. Mouse brain extraction and preparation

All tissue collected in this study was excess material from an experiment approved by the veterinary office of the Canton of Zurich (license number ZH067/17). The brain of one six-month-old female C57BL/6J mouse (Janvier Labs, Le Genest-Saint-Isle, France) was extracted and immersion-fixed with 4% formaldehyde / phosphate buffered saline after sacrifice. The standard paraffin embedding protocol was used (Wolfe, 2019): after immersion in 4% formaldehyde/phosphate buffered saline (Sigma Aldrich, Darmstadt, Germany/Thermo Fisher Scientific, Massachusetts, USA), the brain was immersed for two hours in each of 50%, 70%, 80%, 90%, and 100% ethanol solutions, xylene (20 mL each, Carl Roth GmbH, Karlsruhe, Germany). Finally, the sample was transferred to liquid paraffin wax (ROTI® Plast, Carl Roth GmbH, Karlsruhe, Germany) for two hours, then cooled to form a solid paraffin block.

Between each step, the sample was transferred to a 1.5 mL Eppendorf tube and scanned while immersed in the specific embedding medium. The solidified paraffin block was trimmed to remove excess material and directly glued to the sample holder for tomographic measurement. Fig. 1 shows a sketch of the sequence of sample preparation and experimental set-up.

2.2. Synchrotron radiation-based X-ray microtomography

Microtomography measurements were performed at the ANATOMIX beamline at Synchrotron SOLEIL (Gif-sur-Yvette, France) (Weitkamp et al., 2017). Here, an undulator gap of 10.3 mm was selected together with a $20 \mu\text{m}$ Au filter to provide X-rays with an effective mean photon energy of around 22 keV. Radiographic projections were acquired with a detector system consisting of a $300 \mu\text{m}$ -thick LuAG scintillator coupled to a scientific CMOS camera (Hamamatsu Orca Flash 4.0 V2, 2048×2048 pixels, $6.5 \mu\text{m}$ physical pixel size) via a lens system made of two photo objectives in tandem geometry (Hasselblad HC 4/210 and HC 2.2/100, numerical aperture of 0.22) resulting in a magnification factor of 2.1 and thus yielding an effective pixel size of $3.1 \mu\text{m}$ (Desjardins et al., 2018). The detector system's resolution is the result of three factors: (i) Nyquist-Shannon sampling theorem, (ii) the Hasselblad objective quality (including mirror, etc.), and (iii) the "blur" within the scintillator. At 22 keV, most X-ray photons are absorbed in the first third of the scintillator: 87.9% (98.5%) of photons are absorbed by a depth of

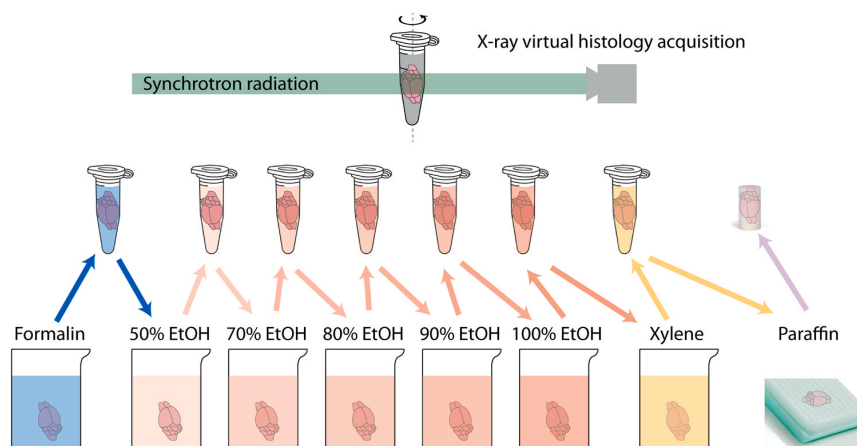


Fig. 1. Virtual histology of an entire mouse brain from formalin fixation to paraffin embedding. Between each step of the standard paraffin embedding protocol, the mouse brain was placed in an Eppendorf tube filled with the embedding media and measured at the ANATOMIX beamline (Synchrotron SOLEIL, Gif-sur-Yvette, France) with pixel length of $3.1 \mu\text{m}$. The final paraffin block was trimmed to a cylinder for measurement.

$108 \mu\text{m}$ ($216 \mu\text{m}$), corresponding to a maximal full width at half maximum blur of 1 pixel (2 pixels). Most well-designed detector systems offer spatial resolution of 2.5–3 pixels. Here, projections of a Siemens star test pattern showed that the setup could resolve a line pair with period just below $10 \mu\text{m}$.

The sample was placed 675 mm upstream of the detector to allow for edge enhancement. For tomographic acquisition, 5,900 projections were acquired over an angular range of 360° with off-axis alignment to nearly double the detector field-of-view. The exposure time was 50 ms per projection. The fly-scan mode was used to minimize overhead. The scan time for a single height step was around seven minutes. Three to four height steps were needed to capture the full sample depending on embedding state. The resulting datasets contained approximately $4,000 \times 4,000 \times 7,000$ voxels and covered a volume of approximately $12 \times 12 \times 21 \text{ mm}^3$.

The selected propagation distance caused edge enhancement, which was desired for the visualization of anatomical structures and interfaces between tissues of similar density. The experimental setup would have allowed for single-distance phase retrieval due to the propagation distance of 675 mm and spatial coherence at the ANATOMIX beamline of Synchrotron SOLEIL. Here, we opted for reconstruction of the linear attenuation coefficient μ , herein referred to as the absorption coefficient, because it does not require *a priori* knowledge of sample composition and filtering for noise reduction can be applied without shifting mean μ -values (Rodgers et al., 2020). Surprisingly, this approach provided sufficient contrast even in the formalin-fixed state despite the low absorption contrast (Schulz et al., 2010). The μ -values measured at interfaces are not considered quantitative since phase effects were present.

For the photon energies and sample size used in this study, the photoelectric effect is the main contributor to X-ray absorption and thus μ is related to the mass density ρ through $\mu \propto \rho Z^4/E^3$, with atomic number Z and photon energy E (Als-Nielsen and McMorrow, 2011). The reconstructed μ -values are thus an approximate measure of mass density ρ , though the impact of phase-contrast phenomena and the energy spectrum used prevent accurate quantitative determination of μ - or ρ -values.

2.3. Dose estimation and potential temperature increase of the mouse brain

The substantial radiation dose during microtomography at synchrotron radiation facilities should not be ignored. Nevertheless, no indication of radiation-induced changes was observed in this study:

projections at same orientation, *i.e.* rotation stage at 0° and 360° , as well as from adjacent height steps showed no noticeable changes in the overlap regions; bubble formation or sample discoloration were not observed; motion artifacts were not present in reconstructions.

The dose was approximated from an estimate of the total flux of the 22 keV-photons per detector pixel. We detected 40,000 and 20,000 counts per pixel without and with the sample, respectively. Considering the acquisition of 5,900 projections with the asymmetric rotation axis, the optical magnification of the detection unit and the scintillator efficiency, the total number of photons per pixel was about 10^8 , the deposited energy was 3 J and the dose was 3 kGy.

The absorbed energy of 3 J in the 1.5 g contents of the Eppendorf container, *i.e.* brain tissue and liquid with a heat capacity of around $4,000 \text{ J kg}^{-1} \text{ K}^{-1}$, would lead to a maximal temperature increase of 0.5 K. This temperature increase gives rise to a linear thermal expansion of one tenth of the pixel length, which is in agreement with the lack of observations mentioned above.

2.4. Tomographic reconstruction

The reconstruction pipeline was implemented in Matlab (release R2020a, The MathWorks, Inc., Natick, USA). Prior to flat- and dark-field correction, radiographic projections were stitched together based on maximum cross-correlation. Ring correction was performed by taking a mean of all projections, applying a low-pass filter to isolate rings, and subtracting the result from the flat-field-corrected projections (a 2D variation of the 1D approach given in *e.g.* (Boin and Haibel, 2006; Miron et al., 2014)). A filtered back-projection with the standard Ram-Lak filter was used for tomographic reconstruction.

Filtering or binning were applied after ring correction to avoid increasing artifact strength (Vo et al., 2018). For the unbinned dataset, Gaussian filtering was used to improve contrast-to-noise at the expense of some spatial resolution (Rodgers et al., 2020). A Gaussian filter with $\sigma = 1.25$ pixels was applied after reconstruction and prior to registration. Additionally, 3×3 and 9×9 binned projections, Gaussian filtered with $\sigma = 1.5$ pixels prior to downsampling, were reconstructed to improve contrast-to-noise and reduce data size (Turner et al., 2004) for memory-intensive computational steps such as non-rigid registration. The $3 \times 3 \times 3$ binned tomographic data with voxel length of $9.3 \mu\text{m}$ have been made publicly available (Rodgers et al., 2021).

2.5. Laboratory-based microtomography

To verify that contrast changes in the brain were observable in pure absorption contrast, an additional mouse brain was measured using a SkyScan 1275 (Bruker, Kontich, Belgium) laboratory microtomography scanner.

The tissue used was excess from an experiment approved by the veterinary office of the Canton of Zurich (license number ZH117/19). One 42 days-old female mouse was euthanized with carbon dioxide then the brain was excised and washed in phosphate buffered saline. The brain was then immersion-fixed in 10% neutral buffered formalin. The mouse line employed was derived from a crossing of three C57BL/6 reporter mouse lines encoding fluorescent proteins that do not impact endogenous gene expression (Yarg, Red5 and Smart13) (Molofsky et al., 2013; Reese et al., 2007; von Moltke, 2016). The mouse line is therefore equivalent to wild-type for the purposes of the current study. The fixation and embedding was performed in the same way as described in Section 2.1.

Laboratory microtomography measurements were taken in formalin, 100% ethanol, xylene, and paraffin. The same parameters were used for all four scans: the acceleration voltage was 25 kVp, electron beam current was 193 μ A, pixel size was 7.5 μ m, exposure time was 305 ms, the mean number of counts per pixel was 58,000 in the reference image, and 720 projections were taken around 360°. Beam hardening correction, ring artifact removal, and tomographic reconstruction were performed with the SkyScan NRecon software package (Version 1.7.4, Bruker, Kontich, Belgium).

2.6. Three-dimensional rendering and segmentation

Segmentation was performed with VGStudio MAX 2.1 (Volume Graphics, Heidelberg, Germany). Adaptive region-growing from user-defined seed points and subsequent morphological operations were used for semi-automatic segmentation of anatomical features. Segmentations were carried out by a single observer based on the Allen Mouse

Brain Atlas (Lein et al., 2007). To understand how over- and under-segmentation impacted the volume of the segmented structures, we morphologically dilated or eroded the single-observer segmentations with spheres of radius 3 voxels for the full brain and radius 1 voxel for the hippocampus, anterior commissure, and ventricles. These radii for dilation or erosion were chosen by the observer as the largest values that still resulted in an acceptable segmentation. The volumes of these dilated/eroded segmentations were used as error bars in Fig. 2 (right). The volume renderings of the segmentations found in Fig. 2 (left) were also generated with VGStudio MAX 2.1 (Volume Graphics, Heidelberg, Germany).

2.7. Quality assurance for data processing pipeline

We identified the following sources of artifacts or losses of data quality during the processing pipeline. Reconstruction (Section 2.4): ring, streak, center-of-rotation, and stitching/blending artifacts. Filtering (Section 2.4): noise, increasing ring artifacts, and over-smoothing. To avoid creating these artifacts, orthogonal slices of all datasets were visually inspected after each processing step. For consistency, parameters were selected only if they allowed for acceptable performance on all datasets.

3. Results

3.1. Global brain shrinkage

The datasets from each of the primary embedding steps (formalin, 100% ethanol, xylene, and paraffin) were manually segmented to track the volume of the full brain, hippocampus, anterior commissure olfactory and temporal limbs (hereafter “anterior commissure”), as well as the lateral and third ventricles (hereafter “ventricles”). The segmentations were based on the Allen Mouse Brain Atlas (Lein et al., 2007). Fig. 2 shows renderings of the segmented regions (left) and measured volumes (right). The measurements were taken from a single brain with

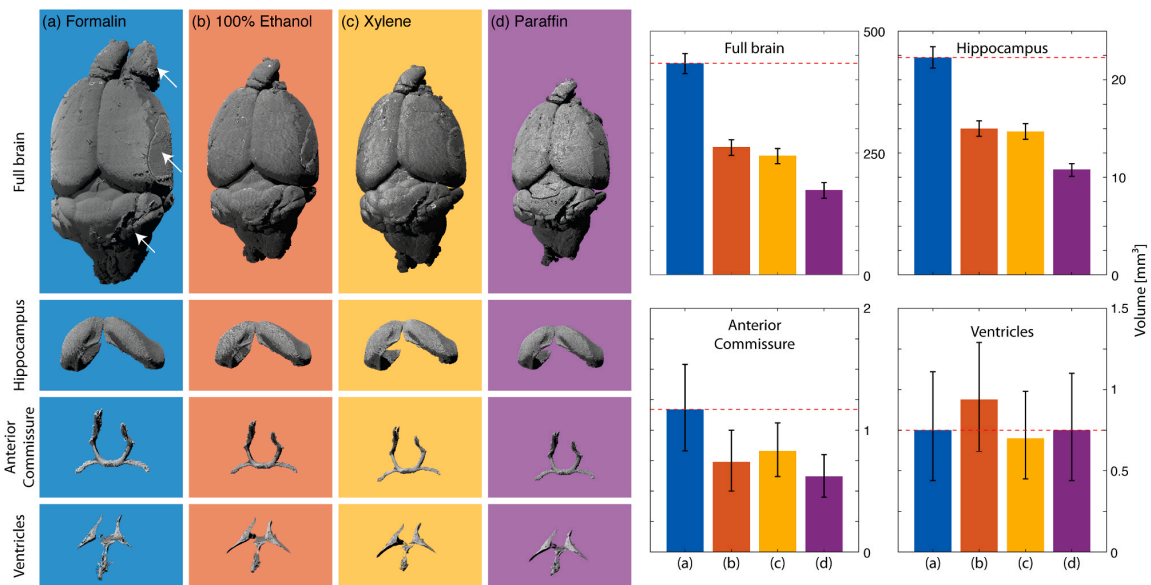


Fig. 2. Brain shrinkage over the course of paraffin embedding. (left) Volume renderings of manually segmented tomographic data are shown for the mouse brain and three selected anatomical regions after (a) formalin fixation, (b) dehydration in ascending alcohol solutions, (c) xylene, and (d) paraffin embedding. Arrows indicate (top) the olfactory lobe, which was broken during sample handling, (middle) the contact between container and brain, and (bottom) a cut on the cerebellum from the extraction of the brain. For reference, the width of the formalin-fixed brain at the middle arrow is about 8.5 mm and all of the renderings have the camera and sample in the same positions. (right) The bar charts show the volumes and estimates of inter-observer segmentation variability as error bars for the selected regions for each embedding step.

error bars representing simulated inter-observer variability. The volumes of the four segmented features and the related volume changes are given in Table 1. The volumes and volume changes are based on segmentations, which are displayed with volume renderings in Fig. 2. The volume changes given in Fig. 2 and Table 1 demonstrate that tissue shrinkage is non-uniform and varies across the selected anatomical features.

3.2. Density changes

In addition to the volume change, a reduction in the X-ray absorption coefficient μ values of the brain tissue and surrounding medium was observed. Histograms of μ for the volumetric datasets of the brain in formalin, 100% ethanol, xylene, and paraffin are displayed in Fig. 3 (left). The shift of the main peak towards lower μ indicates decreased X-ray absorption within the tissue. A broadening of the histogram peak widths indicates an increase in inter-tissue density differences. These changes are also illustrated by axial slices through the datasets with the same grayscale range in Fig. 3 (right). The increase in inter-tissue density differences results in easier differentiation of anatomical features. Despite the mask to isolate the brain tissue, some of the embedding media is reflected in the histogram: formalin solution is more dense than the formalin-fixed brain (right shoulder in histogram) while for the other steps the embedding media are less dense than the brain (smaller peaks on the left side of the histograms).

Table 2 shows the measured absorption coefficients for regions of the cerebellum in formalin, 100% ethanol, xylene, and paraffin. The granular layer, molecular layer, and white matter were manually segmented and the mean values were measured. The absorption coefficient of formalin exceeded those of the other embedding materials. All features of the cerebellum had negative contrast to formalin and positive contrast to 100% ethanol, xylene, and paraffin. Contrast between the three segmented regions of the cerebellum and the surrounding medium increased from formalin to ethanol, xylene, and paraffin. The μ difference between molecular layer and the granular layer increased over the embedding process. Contrast of white matter to granular layer was moderate in formalin and 100% ethanol, and increased in xylene and paraffin. Compared to white matter and the granular layer, the

Table 1

Volumes of the full brain, hippocampus, anterior commissure, and ventricles in the four primary embedding media. Volumes and volume ratio (percentage of volume in formalin) are based on the manual segmentations shown in Fig. 2. The given ranges indicate simulated inter-observer variability. We assume that observers will consistently over- or under-segment the datasets across all embeddings. Therefore, the ranges of volume change correspond to all over- or under-segmented volumes.

	Formalin	100% Ethanol	Xylene	Paraffin
Full brain				
Volume [mm ³]	434	262	244	174
	413–454	245–277	228–259	157–189
Volume Ratio	–	60%	56%	40%
		59–61%	55–57%	38–42%
Hippocampus				
Volume [mm ³]	22.3	15.0	14.7	10.8
	21.2–23.4	14.2–15.8	13.9–15.5	10.1–11.4
Volume Ratio	–	67%	66%	48%
		67–67%	66–66%	48–49%
Anterior Commissure				
Volume [mm ³]	1.17	0.74	0.83	0.62
	0.83–1.54	0.50–1.00	0.62–1.06	0.45–0.80
Volume Ratio	–	63%	71%	53%
		60–65%	75–69%	54–52%
Ventricles				
Volume [mm ³]	0.75	0.94	0.70	0.75
	0.44–1.11	0.62–1.29	0.45–0.99	0.44–1.10
Volume Ratio	–	125%	94%	100%
		141–116%	102–89%	100–99%

absorption coefficient of molecular layer was intermediate for formalin, smaller for ethanol, and intermediate for xylene and paraffin.

Table 3 shows the standard deviation σ of the absorption coefficient within the same regions as Table 2. This gives a measure of texture, or the difference in absorption between extracellular space and microscopic features such as cells, fibers, and vessels. Improved contrast of fine structures was demonstrated by increased σ values from formalin to subsequent steps. For example, the σ for white matter was highest in 100% ethanol. This observation agreed with visual assessment, where the texture of the fiber structures within the white matter was more discernible in 100% ethanol than for the other embedding stages (cf. Fig. 4 bottom). The increased σ of the paraffin was due its granular structure.

3.3. Laboratory- and synchrotron radiation-based microtomography

To confirm that the observed changes in X-ray absorption coefficient were not a result of phase effects, an additional mouse brain was measured in pure absorption mode with a laboratory microtomography system. Fig. 4 (top) shows virtual coronal slices through the cerebellum and brainstem from both laboratory and synchrotron radiation-based microtomography datasets. Magnified views (bottom) highlight the granular layer, molecular layer, white matter, and interposed nucleus of the cerebellum. Both modalities show the same contrast changes over the course of embedding, namely an increasing contrast between brain and surrounding medium, improved contrast between granular and molecular layers over the course of embedding, lower absorption of white matter relative to surrounding tissue in formalin, and increased absorption of white matter in 100% ethanol.

It should be noted that the higher resolution synchrotron radiation-based measurements allowed for differentiation of individual cells, vessels, and fiber tracts. The edge enhancement that is present in the synchrotron radiation datasets improves visualization of these structures. For example, the interposed nucleus of the cerebellum and the Purkinje cell layer (Fig. 4 bottom) can be distinguished in the datasets from ANATOMIX, but appear uniform in the laboratory-based datasets. While both datasets appear to have similar contrast, the synchrotron radiation-based datasets would have significantly higher contrast-to-noise ratio if they were blurred or binned to match the spatial resolution of the laboratory instrument (Rodgers et al., 2020; Thurner et al., 2004).

4. Discussion

Standard histological preparations include the exchange of formalin with alcohol, alcohol with xylene, and xylene with paraffin, a procedure that alters the densities of the affected soft tissues and thereby changes the local X-ray absorption values. Neurons, for example, show significant X-ray contrast enhancement from paraffin embedding, see e.g. (Töpperwien et al., 2019; Khimchenko et al., 2018). In this sense, sample embedding is analogous to staining and should be considered as an experimental parameter to be optimized. The understanding of tissue density and related X-ray contrast changes for the entire brain of animals and humans is therefore desirable, as it will facilitate the selection of embedding state for the visualization of the anatomical structure of interest. In this framework, we combined isotropic micrometer-resolution imaging in three dimensions (Part 1, this paper) with non-rigid registration (Part 2, (Rodgers et al., 2021a)) to quantify morphological and density changes as a result of tissue embedding steps. By way of example, we employed synchrotron radiation-based hard X-ray microtomography to map an entire mouse brain over the course of paraffin embedding, i.e. in formalin, five ascending ethanol solutions, xylene, and finally paraffin. The proposed procedure can be equally employed to any other kind of physically soft tissue with the aim to measure global and local volume changes, to identify the most appropriate embedding medium for feature visualization, and to reveal the basis for the

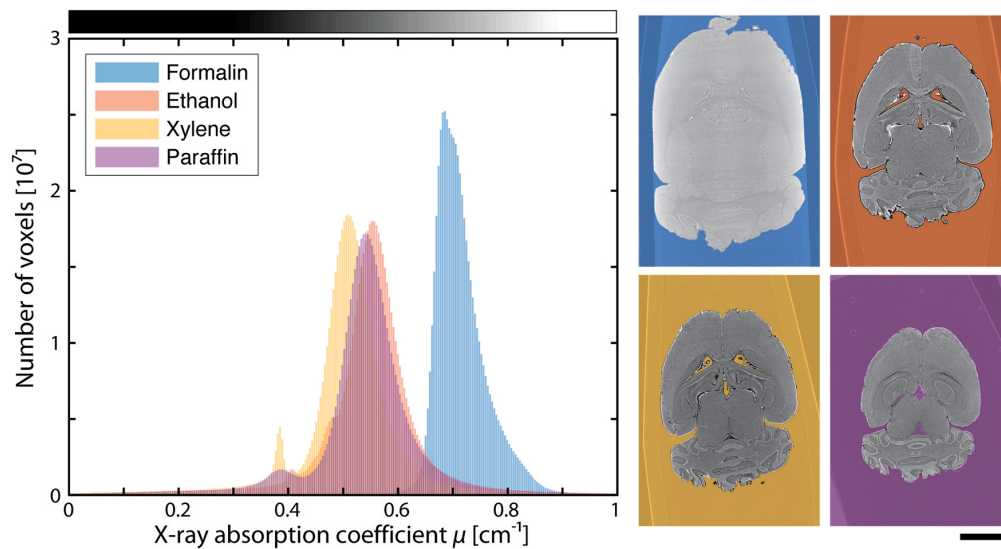


Fig. 3. Global density changes during embedding. Histograms of the X-ray absorption coefficient μ within the brain for several stages of the paraffin embedding protocol. Related axial slices through the original (not registered) datasets are shown with the same grayscale range of $\mu \in [0.3, 0.9] \text{ cm}^{-1}$ as indicated on the histograms. The scale bar for all images is 3 mm. The measurements were taken with the same acquisition parameters. The decrease in mean μ indicates reduced tissue density and the broadening of the peaks indicates increasing separation of tissue densities. The embedding material (semitransparent color overlay on image), which is not completely masked out, accounts for the right shoulder in formalin histogram and the smaller left histogram peaks in the other media.

Table 2

X-ray contrast change in the cerebellum. For the formalin, 100% ethanol, xylene, and paraffin datasets, the mean absorption coefficient μ was measured in manually segmented regions in the granular layer, molecular layer, and white matter of the cerebellum. Contrast between granular layer and both white matter and molecular layer increased with subsequent embedding steps. Molecular layer to white matter contrast was small in 100% ethanol, though texture of white matter increased (see Table 3).

	Mean absorption coefficient $\mu \text{ [cm}^{-1}\text{]}$			
	Embedding material	Molecular layer	Granular layer	White matter
Formalin	0.86	0.83	0.81	0.77
100% Ethanol	0.56	0.71	0.64	0.65
Xylene	0.45	0.69	0.59	0.58
Paraffin	0.45	0.78	0.66	0.62

Table 3

Increasing texture across the embedding process. The standard deviation σ of the absorption coefficient of structures in manually segmented regions of the cerebellum were measured for the formalin, 100% ethanol, xylene, and paraffin datasets. The σ within the selected regions rose as a result of increased density differences between the extracellular space and cells, fibers, vessels, etc. The σ of the embedding material indicates the noise level, except in paraffin, which had a inhomogeneous granular structure.

	Standard deviation $\sigma \text{ [cm}^{-1}\text{]}$			
	Embedding material	Molecular layer	Granular layer	White matter
Formalin	0.05	0.07	0.06	0.07
100% Ethanol	0.05	0.21	0.16	0.20
Xylene	0.05	0.24	0.16	0.16
Paraffin	0.13	0.24	0.19	0.16

dramatic X-ray contrast enhancement observed in numerous embedded tissues.

We have demonstrated X-ray virtual histology for slicing-free imaging of an entire mouse brain after each of the primary steps of tissue preparation for conventional histology, namely fixed in formalin, immersed in ethanol solutions (50%, 70%, 80%, 90%, and 100%), immersed in xylene, and embedded in a paraffin block. These volumetric datasets with voxel length of $3.1 \mu\text{m}$ allowed for analysis of morphological changes and X-ray contrast enhancement. The present study is based on a single mouse brain, thus it is of a preliminary nature compared to MRI-based brain atlases that include six to 20 mice per sex (Dorr et al., 2008). A sample size of a few tens of mice is feasible for future experiments based on the 30 min per brain acquisition time of the synchrotron radiation-based imaging presented here.

X-ray virtual histology provides full brain imaging with near micrometer resolution and reasonable contrast from formalin fixation to paraffin embedding. For *in vivo* studies, however, the radiation dose limitations and the strongly X-ray absorbing skull prevent such high-resolution brain imaging. Therefore, the present study treats the formalin-fixed state as the reference. Fresh tissue imaging would also be possible within a 30-minute scan time, potentially providing a reference point closer to the *in vivo* state. This would, however, present logistical complications related to safety, animal housing, surgery, and timing of experiments. Alternatively, MRI allows for *in vivo* and *post mortem* measurements (Ma et al., 2008), but only reaches a spatial resolution of around 100 micrometers. A combination of the imaging techniques could allow for detailed studies of the changes from the *in vivo* state via formalin fixation to the paraffin embedded state.

We analyzed brain shrinkage during the embedding protocol with two methods: manual segmentation of anatomical features (Part 1) and non-rigid registration (Part 2). The segmentation-based approach allowed for calculation of the volume of the full brain and anatomical regions such as the ventricles, anterior commissure, and the hippocampus (Fig. 2). The improved spatial resolution of microtomography compared to MR microscopy should lead to more accurate segmentations and volume measurements. Multiple independent observers would be needed to fully confirm this hypothesis, whereas the present study

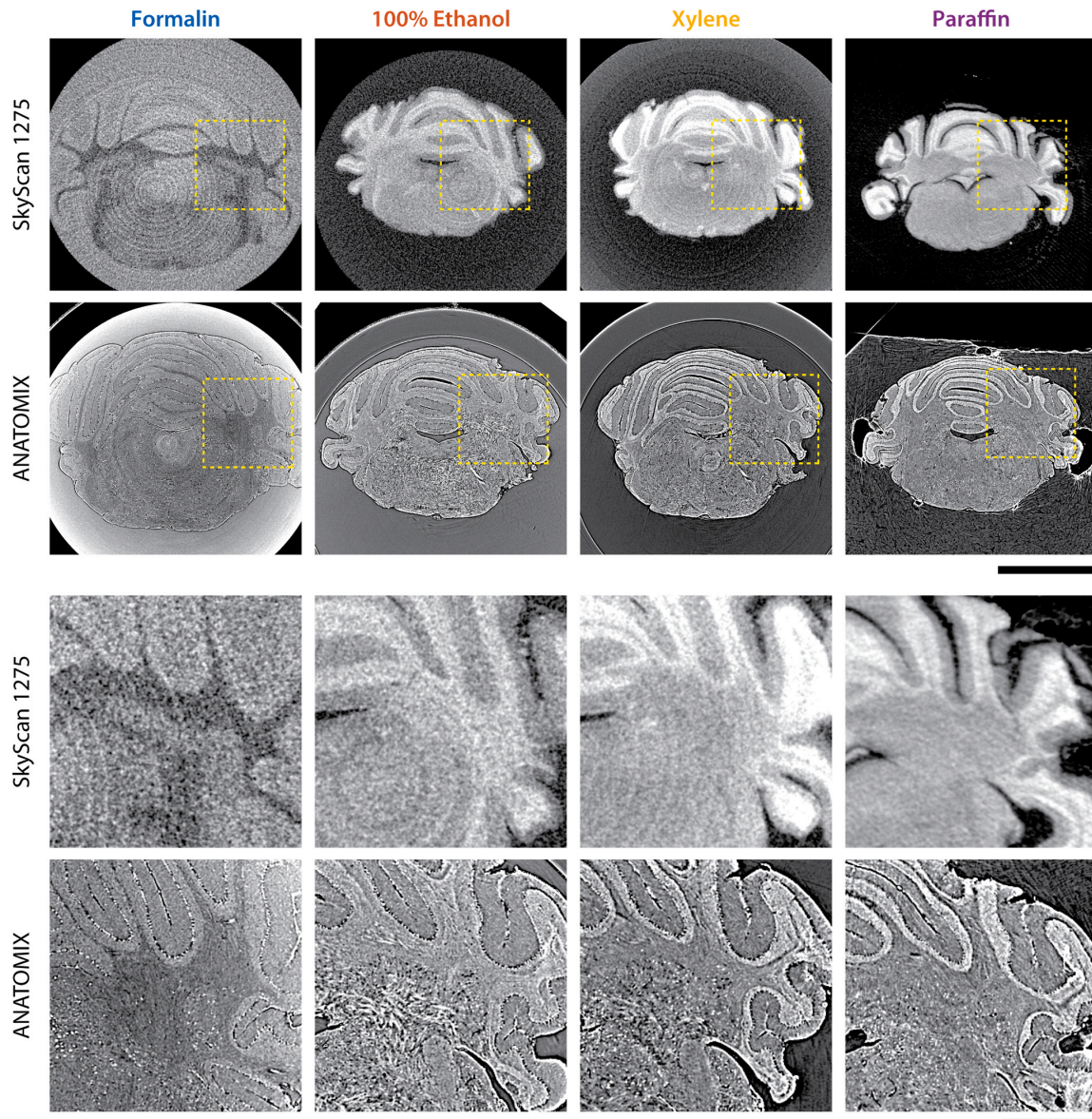


Fig. 4. Comparing tissue contrast in laboratory- and synchrotron radiation-based microtomography of two mouse brains across the embedding media. Similar coronal slices are shown through a mouse brain measured in absorption-contrast mode in a SkyScan 1275 (Bruker, Kontich, Belgium) system and the mouse brain measured at ANATOMIX beamline, Synchrotron SOLEIL (Gif-sur-Yvette, France). These slices contain (top) the cerebellum and the brain stem, while magnified views (bottom) focus on the granular layer, molecular layer, and white matter of the cerebellum, as well as the interposed nucleus. Despite the presence of edge enhancement, the contrast changes observed at ANATOMIX based on reconstructed absorption values are also observed in the laboratory with pure absorption contrast.

was based on a single-observer study and relied on morphological operations to simulate inter-observer variability. Still, the segmentation-based approach was sufficient to determine that volume change was inhomogeneous. Unfortunately, a full characterization of shrinkage with this approach would require extensive segmentation.

Automated segmentation of label-free X-ray microtomography data with cellular resolution is challenging because anatomical borders are often based on connectivity or function and are thus not directly correlated to density. Manual or semi-automatic approaches are required, though ambiguities in anatomical borders cause these approaches to be slow and to suffer from user-specific variability. The

registration approach presented in Part 2 and in (Rodgers et al., 2021b) involves relatively few user interactions. An additional registration between the reference dataset and an appropriate atlas would allow for propagation of all the atlas labels with similar accuracy to the manual approach. This atlas-based segmentation will be more efficient as the number of anatomical features and/or number of datasets increases.

The formalin-fixed brain was squeezed into the Eppendorf container, see Fig. 2. The contact with the container affected tissue up to about 0.5 mm from the edge, see Part 2 Fig. 3.

We acquired a total of nine quasistatic measurements, each after 2 h of immersion in the embedding media, which is a standard immersion

time found in paraffin embedding protocols. Time-resolved volumetric imaging will give a deeper insight into the feature-dependent formation of local strains through the diffusion of the embedding media and its reactions with the tissue components. The current acquisition time was around 30 min, whereas time resolution of around 1 min would be desirable for real-time tracking of shrinkage. Reducing the size of the sample (e.g. a study of tissue punches), the spatial resolution, and/or the signal-to-noise ratio will be necessary to achieve this with currently available instrumentation.

In addition to shrinkage, we analyzed the X-ray absorption changes at each step of the embedding protocol. While the setup allowed for phase retrieval, we analyzed μ because it does not require *a priori* knowledge of sample composition and noise reduction filtering can be applied without shifting mean μ -values (Rodgers et al., 2020). Despite the semi-quantitative nature of the measurement, we can infer composition changes from mean μ of large anatomical regions and texture changes from the standard deviation of μ . To confirm the findings reported here based on a mixture of phase- and absorption-contrast, we performed pure absorption-contrast measurements of a second brain with a laboratory instrument. The results confirmed the observed contrast changes, see Fig. 4.

In preparation steps subsequent to formalin, a decrease in X-ray absorption of both brain tissue and surrounding solutions was observed (Fig. 3). The average absorption decreases of the embedding media compared to formalin are due to a decrease in both density and effective atomic number: formalin (approximated by water, H₂O) has density 0.997 g mL⁻¹, ethanol (C₂H₆O) has density 0.789 g mL⁻¹, xylene (C₈H₁₀) has density 0.864 g mL⁻¹, and paraffin (C_nH_{2n+2}) has density around 0.900 g mL⁻¹. The mean absorption of the brain was not proportional to the embedding medium: the formalin-fixed brain was less than that of formalin, while the brain was higher absorbing than the surrounding medium in ethanol, xylene, and paraffin.

The reduction in mean absorption from formalin to ethanol, xylene, and paraffin is accompanied by an increase in absorption differences between internal structures, evidenced by broadening of histogram peaks in Fig. 3 as well as larger σ values in Table 3. Generally, these changes result in an improved visualization of internal structures with X-ray microtomography for subsequent embedding steps.

Interestingly, the relative absorption values of tissues change substantially from one embedding step to the next: subsequent steps show enhanced or in some cases inverted contrast between internal structures (Table 2). This indicates an embedding medium can be selected to best highlight a given anatomical feature, analogous to stain selection.

Our results indicate that ethanol immersion or paraffin embedding should generally be favored for microtomography-based virtual histology. Compared to formalin, both of these preparations provide X-ray contrast gains within the brain and from the brain to the surrounding medium. These properties also simplify alignment and navigation during imaging. The global decrease in absorption allows for the selection of a lower photon energy to improve density resolution. Töpperwien and co-workers have also noted that compared to formalin, both ethanol and paraffin embedding provide improved contrast for imaging individual cells (Töpperwien et al., 2019). From a practical standpoint, the paraffin embedded state is the simplest to handle and measure. Formalin and xylene both pose health risks and the selection of organic solvent resistant container is an additional requirement for xylene. Future studies should consider the radiation resistance of the embedding media presented here, particularly under higher doses necessary for X-ray nanotomography of brain tissue (Khimchenko et al., 2018; Kuan et al., 2020) as it is scaled towards macroscopic specimens (Du et al., 2021).

All of the specimen preparation steps studied here are compatible with prior *in vivo* MRI or subsequent conventional histology. In principle, non-rigid registration of high resolution virtual histology data to *in vivo* MRI (Fratini et al., 2020) could allow for correction of deformations due to death, fixation, and subsequent tissue treatment. In this case, formalin offers the smallest deformations, though difficulty of

registration may be increased by lower image quality. Paraffin embedding offers the smallest deformations in the case of slice-to-volume registration of conventional histology to virtual histology (Chicherova et al., 2018; Ferrante and Paragios, 2017).

We have presented staining- and slicing-free X-ray imaging of a full mouse brain with pixel size of 3.1 μ m. For full-field tomographic imaging, the accessible spatial resolution depends on the object size. Additional stitching of data will allow for the measurement of the full mouse brain with a spatial resolution of about one micrometer. X-ray imaging with pixel sizes at or below 1 μ m has been reported in literature, however detailed images of those datasets are not yet publicly accessible (Vescovi, 2018; Miettinen et al., 2019). Based on the present study, a decrease in pixel size to below 1 μ m appears feasible, though the approximately 10-fold increase in measurement time and data size are challenges. Increasing spatial resolution with fixed image quality will dramatically increase dose, therefore radiation damage may be observed for such measurements. The current results and extensions to higher resolution suggest that microtomography data should be integrated into future mouse brain atlases.

5. Conclusions

We employed slicing-free, three-dimensional virtual histology of a mouse brain to quantify morphology and X-ray contrast changes during the standard protocol for tissue preparation from the formalin-fixed state to the paraffin-embedded state. The mouse brain volume was 60%, 56%, and 40% of that in formalin for 100% ethanol, xylene, and paraffin, respectively. The volume changes of anatomical regions such as the hippocampus, anterior commissure, and ventricles were not proportional to the global volume change. Additionally, subsequent steps of the embedding protocol led to a global decrease in X-ray absorption as well as changes in inter-tissue absorption. These X-ray absorption changes make ethanol immersion or paraffin embedding attractive choices for X-ray microtomography. These virtual histology results can complement mouse brain atlases based on a combination of magnetic resonance microscopy and optical micrographs of serial histological sections.

CRedit author contribution statement

Griffin Rodgers: Conceptualization, Methodology, Software, Formal analysis, Investigation, Data curation, Writing – original draft, Writing – review & editing, Visualization, Funding acquisition. **Willy Kuo:** Methodology, Validation, Investigation, Resources, Writing – review & editing. **Georg Schulz:** Conceptualization, Methodology, Investigation, Writing – review & editing, Visualization, Supervision. **Mario Scheel:** Formal analysis, Investigation, Resources, Writing – review & editing. **Alexandra Migga:** Validation, Formal analysis, Writing – review & editing, Visualization. **Christos Bikis:** Formal analysis, Writing – review & editing. **Christine Tanner:** Writing – review & editing, Visualization, Supervision. **Vartan Kurtcuoglu:** Writing – review & editing, Supervision, Project administration, Funding acquisition. **Timm Weitkamp:** Investigation, Resources, Writing – review & editing, Funding acquisition. **Bert Müller:** Conceptualization, Methodology, Investigation, Resources, Writing – review & editing, Visualization, Supervision, Project administration, Funding acquisition.

Data availability

The tomographic data from all preparation steps are publicly available in a Zenodo repository (<https://doi.org/10.5281/zenodo.4651412>) (Rodgers et al., 2021). The 3 \times downsampled volumes can be immediately downloaded. Due to the large data sizes, the full resolution data will be made available by request to the first author.

Acknowledgment

This work was carried out under Synchrotron SOLEIL experiment No. 20190424. The authors thank J. Perrin and D. Guillaume of the ANATOMIX beamline at Synchrotron SOLEIL for support during the beam time. ANATOMIX is an Equipment of Excellence (EQUIPEX) funded by the Investments for the Future program of the French National Research Agency (ANR), project NanoimagesX, grant no. ANR-11-EQPX-0031. The authors thank V. Meskenaitė and J. de Tenorio of the University of Zurich for providing excess cadavers for sample extraction. W. K. and V.K acknowledge support from the Swiss National Science Foundation via NCCR Kidney.CH and Project No. 153523. G.R., C.T., and B.M. acknowledge support from the Swiss National Science Foundation Project No. 185058.

Declaration of Competing Interest

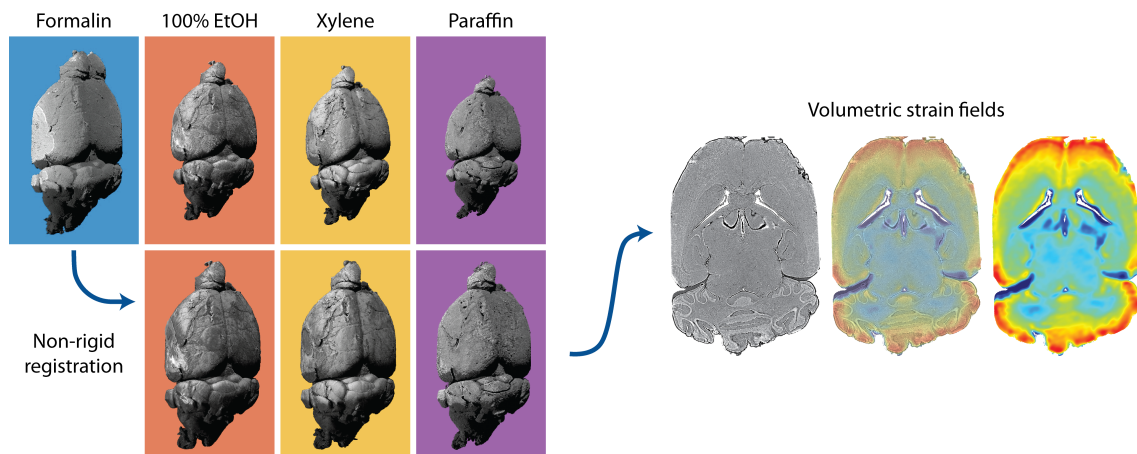
None.

References

- Albers, J., Pacilé, S., Markus, M., Wiart, M., Vande Velde, G., Tromba, G., Dullin, C., 2018a. X-ray-based 3d virtual histology-adding the next dimension to histological analysis. *Mol. Imaging Biol.* 20 (5), 732–741. <https://doi.org/10.1007/s11307-018-1246-3>.
- Albers, J., Markus, M.A., Alves, F., Dullin, C., 2018b. X-ray based virtual histology allows guided sectioning of heavy ion stained murine lungs for histological analysis. *Sci. Rep.* 8 (1), 7712. <https://doi.org/10.1038/s41598-018-26086-0>.
- Als-Nielsen, J., McMorrow, D., 2011. *Elements of Modern X-ray Physics*, second ed. John Wiley & Sons, New York. <https://doi.org/10.1002/9781119998365>.
- Amunts, K., Lepage, C., Borgeat, L., Mohlberg, H., Dickscheid, T., Rousseau, M.-É., Bludau, S., Bazin, P.-L., Lewis, L.B., Oros-Peusquens, A.-M., Shah, N.J., Lippert, T., Zilles, K., Evans, A.C., 2013. BigBrain: an ultrahigh-resolution 3D human brain model. *Science* 340 (6139), 1472–1475. <https://doi.org/10.1126/science.1235381>.
- Anderson, R., Maga, A.M., 2015. A novel procedure for rapid imaging of adult mouse brains with microCT using iodine-based contrast. *PLoS One* 10 (11), e0142974. <https://doi.org/10.1371/journal.pone.0142974>.
- Barbone, G.E., Bravin, A., Romanelli, P., Mittone, A., Bucci, D., Gaaß, T., Le Duc, G., Auweter, S., Reiser, M.F., Kraiger, M.J., Hrabě de Angelis, M., Battaglia, G., Coan, P., 2018. Micro-imaging of brain cancer radiation therapy using phase-contrast computed tomography. *Int. J. Radiat. Oncol. Biol. Phys.* 101 (4), 965–984. <https://doi.org/10.1016/j.ijrobp.2018.03.063>.
- Barbone, G.E., Bravin, A., Mittone, A., Kraiger, M.J., Hrabě de Angelis, M., Bossi, M., Ballarini, E., Rodriguez-Menendez, V., Ceresa, C., Cavaletti, G., Coan, P., 2020. Establishing sample-preparation protocols for X-ray phase-contrast CT of rodent spinal cords: aldehyde fixations and osmium impregnation. *J. Neurosci. Methods* 339, 108744. <https://doi.org/10.1016/j.jneumeth.2020.108744>.
- Böhm, T., Joseph, K., Kirsch, M., Moroni, R., Hilger, A., Osenberg, M., Manke, I., Johnston, M., Stieglitz, T., Hofmann, U.G., Haas, C.A., Thiele, S., 2019. Quantitative synchrotron X-ray tomography of the material-tissue interface in rat cortex implanted with neural probes. *Sci. Rep.* 9 (1), 7646. <https://doi.org/10.1038/s41598-019-42544-9>.
- Boin, M., Haibel, A., 2006. Compensation of ring artefacts in synchrotron tomographic images. *Opt. Express* 14 (25), 12071–12075. <https://doi.org/10.1364/OE.14.012071>.
- Busse, M., Müller, M., Kimm, M.A., Ferstl, S., Allner, S., Achterhold, K., Herzen, J., Pfeiffer, F., 2018. Three-dimensional virtual histology enabled through cytoplasm-specific X-ray stain for microscopic and nanoscopic computed tomography. *Proc. Natl. Acad. Sci. USA* 115 (10), 2293–2298. <https://doi.org/10.1073/pnas.1720862115>.
- de Castro Fonseca, M., Araujo, B.H.S., Dias, C.S.B., Archilha, N.L., Neto, D.P.A., Cavalheiro, E., Westfahl, H., daSilva, A.J., Franchini, K.G., 2018. High-resolution synchrotron-based X-ray microtomography as a tool to unveil the three-dimensional neuronal architecture of the brain. *Sci. Rep.* 8 (1), 12074. <https://doi.org/10.1038/s41598-018-30501-x>.
- Chicherova, N., Hieber, S., Khimchenko, A., Bikis, C., Müller, B., Cattin, P., 2018. Automatic deformable registration of histological slides to μ CT volume data. *J. Microsc.* 271 (1), 49–61. <https://doi.org/10.1111/jmi.12692>.
- Culling, C., 1974. *Methods of examination of tissues and cells*. In: Culling, C. (Ed.), *Handbook of Histopathological and Histochemical Techniques*, third ed. Butterworth-Heinemann, pp. 19–25. <https://doi.org/10.1016/B978-0-407-72901-8.50009-3>.
- D. Desjardins, A. Carcy, J. Giorgetta, C. Meneglier, M. Scheel, T. Weitkamp, Design of Indirect X-Ray Detectors for Tomography on the Anatomix Beamline, in: Proc. 10th Mechanical Engineering Design of Synchrotron Radiation Equipment and Instrumentation (MEDSIA18), Paris, France, 25–29 June 2018, no. 10 in Mechanical Engineering Design of Synchrotron Radiation Equipment and Instrumentation, JACoW Publishing, 2018, pp. 355–357. doi: 10.18429/JACoW-MEDSI2018-THP09.
- Dorr, A., Lerch, J., Spring, S., Kabani, N., Henkelman, R., 2008. High resolution three-dimensional brain atlas using an average magnetic resonance image of 40 adult c57bl/6j mice. *NeuroImage* 42 (1), 60–69. <https://doi.org/10.1016/j.neuroimage.2008.03.037>.
- Du, M., Di, Z., Gürsoy, D., Xian, R.P., Kozorovitskiy, Y., Jacobsen, C., 2021. Upscaling X-ray nanoimaging to macroscopic specimens. *J. Appl. Cryst.* 54 (2), 386–401. <https://doi.org/10.1107/S1600576721000194>.
- Dyer, E.L., GrayRonal, W., Prasad, J.A., Fernandes, H.L., Gürsoy, D., De Andrade, V., Fezzaa, K., Xiao, X., Vogelstein, J.T., Jacobsen, C., Kording, K.P., Kasthuri, N., 2017. Quantifying mesoscale neuroanatomy using X-ray microtomography. *eNeuro* 4 (5). <https://doi.org/10.1523/ENEURO.0195-17.2017>.
- Ferrante, E., Paragios, N., 2017. Slice-to-volume medical image registration: a survey. *Med. Image Anal.* 39, 101–123. <https://doi.org/10.1016/j.media.2017.04.010>.
- Fratini, M., Abdollahzadeh, A., DiNuzzo, M., Salo, R.A., Maugeri, L., Cedola, A., Giove, F., Gröhn, O., Tohka, J., Sierra, A., 2020. Multiscale imaging approach for studying the central nervous system: methodology and perspective. *Front. Neurosci.* 14, 72. <https://doi.org/10.3389/fnins.2020.00072>.
- Germann, M., Morel, A., Beckmann, F., Andronache, A., Jeanmonod, D., Müller, B., 2008. Strain fields in histological slices of brain tissue determined by synchrotron radiation-based micro computed tomography. *J. Neurosci. Methods* 170 (1), 149–155. <https://doi.org/10.1016/j.jneumeth.2008.01.011>.
- Gong, H., Zeng, S., Yan, C., Lv, X., Yang, Z., Xu, T., Feng, Z., Ding, W., Qi, X., Li, A., Wu, J., Luo, Q., 2013. Continuously tracing brain-wide long-distance axonal projections in mice at a one-micron voxel resolution. *NeuroImage* 74, 87–98. <https://doi.org/10.1016/j.neuroimage.2013.02.005>.
- Hieber, S.E., Bikis, C., Khimchenko, A., Schweighauser, G., Hench, J., Chicherova, N., Schulz, G., Müller, B., 2016. Tomographic brain imaging with nucleolar detail and automatic cell counting. *Sci. Rep.* 6, 32156. <https://doi.org/10.1038/srep32156>.
- Jiang, L., Li, C., Li, M., Yin, X., Wu, T., Duan, C., Cao, Y., Lu, H., Hu, J., 2021. Simultaneous 3D visualization of the microvascular and neural network in mouse spinal cord using synchrotron radiation micro-computed tomography. *Neurosci. Bull.* <https://doi.org/10.1007/s12264-021-00715-7>.
- Katsamenis, O.L., Olding, M., Warner, J.A., Chatelet, D.S., Jones, M.G., Sgalla, G., Smit, B., Larkin, O.J., Haig, I., Richeldi, L., Sinclair, I., Lackie, P.M., Schneider, P., 2019. X-ray micro-computed tomography for nondestructive three-dimensional (3D) X-ray histology. *Am. J. Pathol.* 189 (8), 1608–1620. <https://doi.org/10.1016/j.ajpath.2019.05.004>.
- Khimchenko, A., Deyhle, H., Schulz, G., Schweighauser, G., Hench, J., Chicherova, N., Bikis, C., Hieber, S.E., Müller, B., 2016. Extending two-dimensional histology into the third dimension through conventional micro computed tomography. *NeuroImage* 139, 26–36. <https://doi.org/10.1016/j.neuroimage.2016.06.005>.
- Khimchenko, A., Bikis, C., Pacureanu, A., Hieber, S.E., Thalman, P., Deyhle, H., Schweighauser, G., Hench, J., Frank, S., Müller-Gerbl, M., Schulz, G., Cloetens, P., Müller, B., 2018. Hard X-ray nanoholography: large-scale, label-free, 3D nanoimaging beyond optical limit. *Adv. Sci.* 5 (6), 1700694. <https://doi.org/10.1002/adv.201700694>.
- Kuan, A.T., Phelps, J.S., Thomas, L.A., Nguyen, T.M., Han, J., Chen, C.-L., Azevedo, A.W., Tuthill, J.C., Funke, J., Cloetens, P., Pacureanu, A., Lee, W.-C.A., 2020. Dense neuronal reconstruction through X-ray holographic nano-tomography. *Nat. Neurosci.* 23 (12), 1637–1643. <https://doi.org/10.1038/s41593-020-0704-9>.
- Lein, E.S., Hawrylycz, M.J., Ao, N., Ayres, M., Bensinger, A., Bernard, A., Boe, A.F., Boguski, M.S., Brockway, K.S., Byrnes, E.J., Chen, L., Chen, L., Chen, T.-M., Chhinn, M., Chong, J., Crook, B.E., Czaplinski, A., Dang, C.N., Datta, S., Dee, N.R., Desaki, A.L., Desta, T., Diep, E., Dolbeare, T.A., Donelan, M.J., Dong, H.-W., Douherty, J.G., Duncan, B.J., Ebbert, A.J., Eichler, G., Estlin, L.K., Faber, C., Facer, B.A., Fields, R., Fischer, S.R., Fliess, T.P., Frensley, C., Gates, S.N., Glattfelder, K.J., Halverson, K.R., Hart, M.R., Hohmann, J.G., Howell, M.P., Jeung, D.P., Johnson, R.A., Karr, P.T., Kawai, R., Klemm, J.M., Knapik, R.H., Kuan, C.L., Lake, J.H., Laramee, A.R., Larsen, K.D., Lau, C., Lemon, T.A., Liang, A.J., Liu, Y., Luong, L.T., Michaels, J., Morgan, J.J., Morgan, R.J., Mortrud, M.T., Mosqueda, N.F., Ng, L.L., Ng, R., Orta, G.J., Overly, C.C., Pak, T.H., Parry, S.E., Pathak, S.D., Pearson, O.C., Puchalski, R.B., Riley, Z.L., Rockett, H.R., Rowland, S.A., Royall, J.J., Ruiz, M.J., Sarno, N.R., Schaffnit, K., Shapovalova, N.V., Sivisay, T., Slaughterbeck, C.R., Smith, S.C., Smith, K.A., Smith, B.I., Sodt, A.J., Stewart, N.N., Stumpf, K.-R., Sunkin, S.M., Sutram, M., Tam, A., Teemer, C.D., Thaller, C., Thompson, C.L., Varnam, L.R., Visel, A., Whitlock, R.M., Wahnoutka, P.E., Wolkey, C.K., Wong, V.Y., Wood, M., Yaylaoglu, M.B., Young, R.C., Youngstrom, B. L., Feng Yuan, X., Zhang, B., Zwingman, T.A., Jones, A.R., 2007. Genome-wide atlas 971 of gene expression in the adult mouse brain. *Nature* 445, 168–176. <https://doi.org/10.1038/nature05453>.
- Ma, Y., Smith, D., Hof, P., Foerster, B., Hamilton, S., Blackband, S., Yu, M., Benveniste, H., 2008. In vivo 3d digital atlas database of the adult c57bl/6j mouse brain by magnetic resonance microscopy. *Front. Neuroanat.* 2, 1. <https://doi.org/10.3389/fnro.05.001.2008>.
- Massimi, L., Bukreeva, I., Santamaria, G., Fratini, M., Corbelli, A., Brun, F., Fumagalli, S., Maugeri, L., Pacureanu, A., Cloetens, P., Pieroni, N., Fioridalo, F., Forloni, G., Uccelli, A., Kerlero de Rosbo, N., Balducci, C., Cedola, A., 2019. Exploring Alzheimer's disease mouse brain through X-ray phase contrast tomography: from the cell to the organ. *NeuroImage* 184, 490–495. <https://doi.org/10.1016/j.neuroimage.2018.09.044>.
- Miettinen, A., Oikonomidis, I.V., Bonnin, A., Stapanoni, M., 2019. NRStitcher: non-rigid stitching of terapixel-scale volumetric images. *Bioinformatics* 35 (24), 5290–5297. <https://doi.org/10.1093/bioinformatics/btz423>.
- Miron, E., Brun, E., Gouillart, E., Tafforeau, P., Kieffer, J., 2014. The PyHST2 hybrid distributed code for high speed tomographic reconstruction with iterative reconstruction and a priori knowledge capabilities. *Nucl. Instrum. Methods Phys.*

- Res., B 324, 41–48. <https://doi.org/10.1016/j.nimb.2013.09.030> (1st International Conference on Tomography of Materials and Structures).
- Mizutani, R., Suzuki, Y., 2012. X-ray microtomography in biology. *Micron* 43 (2), 104–115. <https://doi.org/10.1016/j.micron.2011.10.002>.
- Mizutani, R., Takeuchi, A., Uesugi, K., Ohyama, M., Takekoshi, S., Osamura, R.Y., Suzuki, Y., 2008. Three-dimensional microtomographic imaging of human brain cortex. *Brain Res.* 1199, 53–61. <https://doi.org/10.1016/j.brainres.2008.01.029>.
- Molofsky, A.B., Nussbaum, J.C., Liang, H.-E., Van Dyken, S.J., Cheng, L.E., Mohapatra, A., Chawla, A., Locksley, R.M., 2013. Innate lymphoid type 2 cells sustain visceral adipose tissue eosinophils and alternatively activated macrophages. *J. Exp. Med.* 210 (3), 535–549. <https://doi.org/10.1084/jem.20121964>.
- von Moltke, J., Ji, M., Liang, H.-E., Locksley, R.M., 2016. Tuft-cell-derived IL-25 regulates an intestinal ILC2-epithelial response circuit. *Nature* 529 (7585), 221–225. <https://doi.org/10.1038/nature16161>.
- Momose, A., 2005. Recent advances in X-ray phase imaging. *Jpn. J. Appl. Phys.* 44 (9A), 6355–6367. <https://doi.org/10.1143/jjap.44.6355>.
- Pichat, J., Iglesias, J.E., Yousry, T., Ourselin, S., Modat, M., 2018. A survey of methods for 3D histology reconstruction. *Med. Image Anal.* 46, 73–105. <https://doi.org/10.1016/j.media.2018.02.004>.
- Pinzer, B., Cacquevel, M., Modregger, P., McDonald, S., Bensadoun, J., Thuring, T., Aebischer, P., Stamanoni, M., 2012. Imaging brain amyloid deposition using grating-based differential phase contrast tomography. *NeuroImage* 61 (4), 1336–1346. <https://doi.org/10.1016/j.neuroimage.2012.03.029>.
- Quester, R., Schröder, R., 1997. The shrinkage of the human brain stem during formalin fixation and embedding in paraffin. *J. Neurosci. Methods* 75 (1), 81–89. [https://doi.org/10.1016/S0165-0270\(97\)00050-2](https://doi.org/10.1016/S0165-0270(97)00050-2).
- Reese, T.A., Liang, H.-E., Tager, A.M., Luster, A.D., Van Rooijen, N., Voehringer, D., Locksley, R.M., 2007. Chitin induces accumulation in tissue of innate immune cells associated with allergy. *Nature* 447 (7140), 92–96. <https://doi.org/10.1038/nature05746>.
- G. Rodgers, G. Schulz, W. Kuo, C. Tanner, B. Müller, Microtomography of a mouse brain from formalin fixed to paraffin embedded: datasets and registration parameters, 2021, March, doi: 10.5281/zenodo.4651412.
- Rodgers, G., Schulz, G., Deyhle, H., Kuo, W., Rau, C., Weitkamp, T., Müller, B., 2020. Optimizing contrast and spatial resolution in hard X-ray tomography of medically relevant tissues. *Appl. Phys. Lett.* 116 (2), 023702 <https://doi.org/10.1063/1.5133742>.
- Rodgers, G., Tanner, C., Schulz, G., Migga, A., Kuo, W., Bikis, C., Scheel, M., Kurtcuoglu, V., Weitkamp, T., Müller, B., 2021a. Virtual histology of an entire mouse brain from formalin fixation to paraffin embedding. Part 2: volumetric strain fields and local contrast changes. *J. Neurosci. Methods*.
- Rodgers, G., Schulz, G., Kuo, W., Scheel, M., Kurtcuoglu, V., Weitkamp, T., Müller, B., Tanner, C., 2021b. Non-rigid registration to determine strain fields during mouse brain fixation and embedding. *Proc. SPIE* 11586 (11586I), 55–65. <https://doi.org/10.1117/12.2583632>.
- Saccomano, M., Albers, J., Tromba, G., Dobrivojević Radmilović, M., Gajović, S., Alves, F., Dullin, C., 2018. Synchrotron inline phase contrast μ CT enables detailed virtual histology of embedded soft-tissue samples with and without staining. *J. Synchrotron Radiat.* 25 (4), 1153–1161. <https://doi.org/10.1107/S1600577518005489>.
- Schulz, G., Weitkamp, T., Zanette, I., Pfeiffer, F., Beckmann, F., David, C., Rutishauser, S., Reznikova, E., Müller, B., 2010. High-resolution tomographic imaging of a human cerebellum: comparison of absorption and grating-based phase contrast. *J. R. Soc. Interface* 7 (53), 1665–1676. <https://doi.org/10.1098/rsif.2010.0281>.
- Thurner, P., Beckmann, F., Müller, B., 2004. An optimization procedure for spatial and density resolution in hard X-ray micro-computed tomography. *Nucl. Instrum. Methods Phys. Res. B* 225 (4), 599–603. <https://doi.org/10.1016/j.nimb.2004.05.027>.
- Töpperwien, M., van der Meer, F., Stadelmann, C., Salditt, T., 2018. Three-dimensional virtual histology of human cerebellum by X-ray phase-contrast tomography. *Proc. Natl. Acad. Sci. USA* 115 (27), 6940–6945. <https://doi.org/10.1073/pnas.1801678115>.
- Töpperwien, M., Markus, A., Alves, F., Salditt, T., 2019. Contrast enhancement for visualizing neuronal cytoarchitecture by propagation-based X-ray phase-contrast tomography. *NeuroImage* 199, 70–80. <https://doi.org/10.1016/j.neuroimage.2019.05.043>.
- Töpperwien, M., van der Meer, F., Stadelmann, C., Salditt, T., 2020. Correlative X-ray phase-contrast tomography and histology of human brain tissue affected by alzheimers disease. *NeuroImage* 210, 116523. <https://doi.org/10.1016/j.neuroimage.2020.116523>.
- Uludag, K., Roebroek, A., 2014. General overview on the merits of multimodal neuroimaging data fusion. *NeuroImage* 102, 3–10. <https://doi.org/10.1016/j.neuroimage.2014.05.018>.
- Vågberg, W., Persson, J., Szekely, L., Hertz, H.M., 2018. Cellular-resolution 3D virtual histology of human coronary arteries using X-ray phase tomography. *Sci. Rep.* 8 (1), 11014. <https://doi.org/10.1038/s41598-018-29344-3>.
- Vescovi, R., Du, M., de Andrade, V., Scullin, W., Gürsoy, D., Jacobsen, C., 2018. Tomosaic: efficient acquisition and reconstruction of teravoxel tomography data using limited-size synchrotron X-ray beams. *J. Synchrotron Radiat.* 25 (5), 1478–1489. <https://doi.org/10.1107/S1600577518010093>.
- Vo, N.T., Atwood, R.C., Drakopoulos, M., 2018. Superior techniques for eliminating ring artifacts in X-ray micro-tomography. *Opt. Express* 26 (22), 28396–28412. <https://doi.org/10.1364/OE.26.028396>.
- Wehrli, H., Bezrukov, I., Wiehr, S., Lehnhoff, M., Fuchs, K., Mannheim, J., Quintanilla-Martinez, L., Kohlhöfer, U., Kneilling, M., Pichler, B., Sauter, A., 2015. Assessment of murine brain tissue shrinkage caused by different histological fixatives using magnetic resonance and computed tomography imaging. *Histol. Histopathol.* 30, 601–613. <https://doi.org/10.14670/HH-30.601>.
- Weitkamp, T., Scheel, M., Giorgetta, J., Joyet, V., Roux, V.L., Cauchon, G., Moreno, T., Polack, F., Thompson, A., Samama, J., 2017. The tomography beamline ANATOMIX at Synchrotron SOLEIL. *J. Phys. Conf. Ser.* 849, 012037 <https://doi.org/10.1088/1742-6596/849/1/012037>.
- Wolfe, D., 2019. 6 – tissue processing. In: *Suvarna, S.K., Layton, C., Bancroft, J.D. (Eds.), Bancroft’s Theory and Practice of Histological Techniques, eighth ed.* Elsevier, pp. 73–83.
- Zdora, M.-C., Thibault, P., Kuo, W., Fernandez, V., Deyhle, H., Vila-Comamala, J., Olbinado, M.P., Rack, A., Lackie, P.M., Katsamenis, O.L., Lawson, M.J., Kurtcuoglu, V., Rau, C., Pfeiffer, F., Zanette, I., 2020. X-ray phase tomography with near-field speckles for three-dimensional virtual histology. *Optica* 7 (9), 1221–1227. <https://doi.org/10.1364/OPTICA.399421>.
- Zhang, M., Zhou, L., Deng, Q.-F., Yuan Xie, Y., Xiao, T., Cao, Y., Zhang, J., Chen, X.-M., zhen Yin, X., Xiao, B., 2015. Ultra-high-resolution 3D digitalized imaging of the cerebral angioarchitecture in rats using synchrotron radiation. *Sci. Rep.* 5, 14982. <https://doi.org/10.1038/srep14982>.

Part 2: Volumetric strain fields and local contrast changes



- Virtual histology of a single mouse brain over the course of standard histological preparation
- Non-rigid registration of embedding-dependent local microanatomy shrinkage
- Quantification of volumetric strain fields of mouse brain
- Increasing fiber tract contrast by a factor of 15 through ethanol dehydration

Published in *Journal of Neuroscience Methods*



ELSEVIER

Contents lists available at ScienceDirect

Journal of Neuroscience Methods

journal homepage: www.elsevier.com/locate/jneumeth

Virtual histology of an entire mouse brain from formalin fixation to paraffin embedding. Part 2: Volumetric strain fields and local contrast changes

Griffin Rodgers^{a,b}, Christine Tanner^{a,b,*}, Georg Schulz^{a,b}, Alexandra Migga^{a,b}, Willy Kuo^{c,d}, Christos Bikis^{a,b,e}, Mario Scheel^f, Vartan Kurtcuoglu^{c,d}, Timm Weitkamp^f, Bert Müller^{a,b}

^a Biomaterials Science Center, Department of Biomedical Engineering, University of Basel, 4123 Allschwil, Switzerland

^b Biomaterials Science Center, Department of Clinical Research, University Hospital Basel, 4031 Basel, Switzerland

^c The Interface Group, Institute of Physiology, University of Zurich, 8057 Zurich, Switzerland

^d National Centre of Competence in Research, Kidney.CH, 8057 Zurich, Switzerland

^e Integrierte Psychiatrie Winterthur – Zürcher Unterland, 8408 Winterthur, Switzerland

^f Synchrotron Soleil, 91192 Gif-sur-Yvette, France

ARTICLE INFO

Keywords:

Synchrotron radiation-based microtomography
Neuroimaging
Non-rigid registration
Non-uniform shrinkage
Embedding media for contrast enhancement in brain tissue

ABSTRACT

Background: Fixation and embedding of *post mortem* brain tissue is a pre-requisite for both gold-standard conventional histology and X-ray virtual histology. This process alters the morphology and density of the brain microanatomy.

New method: To quantify these changes, we employed synchrotron radiation-based hard X-ray tomography with 3 μm voxel length to visualize the same mouse brain after fixation in 4% formalin, immersion in ethanol solutions (50%, 70%, 80%, 90%, and 100%), xylene, and finally after embedding in a paraffin block. The volumetric data were non-rigidly registered to the initial formalin-fixed state to align the microanatomy within the entire mouse brain.

Results: Volumetric strain fields were used to characterize local shrinkage, which was found to depend on the anatomical region and distance to external surface. X-ray contrast was altered and enhanced by preparation-induced inter-tissue density changes. The preparation step can be selected to highlight specific anatomical features. For example, fiber tract contrast is amplified in 100% ethanol.

Comparison with existing methods: Our method provides volumetric strain fields, unlike approaches based on feature-to-feature or volume measurements. Volumetric strain fields are produced by non-rigid registration, which is less labor-intensive and observer-dependent than volume change measurements based on manual segmentations. X-ray microtomography provides spatial resolution at least an order of magnitude higher than magnetic resonance microscopy, allowing for analysis of morphology and density changes within the brain's microanatomy.

Conclusion: Our approach belongs to three-dimensional virtual histology with isotropic micrometer spatial resolution and therefore complements atlases based on a combination of magnetic resonance microscopy and optical micrographs of serial histological sections.

1. Introduction

Histology is the gold standard for investigations of brain microanatomy, as it provides sub-micron resolution in two dimensions with a variety of functional stains (Culling, 1974). Virtual histology based on hard X-ray microtomography (Albers et al., 2018) is an emerging complementary technique that can reveal the brain's cytoarchitecture in three dimensions (Dyer et al., 2017; Hieber et al., 2016; Khimchenko

et al., 2016; Töpperwien et al., 2018, 2020) with isotropic spatial resolution down to and even below the optical limit (Khimchenko et al., 2018; Kuan et al., 2020).

Tissue fixation and embedding are prerequisites for *post mortem* neuroimaging with both conventional and virtual histology. During the standard histological preparation (Culling, 1974), the exchange of formalin with alcohol, alcohol with xylene, and xylene with paraffin alters the densities of physically soft tissues and thereby changes the

* Corresponding author at: Biomaterials Science Center, Department of Biomedical Engineering, University of Basel, 4123 Allschwil, Switzerland.

E-mail address: christine.tanner@unibas.ch (C. Tanner).

<https://doi.org/10.1016/j.jneumeth.2021.109385>

Received 15 July 2021; Accepted 7 October 2021

Available online 9 October 2021

0165-0270/© 2021 The Authors. Published by Elsevier B.V. This is an open access article under the CC BY license (<http://creativecommons.org/licenses/by/4.0/>).

local X-ray absorption coefficient. Neurons, for example, show significant X-ray contrast enhancement from paraffin embedding (Töpperwien et al., 2019). In this sense, sample embedding can be thought of analogously to staining (Müller et al., 2008) and should be considered as an experimental parameter to be optimized (Töpperwien et al., 2019; Strotton et al., 2018). An understanding of tissue density and X-ray contrast changes for the whole brain is therefore desirable, as it would facilitate the selection of embedding state for the visualization of each anatomical structure.

In addition to density changes, paraffin embedding introduces non-uniform shrinkage. Though this has been studied for over a century (Hardy, 1899), until now most studies quantifying shrinkage are based on total volume change or length measurements of tissue sections (Quester and Schröder, 1997). To map shrinkage in three dimensions, a non-destructive volumetric imaging modality is needed. For example, strain fields in the human brain were tracked after extraction from the skull and during formalin fixation with magnetic resonance imaging (MRI) (Schulz et al., 2011). MRI was also used to quantify volume changes of segmented anatomical regions from the *in vivo* state to the formalin fixed state (Ma et al., 2008). Unfortunately, MRI contrast is weak after dehydration for paraffin embedding (Wehrl et al., 2015). Total volume and landmark positions were tracked in MR and computed tomography images to assess shrinkage of the mouse brain with various fixatives (Wehrl et al., 2015). However, all of the above studies lack spatial and density resolution to differentiate effects within smaller anatomical regions.

The objective of this two-part study is to combine isotropic micrometer-resolution imaging with non-rigid registration to quantify morphological and density changes as a result of tissue embedding. To this end, we employ synchrotron radiation-based X-ray micro computed tomography to visualize an entire mouse brain over the course of paraffin embedding, i.e. in formalin, five ascending ethanol solutions (50%, 70%, 80%, 90%, and 100%), xylene, and paraffin. We aim to measure global and local volume change, determine the best embedding medium for visualization of selected anatomical features, and uncover the basis for the dramatic X-ray contrast enhancement observed in embedded tissues.

The first part of this investigation (Rodgers et al., 2021a) reports the brain preparation and paraffin embedding protocol, acquisition and reconstruction of the tomography data from laboratory- and synchrotron radiation-based microtomography, and analysis of volume and density changes of the full brain and segmented anatomical features. Part 2 complements that study by addressing the non-rigid registration of the tomography data, its validation, and the analysis of volumetric strain fields and local contrast changes.

2. Materials and methods

2.1. Sample preparation and data acquisition

A detailed description of the sample preparation, image acquisition, and tomographic reconstruction is presented in Part 1 (Rodgers et al., 2021a).

2.2. Non-rigid registration

The open-source software toolbox `elastix` (Klein et al., 2010; Shamonin et al., 2014) (version 4.9) was used for registration of the tomography data. Registrations were performed on a workstation with an Intel® Xeon® CPU (E5-2637 v2 3.50 GHz) and 144 GB memory. The dataset of the formalin-fixed brain was selected as the reference dataset for all registrations. The non-rigid registration pipeline consisted of three steps: (1) coarse manual affine pre-alignment, (2) automatic multi-resolution affine registration, and (3) automatic multi-resolution B-spline registration. A final rigid transformation (4) was used for displaying the data in anatomical planes.

Step (1) facilitates the automatic registrations by starting from a reasonable alignment. Using the open-source software `ITK-SNAP` (Yushkevich et al., 2006) (version 3.8.0) and the downsampled datasets, three rotation angles, three translations, and one scaling factor were selected for a coarse alignment. Determining these parameters took about one minute per dataset.

The registrations in steps (2) and (3) relied on the 3×3 binned datasets to speed up registration, as the data size of the unbinned reconstructed volumes ranged from 210 to 260 GB for single precision (32-bit depth). Textures and edges were enhanced with a standard deviation filter with $3 \times 3 \times 3$ voxel neighborhood. Background pixels were excluded from the registration optimization to avoid influence of the surrounding medium and sample holder. This was achieved by means of coarse masks created by simple semi-automatic segmentation of the full brain *via* thresholding, morphological closing, and largest connected structure extraction. Mattes mutual information was selected as the similarity measure to account for non-linear intensity changes due to the selected embedding materials. Optimization was based on stochastic gradient descent. The registration parameter files are freely available (Rodgers et al., 2021c).

For step (2), affine registration was done with four resolutions (smoothing and downsampling), 1,000 iterations per resolution, and 65,536 random spatial samples. The number of spatial samples was selected as a compromise between registration speed and fluctuations in the similarity measure due to sample variations. Affine registration of each dataset took around 35 min.

For step (3), non-rigid registration was based on a B-Spline transform, where the displacements at a grid of control points are interpolated by cubic B-Splines. The degrees of freedom are controlled by the grid spacing. We selected a spacing of $12 \times 12 \times 12$ voxels as this choice was the finest grid spacing that allowed the full volume registration to run on a single workstation with 144 GB of RAM and showed sufficient flexibility in initial tests. This approach corresponds to nearly 7 million degrees of freedom. To avoid unrealistic deformations in homogeneous regions, a bending energy term was added to the cost function. The weighting of this regularization term was optimized by plotting the image dissimilarity versus the bending energy after registrations with various grid spacings and weights (Rodgers et al., 2021b). A weight was then chosen which was on the Pareto front and close to the elbow of the resulting L-shape curve (Rodgers et al., 2021b; Hansen, 2000). Five resolutions (smoothing without downsampling) were used with 2,000 iterations each and 131,072 random spatial samples. This registration took around 7.5 h per dataset.

After step (3), all datasets were in the coordinate frame of the formalin dataset. Step (4) applied a rigid transformation to all datasets for display in a desired coordinate frame, i.e. sagittal, axial, and coronal planes. This single transformation was manually determined in `ITK-SNAP` in around one minute.

The datasets were warped only once with the composition of transformations produced in steps (1)-(4). We note that this transformation can be applied to any volume in the same coordinate frame as the floating dataset, for example if an alternative filtering option such as phase retrieval is more desirable for visualization or subsequent analysis. Resampling was done with linear interpolation to avoid over-shoots where edge enhancement is observed. The warping took about 20 min for the $3 \times 3 \times 3$ binned datasets. The entire unbinned dataset could not be warped due to memory limitations, therefore regions of interest were individually warped by applying the transformation from registration of the $3 \times 3 \times 3$ binned dataset.

The voxel-wise volume change as the result of the registrations was calculated from the determinant of the Jacobian of the transformation. The program `transformix` (Klein et al., 2010; Shamonin et al., 2014) (version 4.9) was used to calculate these values for the composition of transformations given from steps (1)-(4). These transformations have been made publicly available along with the $3 \times 3 \times 3$ datasets used for registration (Rodgers et al., 2021c).

2.3. Evaluation of registration accuracy

Validation of non-rigid registration is challenging as the ground truth is unknown and difficult to manually establish (Crum et al., 2003; Schnabel et al., 2003; Pluim et al., 2016). Here, the registration accuracy was qualitatively assessed with visual inspection. Quantitative assessment was based on the Dice Similarity Coefficient (Dice, 1945), median surface-to-surface distance, and volume change error of segmentations of the full brain and ventricles. These structures could be confidently segmented thanks to the contrast between tissue and the embedding material. The metrics were calculated between the reference (formalin) and the transformed segmentations (100% ethanol, xylene, and paraffin).

Consider the reference segmentation S_{ref} , the floating segmentation S_{flo} , and the floating segmentation transformed to the reference space $T(S_{\text{flo}})$ via the transformation T found by registration. The Dice similarity coefficient was defined as

$$DSC = 2|S_{\text{ref}} \cap T(S_{\text{flo}})| / (|S_{\text{ref}}| + |T(S_{\text{flo}})|).$$

The median surface-to-surface distance was defined as

$$d_{\text{med}} = \text{median}\{\mathcal{S}(S_{\text{ref}}, T(S_{\text{flo}})) \cup \mathcal{S}(T(S_{\text{flo}}), S_{\text{ref}})\},$$

where $\mathcal{S}(S_{\text{ref}}, T(S_{\text{flo}}))$ is the set of the shortest distances from all surface points of S_{ref} to the surface of $T(S_{\text{flo}})$. The volume change error was calculated by

$$E_{rV} = rV_{\text{reg}} / rV_{\text{seg}} - 1.$$

Here $rV_{\text{reg}} = V(S_{\text{flo}}) / V(T(S_{\text{flo}}))$ is the volume change ratio using the transformed floating segmentation and $rV_{\text{seg}} = V(S_{\text{flo}}) / V(S_{\text{ref}})$ is the volume change ratio using the reference segmentation.

Dice overlap scores are known to overstate registration quality for large volume segmentations because surface differences have small contributions. Hence, we included median surface-to-surface distances, which are entirely surface-based with the median providing robustness to local segmentation differences. Volume change error was included, as it characterizes the difference between volume change as measured by segmentation vs. registration. For reference, a Dice score of unity indicates perfect overlap and zero indicates no overlap. A surface-to-surface distance of zero indicates precise alignment and large values indicate poor alignment. A volume change error of 0% (+100%) indicates that the volume change measured by registration matches (is two

times larger than) the volume change measured by segmentation.

2.4. Quality assurance for data processing pipeline

We identified the following sources of artefacts or losses of data quality during registration (Section 2.2): overfitting, folding, under- or over-regularization (e.g. wavy or stiff edges). To reduce the risk of these artefacts, orthogonal slices of all datasets were visually inspected after each processing step. For consistency, parameters were selected only if they allowed for acceptable performance on all datasets. We analyzed L-curves to support parameter selection to reduce over- or under-regularization during registration (Rodgers et al., 2021b).

3. Results

3.1. Quality of non-rigid registration

Registration results were visually evaluated within the formalin-fixed and 100% ethanol immersed brain datasets in Figs. 1 and 2. Fig. 1 shows representative virtual axial slices of the reference formalin-fixed dataset (Fig. 1R), the original floating dataset (Fig. 1F), the manually rigid pre-aligned dataset (Fig. 1S1), the automatically affine registered dataset (Fig. 1S2), and the automatically B-spline registered dataset (Fig. 1S3). These selected virtual slices show the steps of registration described in Section 2.2.

The affine registration was characterized by twelve degrees of freedom (three translation, three rotation, three scaling, and three skew parameters) with the same geometric transformation for all voxels and thus a uniform volume change. It resulted in a coarse alignment of the full brain (Fig. 1S2) with many internal features not matching (cf. Fig. 2). The B-spline transform used here contained nearly 7 million degrees of freedom and thus improved on the affine registration with local deformations to match fine structures. This improvement became apparent upon closer visual inspection as depicted for three examples in Fig. 2.

Fig. 2 shows magnified views of the regions of interest highlighted by the dashed yellow squares in Fig. 1R. Overlays are shown to visually compare the performance of automatic affine and automatic B-spline registrations. The B-spline registration showed excellent results within most of the brain, even accurately aligning individual cells (see the hippocampus, top arrow of middle row). Discrepancies were found in regions where large local deformations occurred, e.g. within the



Fig. 1. Registration results. Floating datasets (F, here 100% ethanol) were registered to the reference formalin-fixed dataset (R) via a manual pre-alignment (S1) followed by automatic affine (S2) and then automatic B-spline registration (S3). Affine registration allows for global translation, rotation, scaling, and shearing (12 degrees of freedom), while B-spline allows for local deformations based on displacements of a grid of control points (in this work, about 7 million degrees of freedom were used). A bending energy regularization term was imposed on the B-spline registration to penalize large local deformations. The registration was optimized within full brain masks (shown without color) to avoid influence of the surrounding medium and the sample holder. The yellow dashed boxes show regions of interest for detailed comparison in Fig. 2. The scale bar is 3 mm and the grayscale range is given by mean \pm 2 standard deviations of the intensities in the full brain mask per embedding.

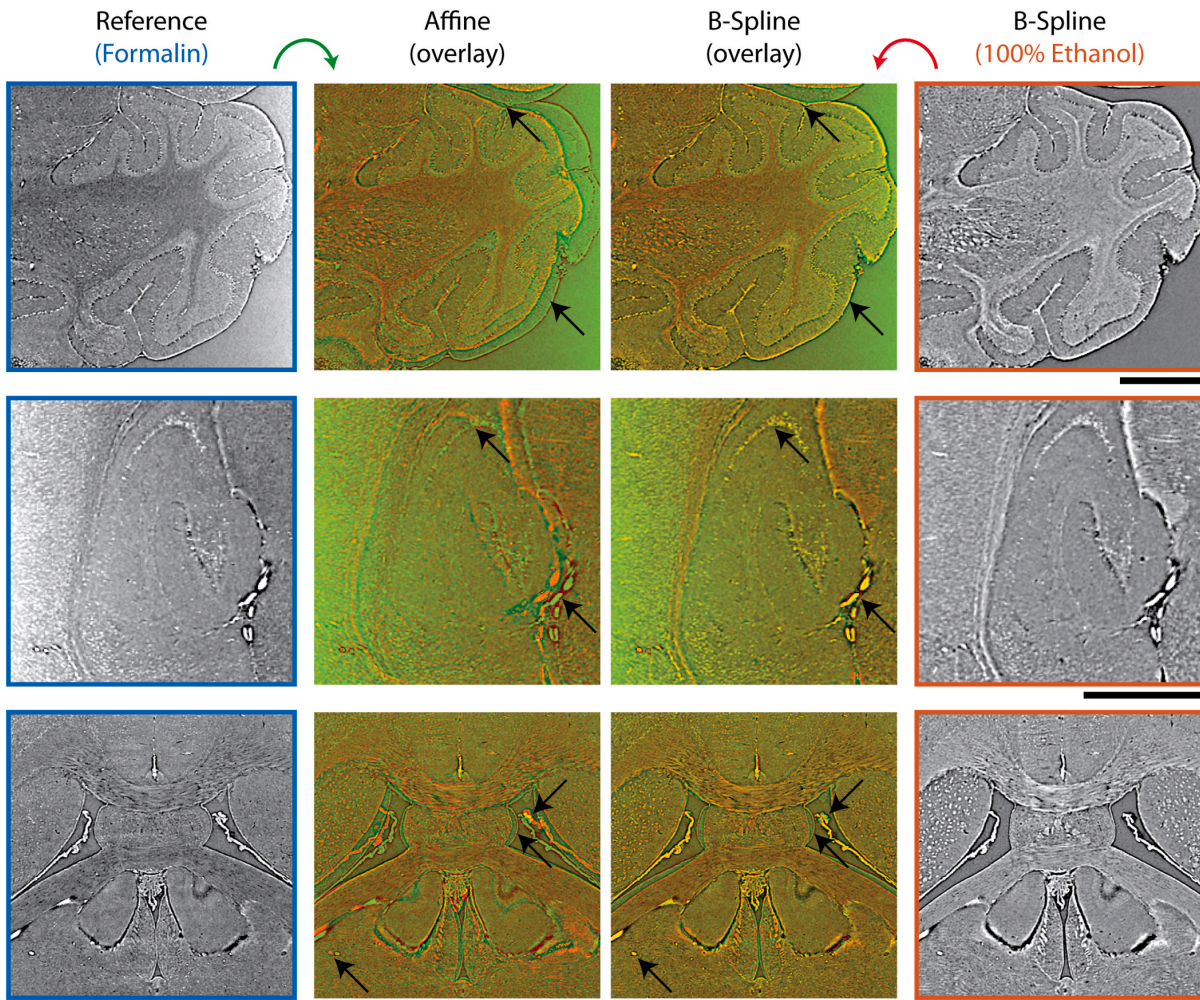


Fig. 2. Comparing affine and non-rigid (B-spline) registration. The three regions of interest marked in Fig. 1 are shown in the reference formalin (column 1) and the B-spline registered 100% ethanol (column 4) datasets. Alignment performance of affine (column 2) and B-spline registrations (column 3) are shown with overlays, green: formalin, red: 100% ethanol. The outer borders of the cerebellum (top) were matched by B-spline (bottom arrow) with the exception of regions of complete collapse or expansion (top arrow); (middle) matching of fine structures near the hippocampus indicates excellent agreement for the B-spline (both arrows); (bottom) the ventricle walls (middle arrow) presented a challenge due to strong local deformations, but nearby regions showed excellent agreement, see e.g. the plexus choroideus (top arrow) or the vessel in the lower left (bottom arrow). All scale bars correspond to 1 mm and the grayscale range is given by mean \pm 2 standard deviations of the intensities in the full brain mask per embedding.

ventricles (bottom row, top arrow), as well as at locations of complete expansion or collapse, e.g. at the border between the cerebellum and cerebral cortex (top row, top arrow).

The registration accuracy was also assessed with Dice overlap, median surface-to-surface distances, and volume difference, see Table 1. Note that the metrics were evaluated on the $3\times$ binned datasets with pixel length of $9.3\ \mu\text{m}$, as this binning factor was used for registration. All metrics showed a substantial registration improvement from affine to B-spline approaches.

3.2. Mapping the local volumetric strain

The determinant of the spatial Jacobian of the transformation found during registration gives the volume change ratio (corresponding to the floating volume divided by reference volume, i.e. $V(I_{\text{flo}}(x))/V(I_{\text{ref}}(x))$) for each voxel in the dataset. Note that the transformation is the composition of all steps (pre-align, affine and non-rigid). Volumetric

Table 1

Registration quality metrics. Segmentations of the full brain and ventricles were used to assess registration accuracy. Dice similarity coefficient, median surface-to-surface distance, and the volume change error were calculated between the reference (formalin) and the transformed segmentations (100% ethanol, xylene, and paraffin).

	Dice Similarity Coefficient		Surface-to-surface distance [μm]		Volume change error	
	Affine	B-spline	Affine	B-spline	Affine	B-spline
Full brain						
100% ethanol	0.953	0.975	47.3	13.1	-3.2%	-1.9%
xylene	0.935	0.974	80.0	11.2	-9.7%	-1.2%
paraffin	0.890	0.951	142.7	46.4	-22.6%	-8.5%
Ventricles						
100% ethanol	0.503	0.677	20.7	9.3	-50.2%	-31.7%
xylene	0.507	0.655	26.2	9.3	-33.0%	-10.3%
paraffin	0.440	0.592	20.7	9.3	-50.4%	-33.5%

strain fields (volume change ratio minus 1, given as percentages in the Figs. 3 and 7) show the local compression or expansion from the reference (formalin) to the floating dataset. Fig. 3 shows renderings of the 100% ethanol, xylene, and paraffin datasets before and after non-rigid registration, slices through the volumetric strain fields, and histograms of the voxel-wise volumetric strains for the entire dataset of each preparation step.

Fig. 3 (left) illustrates the volumetric strain fields for the main steps, namely 100% ethanol, xylene, and paraffin. All embedding steps showed a similar pattern of volume change: greater volume change was observed towards the brain's outer surface, e.g. in the cerebral cortex, while less shrinkage was found in the region around the ventricles. Volume change appeared to be related to both distance from the embedding medium and anatomical region. For example, the thalamus could be identified from the volumetric strain fields by its smaller volume change. Similarly, white matter, granular, and molecular layers of the cerebellum could be seen from interfaces in the strain field maps. The histograms on the right side of Fig. 3 display the distribution of voxel-wise volumetric strain within the brain. Increasing shrinkage was seen over the course of embedding: for 50%, 70%, 80%, 90%, 100% ethanol, xylene, and paraffin, the median volumetric strain (inter-quartile range) from formalin to these steps was -5% (10%), -12% (16%), -23% (18%), -37% (13%), -39% (11%), -41% (12%), and -56% (10%).

3.3. Local X-ray absorption of corresponding features

Registration allows for side-by-side comparisons of the X-ray contrast in corresponding anatomical regions. Fig. 4 shows a sagittal slice (1) through the registered $3\times$ binned datasets in formalin (A), 100% ethanol (B), xylene (C), and paraffin (D). The cerebellum (2), hippocampus (3), and caudoputamen (4) are highlighted with zoom-ins. The difference in absorption coefficient μ between the brain and surrounding medium became larger with each subsequent step.

Fig. 5 shows magnified views of the aligned unbinned datasets with pixel size $3.1\ \mu\text{m}$. These zooms are within the regions of interest of the sagittal slices from Fig. 4 A1. For all datasets, spatial and density resolution were sufficient to identify individual cells. At this resolution, local density changes determined which features can be easily distinguished. The increased relative density of white matter in ethanol made identification of the extent of the granular layer difficult (B1). The same border was clearly distinguishable in xylene and paraffin (C1 & D1). The border between caudoputamen and the fiber tracks was clearest in 100% ethanol (B2) and nearly invisible in paraffin (D2).

Fig. 6 demonstrates the effect of ascending ethanol solutions on the fiber tract contrast. Regions of interest in coronal, axial, and sagittal virtual slices are shown in all steps of the $3\times$ binned datasets. A notable feature in the formalin-fixed brain is the white matter and other fiber tracts, which had μ below that of the surrounding brain tissue (see also e.g. Fig. 4A2). Contrast between fiber tracts and the surrounding tissue increased with ethanol concentration. The visibility of fibers was reduced in xylene and nearly zero when embedded in paraffin.

4. Discussion

The combination of slicing-free three-dimensional imaging and non-rigid registration allowed for the generation of volumetric strain fields and side-by-side comparison of tissue density in the selected preparation stages. As it can be applied after brain extraction and immediately prior to histological sectioning, X-ray virtual histology can also be incorporated into the creation of brain atlases. This procedure can be applied to other tissue types and preparation protocols to measure non-uniform volume changes and to select an optimized preparation with respect to X-ray contrast.

We analyzed brain shrinkage during the embedding protocol with two methods: manual segmentation of anatomical features (Rodgers,

2021a) and non-rigid registration (described in this Part 2). The approach based on non-rigid registration generates volumetric strain fields for the entire brain without the need for time-consuming manual segmentation. This offers a visual scheme that is more intuitive than tabulated volume measurements. For example, the maps shown in Fig. 3 allow for quick determination of the effect of tissue preparation on any anatomical region. Overlaying the anatomical information of the tomographic data with these strain fields (e.g. in Fig. 7 column 2) allows for studying volume changes within a given region in three dimensions.

A challenge of the non-rigid registration approach is that volumetric strain fields depend on the transformation model used for registration, with highly regularized models leading to smooth strain fields (Rodgers et al., 2021b). We tuned registration parameters for one dataset (xylene) and applied them to the other embedding states. The metrics in Table 1 and visual inspection of the registered datasets indicated that the registration parameters were not over-tuned. We expect that parameter tuning for each embedding state, e.g. with the L-curve method (Rodgers et al., 2021b), may provide better registration accuracy and more realistic strain fields, as the contrast changes affect the image similarity metric and thus influence the regularization weight. For population studies, we do not expect that tuning parameters for each mouse will be necessary as long as the identical experimental setup and imaging parameters are used. The current model was optimized for the $3\times$ binned volumes, i.e. for an isotropic voxel length of about $10\ \mu\text{m}$. Registration of the unbinned data would be more computationally demanding but allow for alignment of microstructures with smaller size and/or for the determination of more detailed volumetric strain fields. In this study, such a registration would have exceeded the available memory. A framework should be developed for `elastix` registration of sub-volumes with a large number of degrees of freedom without exceeding standard workstation resources.

Nevertheless, the calculated volumetric strain fields revealed that the shrinkage from the formalin-fixed state to each of the preparation steps was a function of both anatomical region and distance to the brain surface (Fig. 3). This distance dependence suggests shrinkage is related to diffusion of the embedding material into the brain tissue. Fig. 7 compares the volumetric strain field of the paraffin embedded brain with a three-dimensional distance transform of the segmentation of the full brain in paraffin. An overlay of the volumetric strain fields on the tomographic data reveals the dependence on anatomical region. The distance transform shows a first approximation of equal diffusion coefficient for all brain tissue. Deviation of the shrinkage maps from the distance transform is due to tissue composition-dependent uptake of embedding material, altered diffusion across anatomical borders, and decreased access of embedding media through smaller channels such as the ventricles.

Due to the role of diffusion, we expect geometry-dependent volumetric strain fields during preparation of smaller tissue sections such as biopsies (Katsamenis et al., 2019) and punches (Hieber et al., 2016; Töpperwien et al., 2018, 2019). The methodology presented here, or a more accessible variation based on laboratory X-ray microtomography, could be easily adapted to quantify and correct preparation-based tissue deformations.

In this experiment, the choice of embedding material did not alter the spatial resolution of the measurement setup. The data of the paraffin-embedded brain appears to have lower spatial resolution in Fig. 5 because it has been interpolated to be displayed as registered to formalin-fixed brain. Due to shrinkage, a higher spatial resolution may be desirable for studying samples embedded in paraffin compared to samples fixed in formalin. This is in contrast to the concept of expansion microscopy, where a sample is deliberately swollen to increase spatial resolution (Chen et al., 2015).

Individual cells were near the resolution limit of this study and therefore cellular shrinkage could not be accurately characterized. Töpperwien and co-workers performed sub-micrometer virtual histology of 1 mm diameter punches from the cerebellum of formalin-fixed,

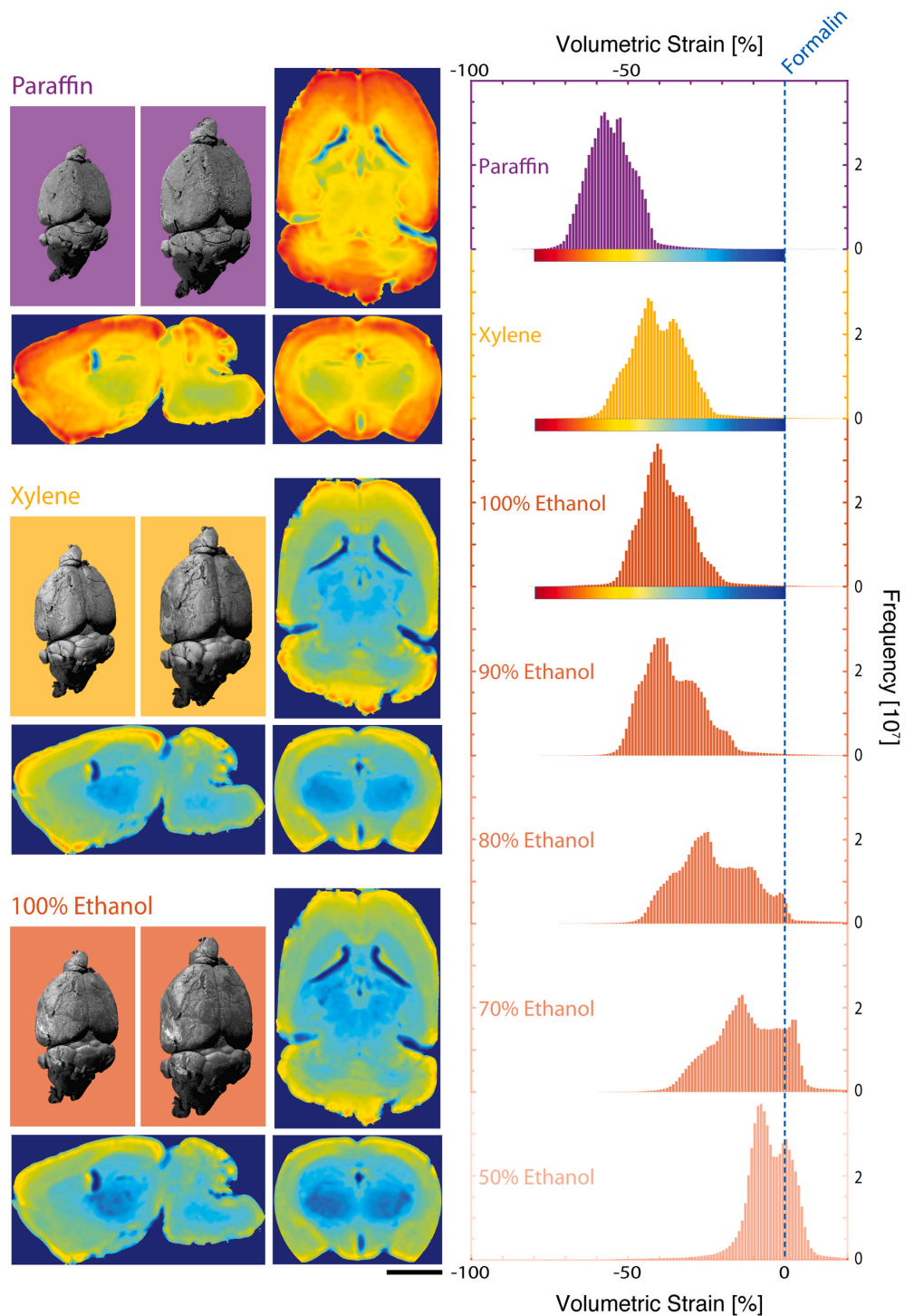


Fig. 3. Volumetric strain fields from mouse brain embedding. Non-rigid registration allows for extraction of the volume change of each voxel in the dataset. The left column shows a volume rendering of the brain before and after registration as well as the associated volumetric strain fields on selected sagittal, coronal, and axial slices (scale bar 3 mm). The highest volume shrinkage was observed towards the outer edges of the brain, e.g. in the cerebral cortex. The region around the ventricles showed the least shrinkage. Volumetric strain appeared to be related to both distance from the embedding medium and anatomical region. Histograms of the volumetric strain fields are given in the right column for all embedding steps. A voxel volume strain of zero corresponds to no volume change from formalin.

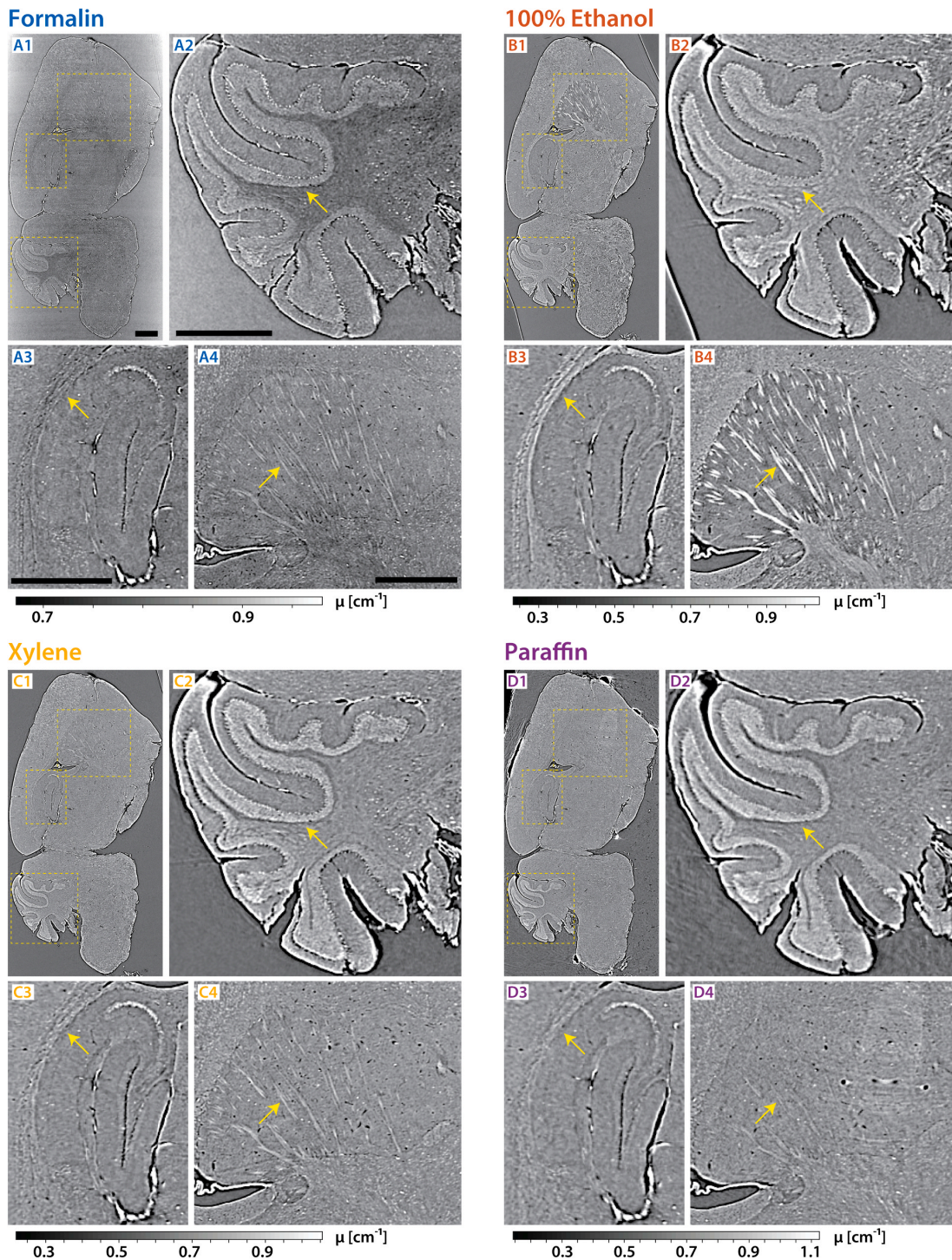


Fig. 4. Direct comparison of tissue density and contrast over the course of embedding: $3\times$ -binned datasets in formalin (A), 100% ethanol (B), xylene (C), and paraffin (D). Corresponding sagittal slices of the registered datasets (A1-D1) indicate regions of interest in the cerebellum (A2-D2), hippocampus (A3-D3), and caudoputamen (A4-D4). In the cerebellum (A2-D2), the relative densities of white matter and granular layer changed dramatically, see arrow. The hippocampus (A3-D3) showed similar contrast throughout embedding, though the nearby fiber tracts became more dense in 100% ethanol (arrow, B3). The fiber tracts in the caudoputamen (A4-D4) were clearly visible in ethanol (B4) and barely visible in paraffin (D4, arrow). All scale bars are 1 mm and the grayscale range is given by mean ± 2 standard deviations of the intensities in the full brain mask per embedding.

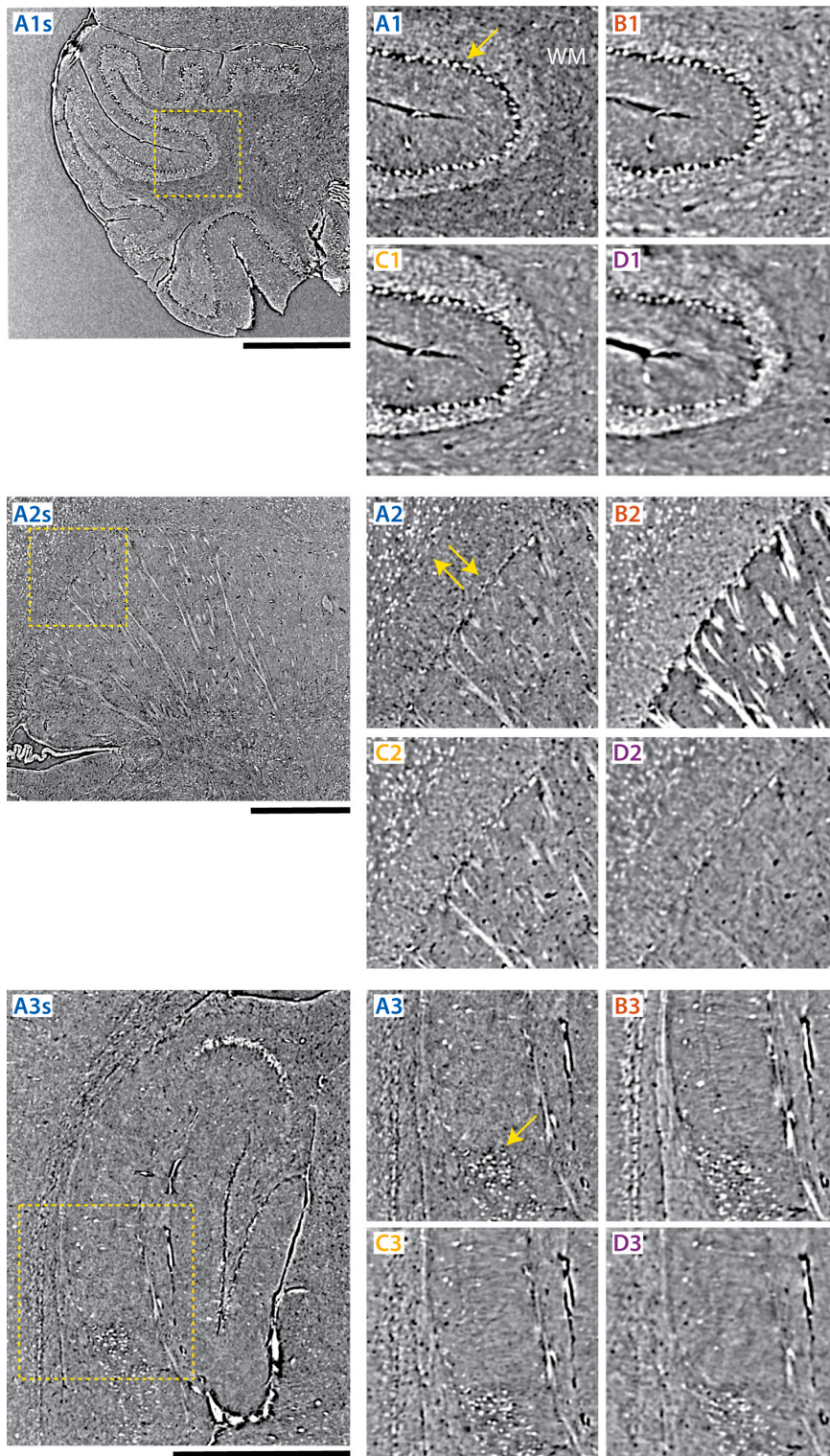
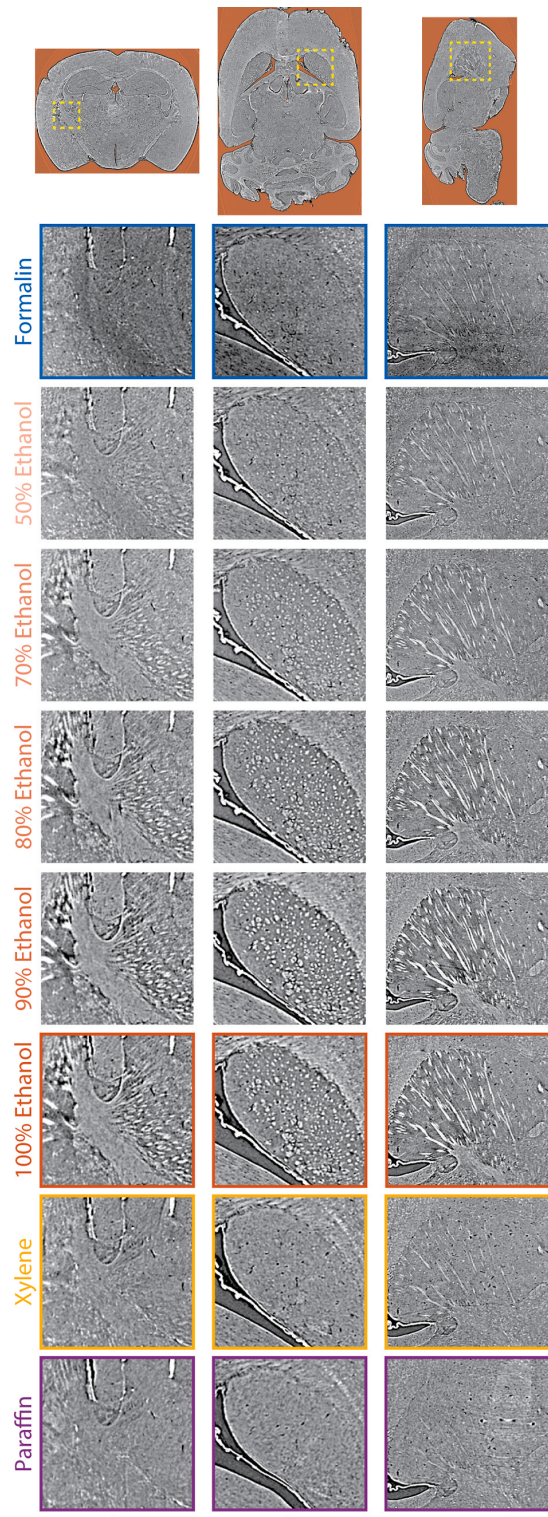


Fig. 5. Anatomical details in the aligned unbinned tomography data with a pixel length of $3.1\mu\text{m}$. Regions of interest of a selected sagittal slice in the formalin dataset showing the cerebellum (A1s), caudoputamen (A2s), and hippocampus (A3s). Zoom-ins provide cellular details in formalin (A), 100% ethanol (B), xylene (C), and paraffin (D). The density and texture of white matter (WM in A1) (A1-D1, right side) is greatly altered by embedding, while the Purkinje cell layer (arrow in A1) is clearly visible in all embeddings. The caudoputamen to fiber tract border (top arrow in A2) is especially visible in ethanol (B2), but individual cells in the somatomotor layers of the isocortex (bottom arrow in A2) are visible in all embeddings (A2-D2, upper left). Spatial resolution is approximately equal but appears poorer in paraffin (e.g. D3) because of the interpolation required to transform the data into the coordinates of formalin-fixed brain. All steps clearly capture cells of the subiculum in the retrohippocampal region (A3, arrow). All scale bars are 1 mm and the grayscale range is given by mean \pm 2.5 standard deviations of the intensities in the full brain mask per embedding.



(caption on next column)

Fig. 6. Enhancement of fiber tract contrast in ethanol solutions. Selected regions of interest showing fiber tracts within virtual sagittal, axial, and coronal slices are given across the entire embedding process after registration. Relative density of fiber tracts increased with respect to the surrounding tissue as ethanol concentration increased. The fiber tract contrast was almost entirely lost when embedded in paraffin. All scale bars are 1 mm and the grayscale range is given by mean \pm 1.5 standard deviations of the intensities in the full brain mask per embedding.

ethanol-immersed, and paraffin-embedded mouse brains (Töpperwien et al., 2019). Segmentation allowed for a statistical comparison of cell size, indicating that of Purkinje cells had shrinkage of 7% from formalin to ethanol and 7% from formalin to paraffin embedding, while cells in the granular layer had shrinkage of 30% from formalin to ethanol and 37% from formalin to paraffin embedding (Töpperwien et al., 2019). For reference, our results showed that for the full brain the mean volumetric strain from formalin to ethanol was 39% and to paraffin embedding was 56%. Thus, cell shrinkage is small compared to the shrinkage of larger anatomical regions, likely because tissue shrinkage is dominated by reduction of extracellular space during dehydration.

Preparation-induced changes in X-ray absorption coefficient of anatomical structures can enhance or invert contrast within the brain (see Figs. 4 to 6). We expect that the combination of datasets from selected embedding steps will provide complementary information and hence help to improve manual and automatic segmentation procedures (Stalder et al., 2014). Analysis of tissue density changes can inform the selection of a sample preparation protocol. We have emphasized the examples of ethanol solutions to highlight fiber tracts (Fig. 6) and paraffin embedding for visualizing the layers of the cerebellum (Fig. 5D1). Compared with formalin, fiber tracts in the caudoputamen showed 15-fold increase in contrast with surrounding tissue after immersion in 100% ethanol. This suggests that ethanol fixation should be used in studies of fiber orientation distribution, e.g. for validation of diffusion MRI (Trinkle et al., 2021; Foxley et al., 2021).

We postulate that the changes in volume and relative absorption coefficient of the fiber tracts can be explained by considering the distribution of water in the brain tissue. The space between the lipid bilayers that compose the myelin lamellae is filled with bound water, commonly referred to as myelin water, which can be observed with MRI systems and has significant clinical importance (Faizy et al., 2020; Birkl et al., 2021). Water in the surrounding tissue is mainly free water, which can be easily replaced by ethanol during immersion (Leist et al., 1986). The composition of myelin lipid bilayers of the central nervous system is about half cholesterol and one quarter phospholipids (Poitelon et al., 2020), the former is more soluble in xylene than ethanol and the latter more soluble in ethanol than xylene. Over the course of ascending ethanol solutions, free water is replaced by lower-absorbing ethanol, while bound water remains within myelin lipid multi-bilayer membranes and with higher relative absorption. This may also explain the increasing contrast between granular and molecular layers of the cerebellum, where the former is more cell-rich and thus contains more bound than free water. During the transition from ethanol to xylene, a greater amount of myelin lipids are dissolved, likely resulting in a breakdown of the membranes and release of the myelin water, reducing the absorption coefficient of fiber tracts relative to the surroundings. Additionally, electrostatic forces on myelin in ethanol and dissolving of lipids in xylene may lead to size changes of fibers, which could help to further explain the observed fiber tract shrinkage and X-ray absorption changes. Small angle X-ray scattering experiments could provide insight into related changes of myelin nanostructure (Georgiadis et al., 2020, 2021; Schulz et al., 2020).

5. Conclusions

We non-rigidly registered hard X-ray microtomography datasets of the same mouse brain from the formalin-fixed to paraffin-embedded

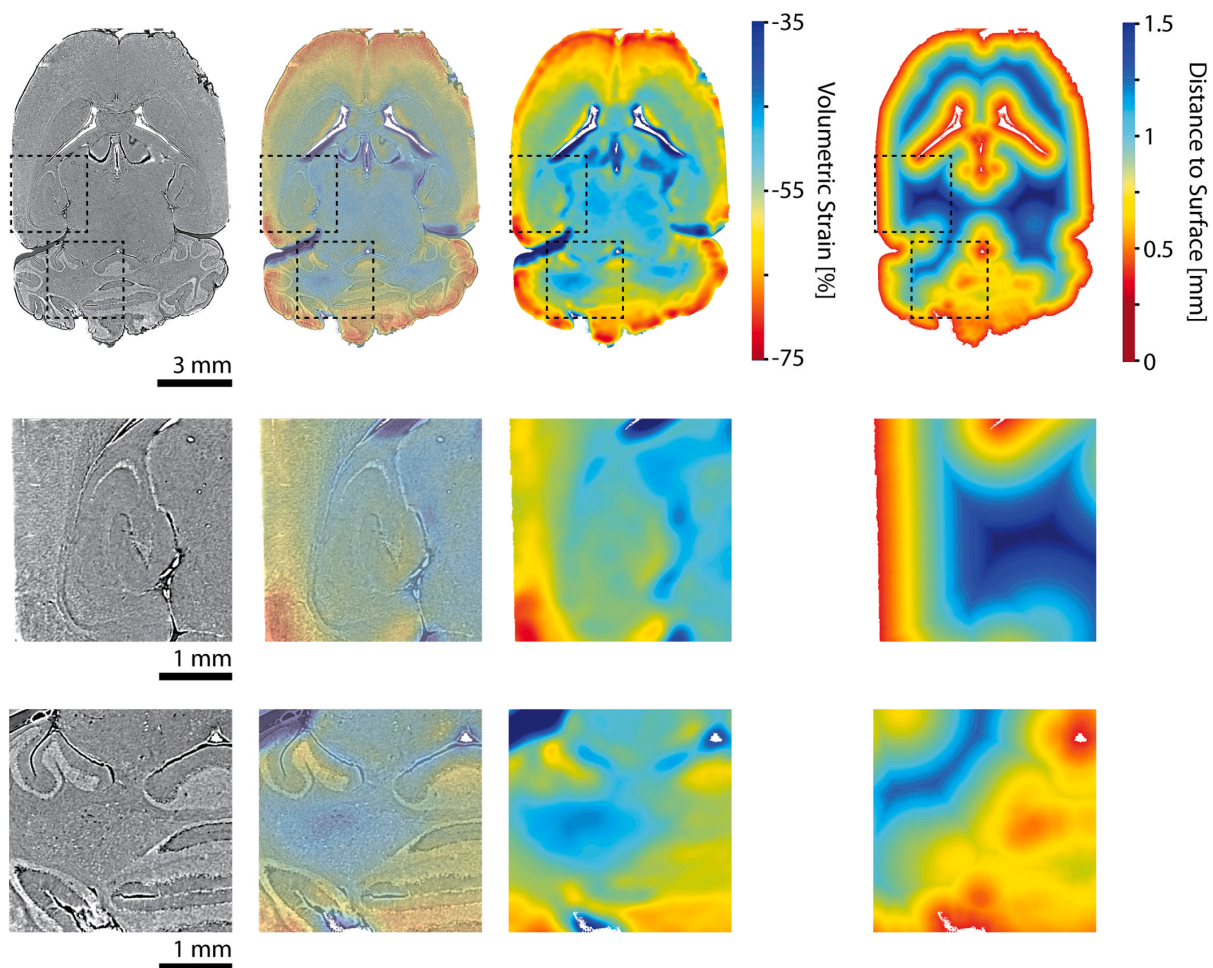


Fig. 7. Comparison of an axial slice through the paraffin embedded brain (column 1), the volumetric strain field (column 3), and the distance transform (column 4). Column 2 shows an overlay of the volumetric strain field on the tomography data. The three-dimensional distance transform was calculated from the segmentation of the paraffin embedded full brain. The grayscale range for column 1 is given by mean \pm 1.5 standard deviations of the intensities in the full brain mask.

state. Volumetric strain fields revealed local shrinkage that depended on the anatomical region and the distance to the external surface. Surprisingly, the preparation step can be selected to highlight specific anatomical features, e.g. fiber tract contrast is amplified by a factor of 15 in 100% ethanol with respect to the formalin-fixed state. The selection of optimized tissue preparation and quantification of morphology changes allows virtual histology to complement mouse brain atlases based on magnetic resonance imaging and serial histology.

CRediT author contribution statement

Griffin Rodgers: Conceptualization, Methodology, Software, Formal analysis, Investigation, Data curation, Writing – original draft, Writing – review & editing, Visualization, Funding acquisition. **Christine Tanner:** Software, Formal analysis, Investigation, Writing – review & editing, Visualization, Supervision. **Georg Schulz:** Conceptualization, Methodology, Investigation, Writing – review & editing, Supervision. **Alexandra Migga:** Validation, Formal analysis, Writing – review & editing, Visualization. **Willy Kuo:** Resources, Writing – review & editing. **Christos Bikis:** Methodology, Formal analysis, Writing – review & editing. **Mario Scheel:** Resources, Writing – review & editing. **Vartan Kurtcuoglu:** Writing – review & editing, Supervision, Project

administration, Funding acquisition. **Timm Weitkamp:** Resources, Writing – review & editing, Funding acquisition. **Bert Müller:** Conceptualization, Methodology, Investigation, Resources, Writing – review & editing, Visualization, Supervision, Project administration, Funding acquisition.

Declaration of Competing Interest

None.

Data availability

The tomographic data from all preparation steps as well as the registration parameters and final transformations are publicly available in a Zenodo repository (<https://doi.org/10.5281/zenodo.4651412>) (Rodgers et al., 2021c). Data registration and transformations can be performed with the provided parameter files and the open source software *elastix/transformix* (<https://elastix.lumc.nl/>) (Klein et al., 2010; Shamonin et al., 2014). The 3 \times downsampled volumes can be immediately downloaded. Due to the large data sizes, the full resolution data will be made available by request to the first author.

Acknowledgment

This work was carried out under Synchrotron SOLEIL experiment No. 20190424. The authors thank J. Perrin and D. Guillaume of the ANATOMIX beamline at Synchrotron SOLEIL for support during the beam time. ANATOMIX is an Equipment of Excellence (EQUIPEX) funded by the Investments for the Future program of the French National Research Agency (ANR), project NanoimagesX, grant no. ANR-11-EQPX-0031. W.K. and V.K. acknowledge support from the Swiss National Science Foundation via NCCR Kidney.CH and Project No. 153523. G.R., C. T., and B.M. acknowledge support from the Swiss National Science Foundation Project No. 185058.

References

- Albers, J., Pacilé, S., Markus, M., Wiart, M., Vande Velde, G., Tromba, G., Dullin, C., 2018. X-ray-based 3D virtual histology-adding the next dimension to histological analysis. *Mol. Imaging Biol.* 20 (5), 732–741. <https://doi.org/10.1007/s11307-018-1246-3>.
- Birkel, C., Doucette, J., Fan, M., Hernández-Torres, E., Rauscher, A., 2021. Myelin water imaging depends on white matter fiber orientation in the human brain. *Magn. Reson. Med.* 85 (4), 2221–2231. <https://doi.org/10.1002/mrm.28543>.
- C. Culling, Chapter 2: Methods of examination of tissues and cells, in: C. Culling (Ed.), *Handbook of Histopathological and Histochemical Techniques*, 3rd ed., Butterworth-Heinemann, 1974, 19–25. [10.1016/B978-0-407-72901-8.50009-3](https://doi.org/10.1016/B978-0-407-72901-8.50009-3).
- Chen, F., Tillberg, P.W., Boyden, E.S., 2015. Expansion microscopy. *Science* 347 (6221), 543–548. <https://doi.org/10.1126/science.1260088>.
- Crum, W., Griffin, L., Hill, D., Hawkes, D., 2003. Zen and the art of medical image registration: correspondence, homology, and quality. *NeuroImage* 20 (3), 1425–1437. <https://doi.org/10.1016/j.neuroimage.2003.07.014>.
- Dice, L.R., 1945. Measures of the amount of ecologic association between species. *Ecology* 26 (3), 297–302. <https://doi.org/10.2307/1932409>.
- Dyer, E.L., Gray Roncal, V., Prasad, J.A., Fernandes, H.L., Gürsoy, D., De Andrade, V., Fezzaa, K., Xiao, X., Vogelstein, J.T., Jacobsen, C., Kording, K.P., Kasthuri, N., 2017. Quantifying mesoscale neuroanatomy using X-ray microtomography. *eNeuro* 4. <https://doi.org/10.1523/ENEURO.0195-17.2017>.
- Faizy, T.D., Thaler, C., Broocks, G., Flottmann, F., Leischner, H., Knip, H., Nawabi, J., Schön, G., Stellmann, J.-P., Kemmling, A., Reddy, R., Heit, J.J., Fiehler, J., Kumar, D., Hanning, U., 2020. The myelin water fraction serves as a marker for age-related myelin alterations in the cerebral white matter – a multiparametric MRI aging study. *Front. Neurosci.* 14, 136. <https://doi.org/10.3389/fnins.2020.00136>.
- Foxley, S., Sampathkumar, V., De Andrade, V., Trinkle, S., Sorokina, A., Norwood, K., La Riviere, P., Kasthuri, N., 2021. Multi-modal imaging of a single mouse brain over five orders of magnitude of resolution. *NeuroImage* 238, 118250. <https://doi.org/10.1016/j.neuroimage.2021.118250>.
- Georgiadis, M., Schroeter, A., Gao, Z., Guizar-Sicairos, M., Novikov, D.S., Fieremans, E., Rudin, M., 2020. Retrieving neuronal orientations using 3D scanning SAXS and comparison with diffusion MRI. *NeuroImage* 204, 116214. <https://doi.org/10.1016/j.neuroimage.2019.116214>.
- Georgiadis, M., Schroeter, A., Gao, Z., Guizar-Sicairos, M., Liebi, M., Leuze, C., McNab, J. A., Balolia, A., Veraart, J., Ades-Aron, B., Kim, S., Shepherd, T., Lee, C.H., Walczak, P., Chodankar, S., DiGiacomo, P., David, G., Augath, M., Zerbi, V., Sommer, S., Rajkovic, I., Weiss, T., Bunk, O., Yang, L., Zhang, J., Novikov, D.S., Zeineh, M., Fieremans, E., Rudin, M., 2021. Nanostructure-specific X-ray tomography reveals myelin levels, integrity and axon orientations in mouse and human nervous tissue. *Nat. Commun.* 12 (1), 2941. <https://doi.org/10.1038/s41467-021-22719-7>.
- Hansen, P.C., 2000. The L-curve and its use in the numerical treatment of inverse problems. In: Johnston, P. (Ed.), *Computational Inverse Problems in Electrocardiology*. WIT Press, pp. 119–142 (*Advances in Computational Bioengineering*).
- Hardy, W.B., 1899. On the structure of cell protoplasm. *J. Physiol.* 24 (2), 158–210. <https://doi.org/10.1113/jphysiol.1899.sp000755>.
- Hieber, S.E., Bikis, C., Khimchenko, A., Schweighauser, G., Hench, J., Chicherova, N., Schulz, G., Müller, B., 2016. Tomographic brain imaging with nucleolar detail and automatic cell counting. *Sci. Rep.* 6, 32156. <https://doi.org/10.1038/srep32156>.
- Katsamenis, O.L., Olding, M., Warner, J.A., Chatelet, D.S., Jones, M.G., Sgalla, G., Smit, B., Larkin, O.J., Haig, I., Richeldi, L., Sinclair, I., Lackie, P.M., Schneider, P., 2019. X-ray micro-computed tomography for nondestructive three-dimensional (3D) X-ray histology. *Am. J. Pathol.* 189 (8), 1608–1620. <https://doi.org/10.1016/j.ajpath.2019.05.004>.
- Khimchenko, A., Deyhle, H., Schulz, G., Schweighauser, G., Hench, J., Chicherova, N., Bikis, C., Hieber, S.E., Müller, B., 2016. Extending two-dimensional histology into the third dimension through conventional micro computed tomography. *NeuroImage* 139, 26–36. <https://doi.org/10.1016/j.neuroimage.2016.06.005>.
- Khimchenko, A., Bikis, C., Pacureanu, A., Hieber, S.E., Thalman, P., Deyhle, H., Schweighauser, G., Hench, J., Frank, S., Müller-Gerbl, M., Schulz, G., Cloetens, P., Müller, B., 2018. Hard X-ray nanoholotomography: large-scale, label-free, 3D neuroimaging beyond optical limit. *Adv. Sci.* 5 (6), 1700694. <https://doi.org/10.1002/advs.201700694>.
- Klein, S., Staring, M., Murphy, K., Viergever, M.A., Pluim, J.P.W., 2010. elastix: a toolbox for intensity-based medical image registration. *IEEE Trans. Med. Imag.* 29, 196–205. <https://doi.org/10.1109/TMI.2009.2035616>.
- Kuan, A.T., Phelps, J.S., Thomas, L.A., Nguyen, T.M., Han, J., Chen, C.-L., Azevedo, A.W., Tuthill, J.C., Funke, J., Cloetens, P., Pacureanu, A., Lee, W.-C.A., 2020. Dense neuronal reconstruction through X-ray holographic nano-tomography. *Nat. Neurosci.* 23 (12), 1637–1643. <https://doi.org/10.1038/s41593-020-0704-9>.
- Leist, D.P., Nettleton, G.S., Feldhoff, R.C., 1986. Determination of lipid loss during aqueous and phase partition fixation using formalin and glutaraldehyde. *J. Histochem. Cytochem.* 34 (4), 437–441. <https://doi.org/10.1177/34.4.3081623>.
- Ma, Y., Smith, D., Hof, P., Foerster, B., Hamilton, S., Blackband, S., Yu, M., Benveniste, H., 2008. In vivo 3D digital atlas database of the adult C57BL/6J mouse brain by magnetic resonance microscopy. *Front. Neuroanat.* 2, 1. <https://doi.org/10.3389/neuro.05.001.2008>.
- Müller, B., Lang, S., Dominietto, M., Rudin, M., Schulz, G., Deyhle, H., Germann, M., Pfeiffer, F., David, C., Weitkamp, T., 2008. High-resolution tomographic imaging of microvessels. *SPIE*, pp. 89–98.
- Pluim, J.P., Muenzing, S.E., Eppenhof, K.A., Murphy, K., 2016. The truth is hard to make: validation of medical image registration. 2016 23rd International Conference on Pattern Recognition (ICPR). IEEE, pp. 2294–2300. <https://doi.org/10.1109/ICPR.2016.7899978>.
- Poitelou, Y., Kopec, A.M., Belin, S., 2020. Myelin fat facts: an overview of lipids and fatty acid metabolism. *Cells* 9 (4). <https://doi.org/10.3390/cells9040812>.
- Quester, R., Schröder, R., 1997. The shrinkage of the human brain stem during formalin fixation and embedding in paraffin. *J. Neurosci. Methods* 75 (1), 81–89. [https://doi.org/10.1016/S0165-0270\(97\)00050-2](https://doi.org/10.1016/S0165-0270(97)00050-2).
- Rodgers, G., Kuo, W., Schulz, G., Scheel, M., Migga, A., Bikis, C., Tanner, C., Kurtcuoglu, V., Weitkamp, T., Müller, B., 2021a. Virtual histology of an entire mouse brain from formalin fixation to paraffin embedding. Part 1: data acquisition, anatomical feature segmentation, global volume and density tracking. *J. Neurosci. Methods* 364, 109354 (submitted for publication).
- Rodgers, G., Schulz, G., Kuo, W., Scheel, M., Kurtcuoglu, V., Weitkamp, T., Müller, B., Tanner, C., 2021b. Non-rigid registration to determine strain fields during mouse brain fixation and embedding. *Proc. SPIE*, pp. 55–65. <https://doi.org/10.1117/12.2583632>.
- Rodgers, G., Schulz, G., Kuo, W., Tanner, C., Müller, B., Microtomography of a mouse brain from formalin fixed to paraffin embedded: datasets and registration parameters, 2021c. <https://zenodo.org/record/4651412>.
- Schnabel, J.A., Tanner, C., Castellano-Smith, A.D., Degenhard, A., Leach, M.O., Hose, D. R., Hill, D.L., Hawkes, D.J., 2003. Validation of nonrigid image registration using finite-element methods: application to breast MRI images. *IEEE Trans. Med. Imag.* 22 (2), 238–247. <https://doi.org/10.1109/TMI.2002.808367>.
- Schulz, G., Crooijmans, H.J.A., Germann, M., Scheffler, K., Müller-Gerbl, M., Müller, B., 2011. Three-dimensional strain fields in human brain resulting from formalin fixation. *J. Neurosci. Methods* 202 (1), 17–27. <https://doi.org/10.1016/j.jneumeth.2011.08.031>.
- Schulz, G., Deyhle, H., Bikis, C., Bunk, O., Müller, B., 2020. Imaging the orientation of myelin sheaths in a non-stained histology slide of human brain. *Prec. Nanomed.* 3 (4), 656–665. <https://doi.org/10.33218/001c.17211>.
- Shamonin, D., Bron, E., Lieveveldt, B., Smits, M., Klein, S., Staring, M., 2014. Fast parallel image registration on CPU and GPU for diagnostic classification of Alzheimer's disease. *Front. Neuroinform.* 7, 50. <https://doi.org/10.3389/fninf.2013.00050>.
- Stalder, A.K., Ilgenstein, B., Chicherova, N., Deyhle, H., Beckmann, F., Müller, B., Hieber, S.E., 2014. Combined use of micro computed tomography and histology to evaluate the regenerative capacity of bone grafting materials. *Int. J. Mater. Res.* 105 (7), 679–691. <https://doi.org/10.3139/146.111050>.
- Strotton, M.C., Bodey, A.J., Wanelik, K., Darrow, M.C., Medina, E., Hobbs, C., Rau, C., Bradbury, E., 2018. Optimising complementary soft tissue synchrotron X-ray microtomography for reversibly-stained central nervous system samples. *Sci. Rep.* 8, 12017. <https://doi.org/10.1038/s41598-018-30520-8>.
- Töppervien, M., van der Meer, F., Stadelmann, C., Salditt, T., 2018. Three-dimensional virtual histology of human cerebellum by X-ray phase-contrast tomography. *Proc. Natl. Acad. Sci. U. S. A.* 115 (27), 6940–6945. <https://doi.org/10.1073/pnas.1801678115>.
- Töppervien, M., Markus, A., Alves, F., Salditt, T., 2019. Contrast enhancement for visualizing neuronal cytoarchitecture by propagation-based X-ray phase-contrast tomography. *NeuroImage* 199, 70–80. <https://doi.org/10.1016/j.neuroimage.2019.05.043>.
- Töppervien, M., van der Meer, F., Stadelmann, C., Salditt, T., 2020. Correlative X-ray phase-contrast tomography and histology of human brain tissue affected by Alzheimer's disease. *NeuroImage* 210, 116523. <https://doi.org/10.1016/j.neuroimage.2020.116523>.
- Trinkle, S., Foxley, S., Kasthuri, N., Rivière, P.L., 2021. Synchrotron X-ray micro-CT as a validation dataset for diffusion MRI in whole mouse brain. *Magn. Reson. Med.* 86 (2), 1067–1076. <https://doi.org/10.1002/mrm.28776>.
- Wehrli, H., Bezrukov, I., Wiehr, S., Lehnhoff, M., Fuchs, K., Mannheim, J., Quintanilla-Martinez, L., Kohlhöfer, U., Kneilling, M., Pichler, B., Sauter, A., 2015. Assessment of murine brain tissue shrinkage caused by different histological fixatives using magnetic resonance and computed tomography imaging. *Histol. Histopathol.* 30, 601–613. <https://doi.org/10.14670/HH-30.601>.
- Yushkevich, P.A., Piven, J., Hazlett, H.C., Smith, R.G., Ho, S., Gee, J.C., Gerig, G., 2006. User-guided 3D active contour segmentation of anatomical structures: significantly improved efficiency and reliability. *NeuroImage* 31, 1116–1128. <https://doi.org/10.1016/j.neuroimage.2006.01.015>.

4 X-ray virtual histology for the investigation of temporal lobe epilepsy in a mouse model

Manuscript in preparation

X-ray virtual histology for the investigation of temporal lobe epilepsy in a mouse model

G. Rodgers^{a,b}, C. Bikis^{a,b,c}, P. Janz^{d,e}, C. Tanner^{a,b}, G. Schulz^{a,b,f}, M. Osterwalder^{a,b}, P. Thalmann^{a,b}, C. Haas^{d,g,h}, B. Müller^{a,b}

^aBiomaterials Science Center, Department of Biomedical Engineering, University of Basel, 4123 Allschwil, Switzerland

^bBiomaterials Science Center, Department of Clinical Research, University Hospital Basel, 4031 Basel, Switzerland

^cIntegrierte Psychiatrie Winterthur – Zürcher Unterland, 8408 Winterthur, Switzerland

^dExperimental Epilepsy Research, Department of Neurosurgery, Medical Center – University of Freiburg, 79114 Freiburg, Germany

^eFaculty of Biology, University of Freiburg, 79114 Freiburg, Germany

^fCore Facility Micro- and Nanotomography, Department of Biomedical Engineering, University of Basel, 4123 Allschwil, Switzerland

^gBrainLinks-BrainTools Cluster of Excellence, University of Freiburg, 79114 Freiburg, Germany

^hBernstein Center Freiburg, University of Freiburg, 79114 Freiburg, Germany

4.1 Abstract

The most common form of epilepsy among adults is mesial temporal lobe epilepsy (mTLE), with seizures originating in the hippocampus due to abnormal electrical activity. The gold standard for *post mortem* pathological analysis of mTLE is histology. Correlation with *in vivo* magnetic resonance imaging for the identification of biomarkers is an ongoing challenge. Unfortunately, conventional histology does not provide a three-dimensional visualization of the pathology with cellular resolution. To fill this gap, we propose complementary X-ray virtual histology. Here, synchrotron radiation-based phase contrast micro computed tomography with 1.6 μm -wide voxels was used for *post mortem* visualization of kainate injection induced mTLE in a mouse model. We demonstrate that virtual histology of unstained, unsectioned paraffin-embedded brain hemispheres can identify hippocampal sclerosis through loss of pyramidal neurons in the first and third regions of the *Cornu ammonis* as well as granule cell dispersion within the dentate gyrus. Segmentation of the virtual histology data allowed for three-dimensional quantification of morphology and density changes during epileptogenesis. Compared to control mice, the total dentate gyrus volume doubled and granular layer volume nearly quadrupled in mice sacrificed 21 days after kainate injection. Subsequent sectioning of the same mouse brains allowed for benchmarking of virtual histology with well-established histochemical and immunofluorescence stains. Thus, virtual histology is a complementary *post mortem* neuroimaging tool to unlock the third dimension for cellular-resolution pathological analysis of mTLE.

4.2 Introduction

Epilepsy is among the most common neurological disorders with a prevalence of about 1% worldwide. The most frequent form of human epilepsy is mesial temporal lobe epilepsy (mTLE) [81], with seizures often originating in the hippocampus as a result of abnormal electrical activity [82]. mTLE is caused by brain injury, which can lead to aberrant wiring of neuronal circuits, though it is still unclear in which cases brain injury produces mTLE and when it will develop [81, 83]. mTLE is commonly associated with hippocampal sclerosis, characterized by glial scarring, the loss of pyramidal neurons in the first and third regions of the *Cornu ammonis* (CA1 and CA3), and granule cell dispersion (GCD) within the dentate gyrus (DG) [84, 85]. Unfortunately, mTLE can be resistant to pharmacological treatment, requiring surgery to remove epileptic lesions [81] that does not prevent seizures in all cases [86].

Neuroimaging plays an important role in diagnosis and understanding of epilepsy. For example, determining epilepsy biomarkers for *in vivo* magnetic resonance imaging (MRI) is an active area of research [87], where validation with *post mortem* cellular-resolution imaging is critical [88]. Conventional histology with well-established immunohistochemistry is the gold standard for histopathological investigation of mTLE. Histology, however, has limited out-of-plane resolution and suffers from artefacts during staining and sectioning. As a result, correlation with MRI can involve complex slice-to-volume registration [89]. Visualizing the three-dimensional arrangement of hippocampal cells is critical for understanding the progression of mTLE, see e.g. Refs. 90–92, however MRI is not ideal for this task due to its relatively low spatial resolution. Therefore, a label- and slicing-free volumetric imaging approach is highly desirable, where compatibility with both MRI and conventional histology workflows would allow for correlation and validation.

Hard X-ray micro- and nanotomography are attractive for this role, as X-ray imaging can bypass sectioning or clearing and provide spatial resolution below the limits of optical microscopy [73, 74]. While X-ray absorption of soft tissues is weak, highly brilliant X-ray sources and phase contrast imaging can reach the requisite spatial and density resolution for visualization of unstained brain tissue with micrometer [66–68] or even nanometer resolution [74]. X-ray microtomography at an intermediary step of the standard histopathological preparation has allowed for extension of conventional histology to the third dimension [71] and provides enhanced X-ray contrast [72, 93, 94]. This emerging field is often referred to as *X-ray virtual histology*.

This work evaluates virtual histology with synchrotron radiation-based X-ray microtomography to track the histopathological progression of mTLE in a mouse model. The kainate (KA) model of mTLE is used, where stereotactic KA injection into the hippocampus induces a pathogenesis resembling that in humans [95]. Label-free X-ray virtual histology with 1.6 μm -wide voxels visualized paraffin-embedded brain hemispheres from mice sacrificed 1, 7, 14, and 21 days after KA injection. Virtual histology could identify the onset of hippocampal sclerosis, namely GCD and pyramidal neuron loss. The volumetric virtual histology data were benchmarked with corresponding sections in conventional histology. Finally, segmentation of the molecular, granular, and polymorph layers of the DG enabled three-dimensional quantification of electron density and morphology changes during epileptogenesis.

4.3 Materials and methods

4.3.1 Animals and kainate injection

Fifteen 9-12 weeks-old male C57BL/6N wildtype mice (Charles River, Sulzfeld, Germany) were used for this experiment. The mice were housed at room temperature in a 12 hour light/dark cycle and were provided with food and water *ad libitum*. The animal procedures were in accordance with the guidelines of the European Community's Council Directive of 22 September 2010 (2010/63/EU) and were approved by the regional council (Regierungspräsidium Freiburg).

The fifteen mice formed five groups of three replicates. On day 0, Group 1 were injected with saline and Groups 2-5 were injected with kainate. On day 1, Group 2 were sacrificed. On day 7, Groups 1 and 3 were sacrificed. On day 14, Group 4 were sacrificed. On day 21, Group 5 were sacrificed. The injection procedure is described in references 92,96,97. In short, anaesthetized mice were stereotactically injected with 50 nL of either 0.9% saline solution (Group 1) or 20 mM kainate solution (Tocris, Bristol, UK) in 0.9% saline (Groups 2-4) into the right dorsal hippocampus. One of the mice from Group 3 died before reaching the sacrifice time point.

4.3.2 Tissue preparation

The mice were anaesthetized and transcardially perfused with 0.9% saline followed by 4% paraformaldehyde in 0.1 M phosphate buffer for 5 minutes, then sacrificed. Brains were extracted and post-fixed in 4% paraformaldehyde with 0.1 M phosphate buffer overnight at 4 °C. After fixation, a scalpel was used to separate the brain hemispheres and remove the cerebellum and olfactory bulbs. Brain hemispheres were embedded in paraffin following the standard procedure in histopathology [13]: the tissue was dehydrated in ascending ethanol solutions, cleared in xylene, and embedded in liquid paraffin wax (Surgipath Paraplast®, Leica Biosystems, Wetzlar, Germany) before cooling to form a solid block. The paraffin-embedded samples were imaged with a nanotom m® (GE Sensing and Inspection Technologies GmbH, Hürth, Germany) laboratory microtomography system to identify defects such as cracks, highly absorbing debris, or trapped air. Samples with defects were melted and re-embedded in paraffin. A tissue punch with inner diameter of 6 mm was used to extract cylindrical samples containing an entire brain hemisphere and minimal excess paraffin.

4.3.3 Synchrotron radiation-based microtomography

X-ray microtomography of the mouse brain hemispheres was performed at the ID19 Beamline of the European Synchrotron Radiation Facility (Grenoble, France). Here, a “pink beam” [98] with mean photon energy of 19 keV was used. A detector based on a 100 µm-thick Ce:LuAG scintillator coupled *via* a 4× magnifying objective to a scientific CMOS camera (pco.edge 5.5, 2560 × 2160 pixel array, 6.5 µm physical pixel size) was used to achieve an effective pixel size of 1.625 µm. The resulting detector field-of-view was 4.16 mm × 3.51 mm. A propagation distance of 280 mm was selected to allow for propagation-based phase contrast. Each brain was scanned with 4000 projections around 360° with an exposure time of 100 ms per projection. Three or four height steps were acquired to cover the entire brain hemispheres.

Prior to reconstruction, projections were phase retrieved using Paganin’s filter [64] with $\delta/\beta = 1500$. Ring artefacts were reduced using the method described in [99]. Tomographic reconstruction was performed in **MATLAB** (release 2016a, The MathWorks, Inc., Natick, USA) using a filtered backprojection algorithm with the standard Ram-Lak filter [32]. Overlap between height steps was determined using the open source registration toolbox **elastix** (version 4.9) [100, 101]. A translation transform was used with normalized correlation coefficient as a similarity metric. Height steps were combined with linear blending within the overlapping regions.

4.3.4 Immunohistochemistry and histology

Subsequent to tomographic imaging, 50 μm thick coronal sections of the paraffin-embedded brain hemispheres were produced on a vibratome (VT1000S, Leica, Bensheim, Germany). Sections were alternately stained with Hematoxylin and eosin (H&E), Nissl, NeuN-Iba1, and GFAP. For immunofluorescence staining, sections were treated with 0.25% TritonX-100 in 1% bovine serum albumin for 1 hour, then incubated 4°C for 24 hours with Guinea pig anti-NeuN (1:500, Synaptic Systems, Göttingen, Germany), rabbit anti-Iba-1 (1:1000, Wako Chemicals, Neuss, Germany), or rabbit anti-GFAP (1:500, Dako, Hamburg, Germany). For detection, Cy2-, Cy3- or Cy5-conjugated secondary donkey anti-guinea pig or goat anti-rabbit antibodies (1:200, Jackson ImmunoResearch Laboratories Inc., West Grove, USA) were applied for 3 hours at room temperature followed by rinsing in 0.1 M PB for 6×15 minutes. Sections were then counterstained with DAPI (4',6-diamidino-2-phenylindole; 1:10000, Roche Diagnostics GmbH, Mannheim, Germany). The free-floating sections were mounted on glass slides and cover-slipped with ProLong Gold (Molecular Probes, Invitrogen, Carlsbad, USA).

Histological slides were scanned using an AxioImager2 microscope (Zeiss, Göttingen, Germany). A 10 \times objective (Plan-APOCHROMAT, Zeiss, Göttingen, Germany) and digital camera (MR605, Zeiss, Göttingen, Germany) were used to acquire composites immunofluorescent-stained sections. The composites were processed with the Zen (Zeiss, Göttingen, Germany) software package.

Several histology slices suffered from artefacts including thickness variations, folds, tears, and cracks. The most artefact-free sections were selected for comparison with virtual histology.

4.3.5 Segmentation and rendering of the volumetric data

The tomography data were manually registered with a rigid transform to the reference coordinate system of the Allen Mouse Brain Atlas [102] using the open-source tools **ITK-SNAP** (version 3.8.0) [103] and **transformix** (version 4.9) [100, 101].

The molecular, granular, and polymorph layers of the DG were semi-automatically segmented from the tomography data. Manual segmentations were guided by the Allen Mouse Brain Atlas [102]. Segmentation was performed in **Amira 6.2.0** (Thermo Fisher Scientific Inc., Waltham, USA). The $4 \times 4 \times 4$ binned tomography data were used. The blow tool (tolerance 15, gauss width 3) was used to manually segment every 10th virtual coronal slice. Three-dimensional segmentations were created using the wrap tool on the stack of two-dimensional segmentations. Volume renderings were made in **VGStudio MAX 2.1** (Volume Graphics, Heidelberg, Germany) and

Amira 6.2.0 (Thermo Fisher Scientific Inc., Waltham, USA) for Figures 4.1 and 4.6, respectively.

4.4 Results

4.4.1 Visualizing pathological changes associated with epilepsy

The volumetric datasets from X-ray virtual histology allowed for navigation of the mouse brain’s microanatomy in three dimensions. Virtual sectioning identified the site of saline or KA injection as well as the relevant features of the hippocampal formation, namely the *Cornu ammonis* and DG, see Figure 4.1. For a detailed comparison of the healthy and epileptic brains, all measured hemispheres were coarsely aligned with the coordinate system of the Allen Mouse Brain Reference Atlas [102].

Virtual coronal slices through the KA-injected brains revealed pathological changes associated with the progression of mTLE, see Figure 4.2. Despite the label-free approach, hippocampal sclerosis was observed by GCD as well as a loss of neurons in the pyramidal layers of the CA1 and CA3 regions. The extent of hippocampal sclerosis increased with time from injection to sacrifice. In contralateral hemispheres, the pyramidal layers of the CA1 and CA3 regions were identifiable by a continuous cell layer of increased density. The loss of pyramidal neurons in these regions was characterized by an initial increase in density of individual cells (see 1 day post injection), followed by a widening of pyramidal layer and a decrease in density and a loss of the layers’ contrast relative to the surrounding strata. Pyramidal neuron loss in the CA1 field was identified 7 days after KA injection, while neuron loss in the CA3 field was first observed 14 days after KA injection. The GCL appeared as

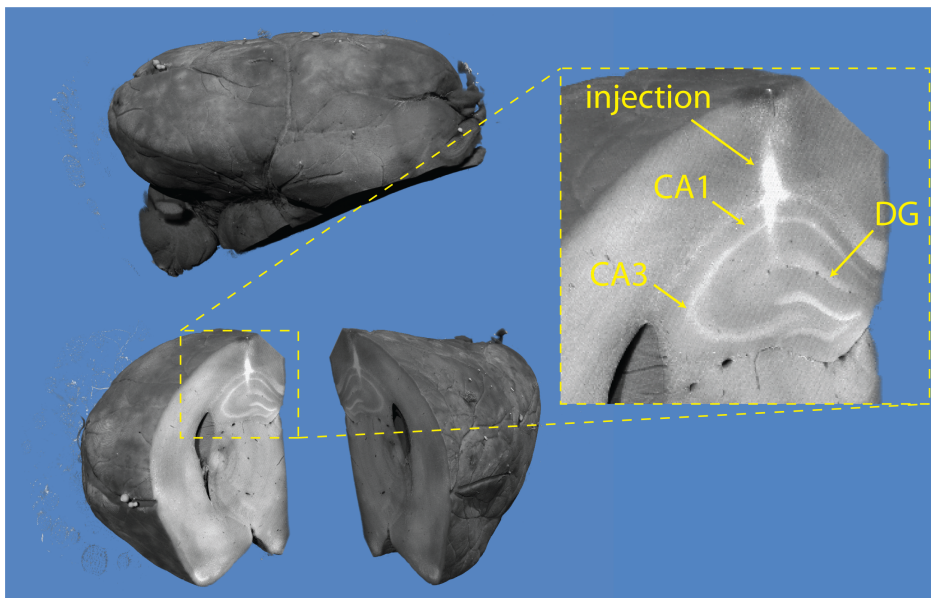


Figure 4.1: Virtual histology of a saline-injected mouse brain hemisphere. Volume renderings show the right hemisphere (top left) of a mouse from group 1 sacrificed seven days after saline injection. Virtual sectioning of the brain allows for identification of the injection site in the right dorsal hippocampus (bottom left). The pyramidal layers of the first and third fields of the *Cornu ammonis* (CA1 and CA3) as well as the layers of the dentate gyrus (DG) are visible in the zoom-in (right).

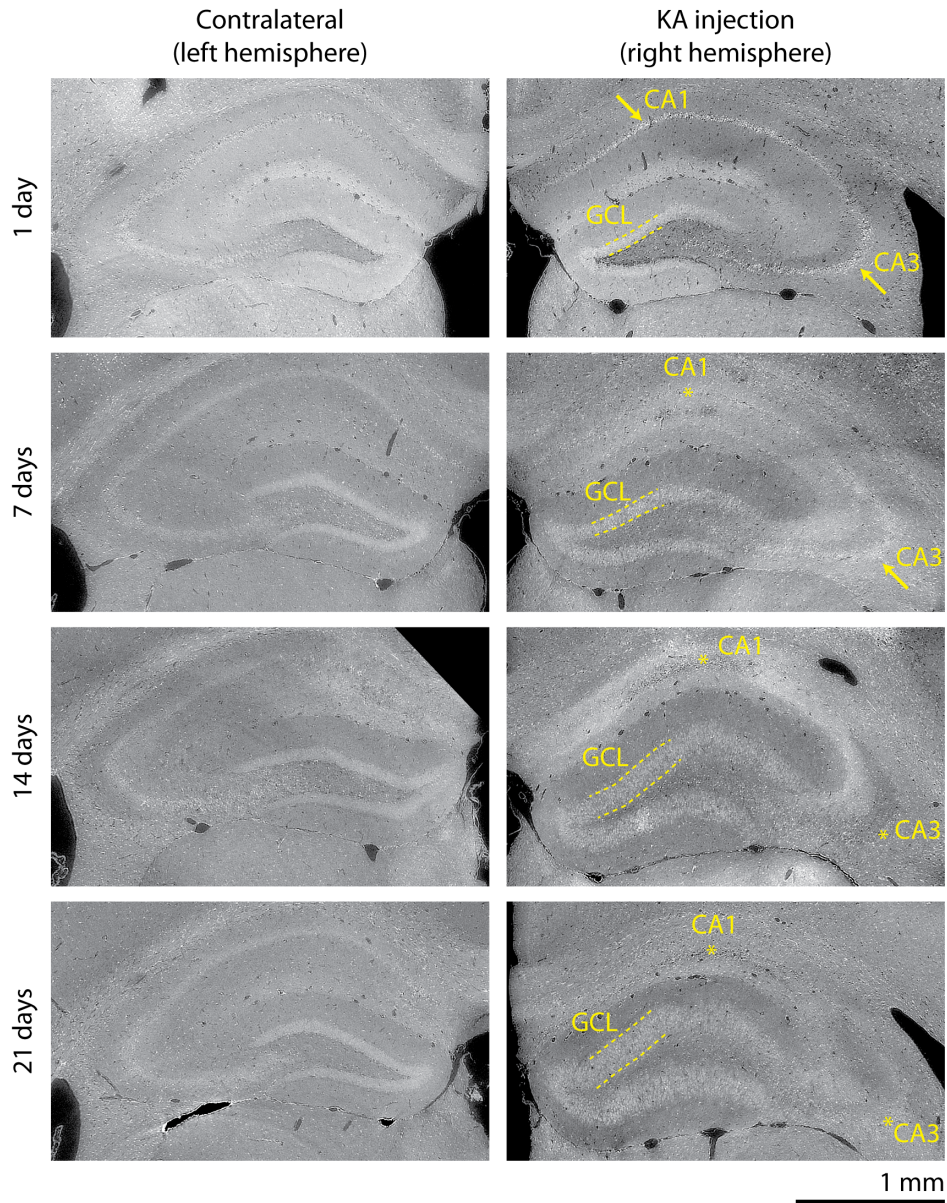


Figure 4.2: Virtual histology reveals pathological changes in mTLE. Indications of hippocampal sclerosis are observed with increasing time from KA injection (top to bottom) in virtual coronal slices. The loss of neurons in the pyramidal layer of the CA1 region (arrow: intact, star: neuronal loss) is observed 7 days after KA injection. Neuronal loss in the CA3 field is observed 14 days post-injection. Granular cell dispersion, characterized by an increased thickness of the granular cell layer (GCL, dashed line), is more prominent 14 and 21 days post injection. Hippocampal sclerosis is not observed in the contralateral brain hemispheres.

a cell-rich band of relatively high density. GCD was identified through an increasing thickness and decreasing mean density of the GCL. The increase in GCL thickness was observable in mice sacrificed 7 days after injection. Degree of GCD, i.e. thickness of GCL, increased with time from injection. It should be noted that compared with other time points, an increased contrast between the polymorph and molecular layers of the DG was observed for both hemispheres of the mice sacrificed 1 day after KA injection (Figure 4.2, top row).

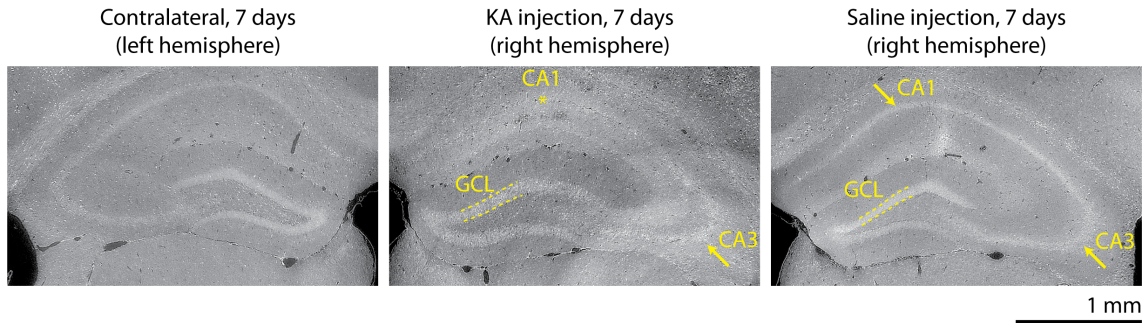


Figure 4.3: Comparing KA and saline injection. Virtual coronal slices through contralateral and ipsilateral hemispheres of a mouse sacrificed 7 days KA injection (left and center, respectively) are compared with the ipsilateral hemisphere of a mouse sacrificed 7 days after saline injection (right). Hippocampal sclerosis is not found in the contralateral or saline injected ipsilateral virtual slices, however signs of pyramidal neuron loss in the CA1 region as well as early signs of granular cell dispersion are observed for the ipsilateral hemisphere of the KA injected mouse.

Control mice sacrificed 7 days after saline injection were also imaged, see Figure 4.3. No pathology was identified in the control mice, with the ipsilateral hemisphere of the saline-injected mouse resembled the contralateral hemisphere of the KA-injected mice. For example, CA1 and CA3 regions remained intact and no signs of GCD were detected, cf. the 7 day post-KA-injection mouse in Figure 4.3. The injection site was identified in the three-dimensional datasets, see Figure 4.1. There, increased tissue density was observed but no further pathological signs were identified.

4.4.2 Comparing virtual histology with histology and immunohistochemistry

This work represents the first observation of mTLE pathology with X-ray virtual histology, therefore validation with gold standard conventional histology is essential. Immunofluorescent staining subsequent to virtual histology allowed for confirmation of hippocampal sclerosis, see Figure 4.4. NeuN-Iba1 double immunostained sections confirmed pyramidal neuron loss in the *Cornu ammonis* through diminished green NeuN signal and microglia proliferation through increasing red Iba1 signal. Note that the specificity of the immunostaining allowed for identification of pyramidal neuron loss in the CA3 at 7 days post injection, while the label-free virtual histology is more ambiguous, see Figure 4.4 middle. GCD was confirmed through increasing thickness and decreasing green NeuN signal of the GCL. The density of the GCL in the virtual histology was observed to correlate well with the intensity of the NeuN signal.

The electron-density-based contrast of label-free virtual histology was benchmarked with common histological and immunofluorescent stains. Figure 4.5 compares virtual histology of a KA-injected mouse 14 days post injection with photomicrographs of the same brain hemisphere after subsequent sectioning and staining with Hematoxylin and eosin (H&E), Nissl, NeuN-Iba1-DAPI, or GFAP-DAPI. For the histochemical stains, hematoxylin (purple/blue) stains cell nuclei, eosin (pink) stains extracellular matrix and cytoplasm, and Nissl (purple) stains cell bodies. For the immunofluorescent stains, NeuN (green) labels neurons, Iba1 (red) labels microglia, GFAP (green) labels astrocytes, and DAPI (blue) labels DNA. The density-related

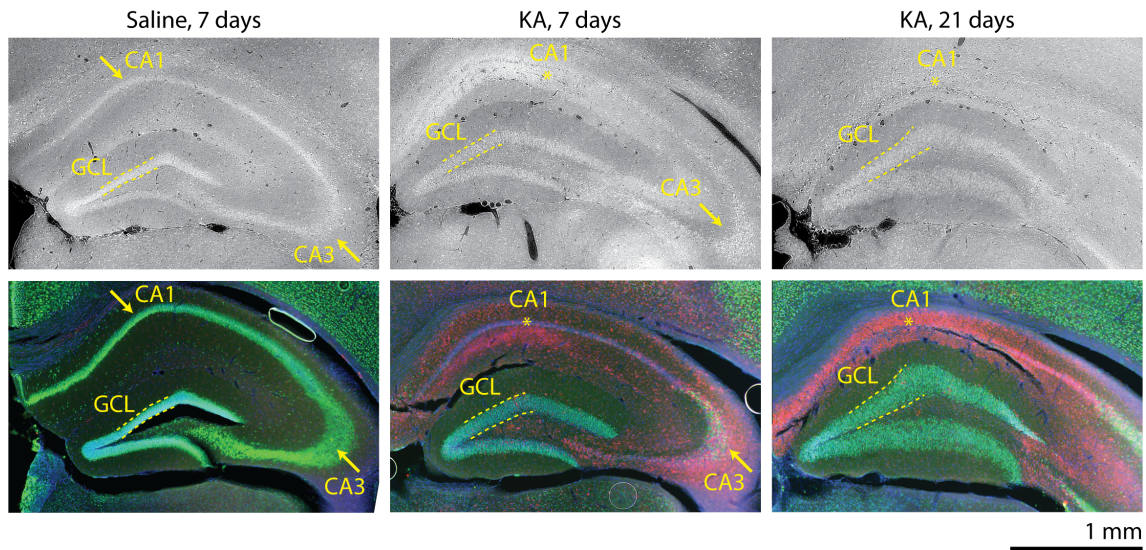


Figure 4.4: Comparison of histopathological findings with histology and immunohistochemistry. Virtual slices through the microtomography data (top row) and photomicrographs of subsequent NeuN-Iba1-DAPI (green-red-blue) immunostained sections (bottom row) from a similar position within the same mouse brains are shown. The fluorescent-labelled sections confirm neuronal loss (diminished green NeuN signal) and indicate microglia proliferation (increased red Iba1 signal) in the CA1 region. GCD is confirmed based on increased thickness and reduced fluorescence signal (diminished green NeuN signal) of the granule cell layer (GCL, dashed lines). The grayscale for the virtual histology images corresponds to [1st, 99th] percentile.

contrast of virtual histology shows correlation with some of the stains. For example, the virtual histology with inverted look-up table resembles the Nissl staining. The increased intensity of GCL and CA3 layers within the virtual histology also correlates with NeuN intensity. As histological sections had a thickness of 50 μm , an average of 30 slices from the 1.625 μm -wide voxel virtual histology data is also given. This increases the contrast-to-noise ratio of the virtual histology and makes the appearance more comparable with histology. It should also be noted that strain during sectioning and preparation of histological slides introduces artefacts, for example a gap opens between between the granular and polymorph layers of the DG as well as between the DG and thalamus.

4.4.3 Volume and density changes associated with the progression of mTLE

X-ray microtomography generates inherently three-dimensional datasets, providing a unique opportunity to study morphology changes associated with mTLE. Though the anatomy is identifiable in the virtual histology, fully automatic segmentation of the hippocampal formation based on the density-related contrast is challenging. Two-dimensional manual segmentation can be performed relatively fast, requiring about 1 minute per virtual slice. The isotropic, high-resolution nature of virtual histology presents a challenge, as segmenting ≈ 2000 of the 1.625 μm -thick virtual sections per brain hemisphere is prohibitively time-consuming. We used an approach based on three-dimensional interpolation of equally-spaced manually-segmented two-dimensional virtual coronal sections, see Figure 4.6. Here, $4 \times 4 \times 4$ binned datasets were used, as identification of individual cells was not needed and binning-related

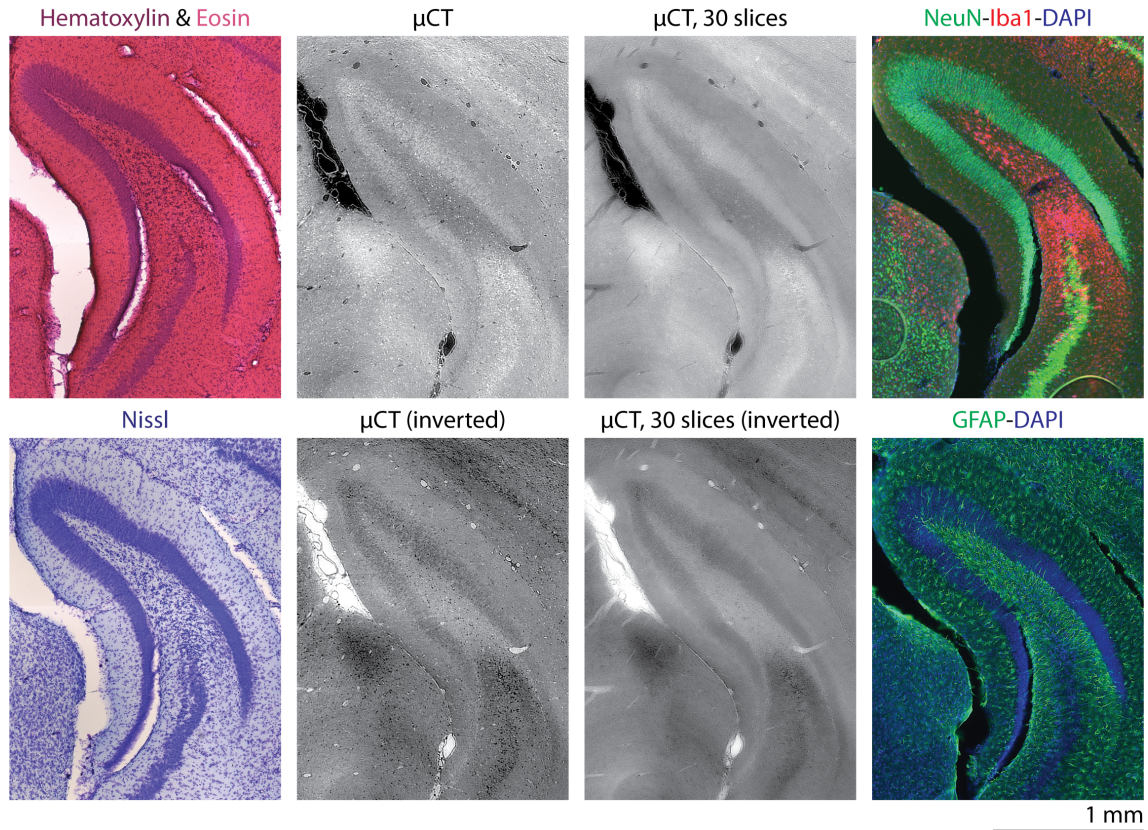


Figure 4.5: Benchmarking label-free virtual histology with histological and immunofluorescent staining. Following X-ray imaging, brain hemispheres were sectioned and sequentially stained with Hematoxylin and eosin (H&E), Nissl, NeuN-Iba1-DAPI (green-red-blue), and GFAP-DAPI (green-blue). Photomicrographs of stained sections are compared with virtual coronal sections in a similar position from the virtual histology volume from a mouse sacrificed 14 days after KA injection. The z -average of a $50\ \mu\text{m}$ -thick virtual section ($30 \times 1.625\ \mu\text{m}$ slices) and intensity-inverted images are also given for the microtomography dataset. Note that histological sections were $50\ \mu\text{m}$ thick.

contrast gains [104, 105] further accelerated manual segmentation.

For evaluation purposes, every 20th virtual sagittal slice from the right hemisphere of a mouse sacrificed 7 days after saline injection was also manually segmented. This resulted in 20 two-dimensional sagittal segmentations. We assessed the required interval of two-dimensional segmentations by determining the accuracy after interpolation (i.e. wrapping) of two-dimensional segmentation stacks with different spacings. The accuracy was measured by the Dice similarity coefficient (DSC) between the gold standard sagittal segmentations and interpolated coronal segmentations. We tested performance when interpolating every 5th, 10th, 20th, or 40th coronal slice. These corresponded to spacing of 8, 16, 32, and 64 μm respectively. The distribution of DSCs are shown in Figure 4.7 as box plots with mean values added as circles. DSC was assessed individually on the three regions of the segmentation, namely the polymorph, granular, and molecular layers of the DG. The accuracy of three-dimensional interpolation decreased with increasing coronal slice interval. However, the drop-off in segmentation quality between intervals of 5 and 10 slices was minor. Every 20th slice segmentation showed somewhat reduced qual-

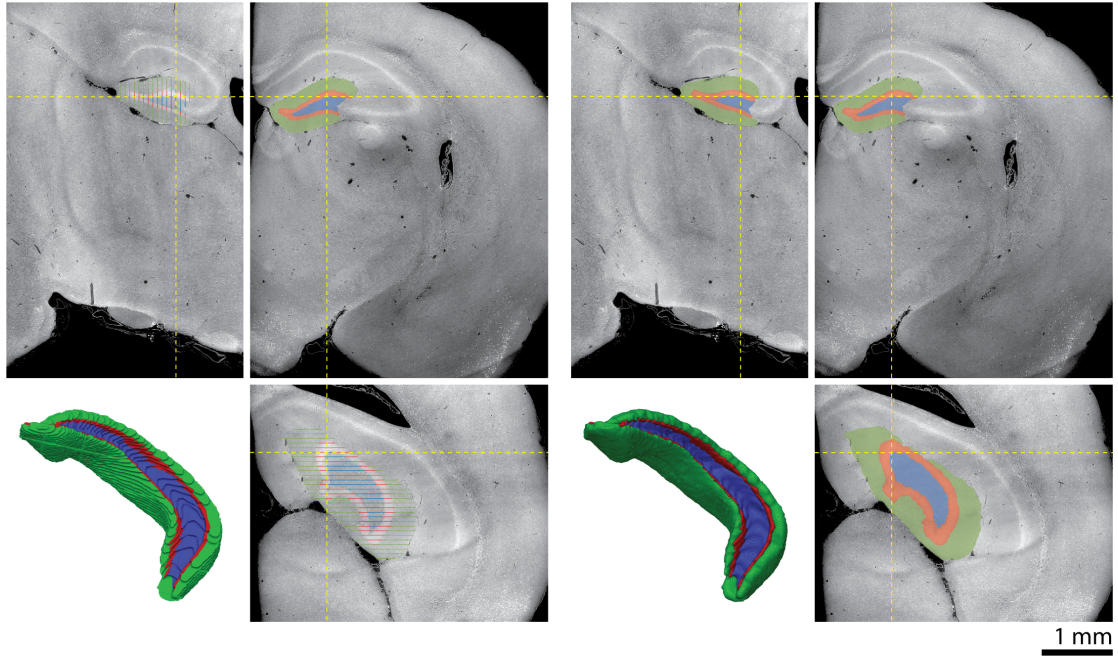


Figure 4.6: Segmentation of the dentate gyrus (DG) from the volumetric virtual histology data. Images illustrate segmentation of the right hemisphere of a mouse sacrificed 7 days after saline injection. (left) For every N^{th} virtual coronal slice ($N = 10$ shown), the molecular (green), granular (red), and polymorph layers (blue) of the DG were manually segmented. Three orthogonal slices and a volume rendering of the segmentations are shown. (right) The stack of slice-wise annotations were automatically wrapped to form a three-dimensional segmentation. Virtual slices are displayed with grayscale corresponding to [0.25, 99.75] percentiles of the values in the DG.

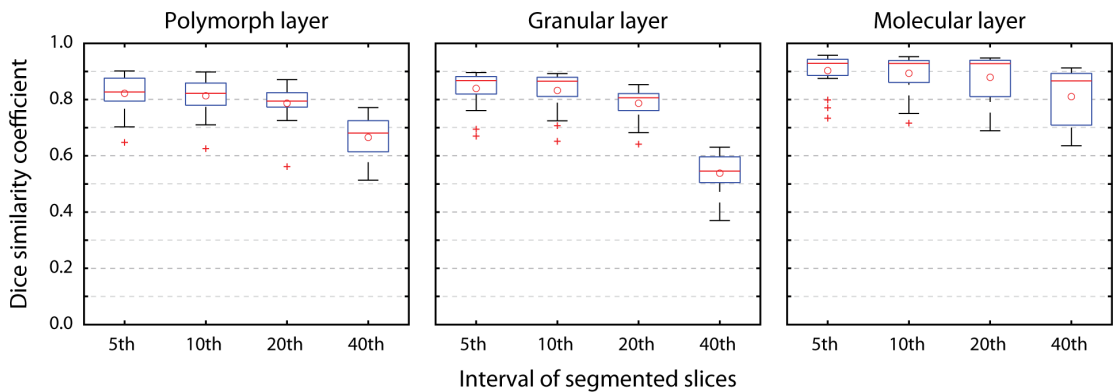


Figure 4.7: Validation of the dentate gyrus segmentation approach. Every 5th virtual coronal slice was segmented from a mouse sacrificed 7 days after saline injection. Three-dimensional segmentations were created by interpolation of two-dimensional segmentations of every 5th, 10th, 20th, and 40th coronal slice, which correspond to a spacing of 8, 16, 32, and 64 μm , respectively. Accuracy was assessed on independent two-dimensional segmentations of every 20th sagittal slice (20 total). Box plots show the distribution of Dice similarity coefficients for the sagittal slices with mean values added as circles.

ity, particularly in the granular layer. Therefore, an interval of every 10th slice was selected for segmentation of all datasets. For the 7 days post-saline-injection dataset used for validation, this provided median DSC of 0.82, 0.87, and 0.93 for the polymorph, granular, and molecular layers, respectively.

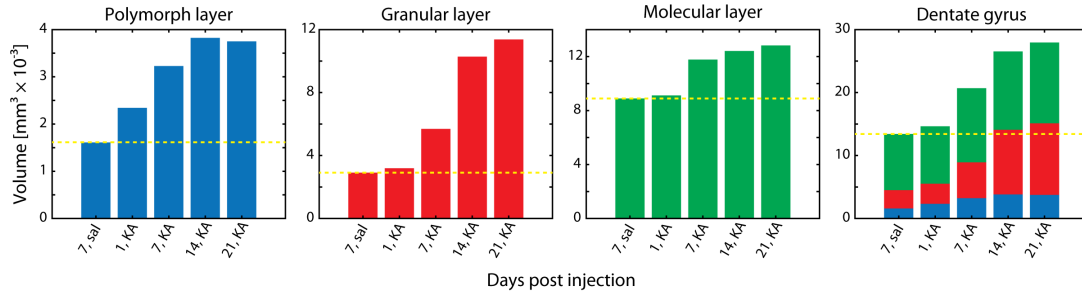


Figure 4.8: Volume changes within dentate gyrus (DG) after KA injection. Volumes of the segmented polymorph, granular, and molecular layers as well as the full DG are plotted for the mice 1, 7, 14, and 21 days after KA injection (left to right). For reference, the volumes for the 7 days post-saline-injection mouse are also shown (yellow dashed line).

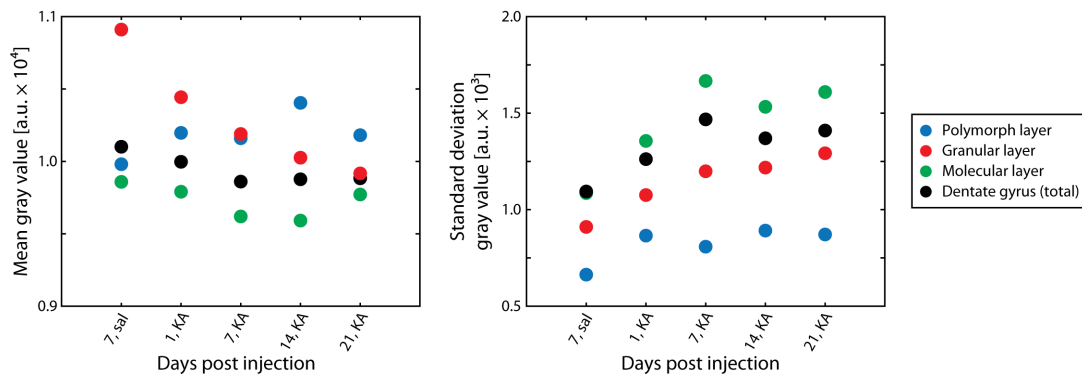


Figure 4.9: Density changes within the dentate gyrus (DG) after KA injection. Mean (left) and standard deviation (right) of the gray values within the segmented polymorph, granular, and molecular layers as well as the full DG are plotted for the mice 1, 7, 14, and 21 days after KA injection. For reference, the values for the 7 days post-saline-injection mouse are also shown (first point).

Volume changes within the three layers of the DG after KA injection were assessed based on the semi-automatic three-dimensional segmentations. Figure 4.8 shows the volume of the polymorph, granular, and molecular layers of the DG as well as the total of all three. Note that in accordance with Janz *et al.* [88], positions from $z = 0$ to $1820 \mu\text{m}$ along the rostro-caudal hippocampal axis were considered for volume calculations. This represents the extent of the region where GCD was observed after KA injection and was consistent in all datasets. All three regions showed increased volumes with increased time from injection to sacrifice. As expected from the observed GCD (see Figure 4.2), the volume of the granular layer substantially increased as mTLE progressed. The volume of the granular layer in the 21 days post-KA-injection mice was larger than the 1 day post-KA-injection mice (7 days post-saline-injection) by a factor of 3.6 (3.9). Additionally, the volumes of the polymorph and molecular layers increased. The result was a near doubling of volume of the entire DG for the 21 days post-KA-injection mice compared to both the 1 day post-KA-injection mouse and the 7 day post-saline-injection mouse.

The density within the three segmented regions of the DG were also assessed by the image intensity values as surrogate measures. Note that all measurements were taken with the same system and measurement parameters, i.e. same photon statistics. Figure 4.9 plots mean and standard deviation of the gray values found in the

polymorph, granular, and molecular layers of the DG. Mean intensity within the granular layer decreased with time from injection of KA to sacrifice. This is consistent with GCD and correlates with decreased intensity of NeuN fluorescent signal observed in the GCL, cf. Figure 4.4. Generally, KA injected mice showed increased standard deviation of intensity values for all three layers of the DG. The increased standard deviation is in accordance with visual observations of increased contrast between cells and surrounding media with progression of mTLE.

4.5 Discussion

This study presents virtual histology for investigation of mTLE. Here, *post mortem* label-free volumetric imaging with isotropic $(1.6\ \mu\text{m})^3$ voxels was based on phase contrast synchrotron radiation-based microtomography. A total of 14 mice brains were imaged, including 3 controls sacrificed 7 days after saline injection as well as 3, 2, 3, and 3 mice sacrificed 1, 7, 14, and 21 days after KA injection, respectively. Virtual histology identified pathological developments during epileptogenesis including hippocampal sclerosis. Virtual histology was compatible with subsequent conventional histology with a variety of histochemical and immunofluorescent stains. This allowed for comparison of virtual histology findings with well-established techniques. Virtual histology is also an inherently three-dimensional imaging modality, allowing for complete quantification of morphological changes in the DG as a result of mTLE. In this pilot study, segmentation was limited to one mouse per group. Given the promising results, all mice will be analyzed in future work.

Slice-to-volume registration, which is the process of finding the spatial correspondence between two-dimensional histological sections and volumetric imaging data, is a challenging task due to the large search space, small amount of two-dimensional data, multi-modality, and topology changes (e.g. cracks) [89]. Here, histology to virtual histology matching may prove simpler than histology to MRI matching, thanks to the comparable resolution and more similar appearance between label-free virtual histology and common stains, cf. Figure 4.5. In this study, correspondence was only approximately found with manual rotation and translation of the virtual histology datasets. Even after alignment of virtual histology with the atlas coordinate frame, several rotations were necessary for correspondence with coronally sectioned histology slices. The development of automatic or semi-automatic slice-to-volume registration is therefore desirable.

The present study employed single-distance propagation-based phase contrast based on Paganin's filter [64]. The resulting contrast is related to the electron density through the real part of the index of refraction, as opposed to highly specific histochemical or immunofluorescent stains that target proteins. Nevertheless, the electron density-based contrast identified pathological changes such as hippocampal sclerosis, see Figure 4.2. This is likely because the electron density correlates with presence of cells, which is supported by the comparison of the virtual histology with common stains, see Figure 4.5. For example, the decrease in mean intensity of the GCL, see Figure 4.9, can serve as an indication of GCD, analogous to decrease in fluorescence signal of NeuN. Still, unstained virtual histology alone was insufficient to identify astrocytes (labeled with GFAP) or differentiate between neurons (NeuN) and microglia (Iba1). While development of X-ray contrast agents may help these shortcomings, label-free imaging of paraffin-embedded tissue offers consistent and

easily repeatable results. This is an advantage over sectioning and staining, where variations in section thickness or stain intensity lead to challenges for automated analysis [14, 15]. As shown in this study, more specific conventional histology can be added subsequent to virtual histology for confirmation with a wide range of well-established stains.

Morphological analysis with sparse and artefact-prone two-dimensional histology slices only allows for approximations of volumes and surface areas of cell layers. These approximations can be refined with virtual histology, cf. Figure 4.8 and Figure 1(c) of Reference 88. Additionally, measured areas in histological sections, e.g. GCL area for quantification of GCD, depend on the angle of sectioning. Volume measurements may therefore prove more robust, though a detailed comparison is needed with precise correspondence of histological slice and virtual histology volume as well as a quantification of segmentation errors for both modalities. The three-dimensional nature of virtual histology should also allow for the introduction of novel morphological metrics for the quantification of mTLE.

In this study, we quantified the volume of the three layers of the DG based on segmentation. This segmentation was time-consuming, though it was accelerated by interpolation of segmentations of only every 10th virtual slice, see Figures 4.6 and 4.7. Standard automated approaches to segment unstained virtual histology data are suboptimal because of the lack of specificity. Anatomical borders are often based on connectivity or type of cells in a given region, which are unaccessible in the present virtual histology data. Improving contrast and spatial resolution will simplify segmentation, whether manual or automatic. For example, anatomical regions could be differentiated by microanatomical composition if cells, vessels, fibers, etc. can be resolved [106–108]. Atlas-based segmentation provides an alternative approach, where a segmentation problem is traded for a registration problem, with the potential advantage of transferring anatomical knowledge captured in the atlas to the image. Still, this may prove more difficult for the diseased states because atlases generally only provide labels for the healthy state. Morphology and density changes associated with mTLE pathology, see Figures 4.8 and 4.9, respectively, make registration of diseased to healthy states challenging.

A drawback of the present synchrotron radiation-based approach is the lack of accessibility. Laboratory-based microtomography may bridge this gap, with impressive results using conventional absorption contrast [71] and more recently phase contrast [67, 68]. As more of these systems enter the market [77], virtual histology can be integrated into the existing workflow of histopathology.

4.6 Conclusion

We have presented a *post mortem* virtual histology study of KA-induced mTLE in a mouse model. Label-free microtomography identified pathological changes associated with mTLE, namely pyramidal neuron loss in the CA1 and CA3 regions as well as GCD. Segmentation of the three-dimensional data allowed for quantification of volume and density changes within the DG during epileptogenesis. The findings were compared with conventional histology for confirmation of pathological observations and benchmarking of the electron-density based contrast with well-known histochemical and immunofluorescence stains. Thus, virtual histology can com-

plement conventional histology by providing three-dimensional, cellular-resolution histopathological analysis for the investigation of mTLE.

4.7 Acknowledgements

Beamtime for this experiment was provided by the European Synchrotron Radiation Facility (ESRF) through application MD 896. The authors thank A. Rack and the staff at beamline ID19 of ESRF for support during the beamtime. Financial support was provided by the Swiss National Science Foundation through projects 147172, 150164, and 185058, as well as R'Equip project 133802.

5 Microtomography of the entire mouse brain with sub-micrometer voxels

This chapter presents developments in mosaic-style microtomography acquisition and reconstruction for the visualization of entire organs with cellular resolution. The reconstruction pipeline introduced here has been applied for imaging paraffin-embedded nerve bundles [77], human teeth from Natural History Museum of Basel [78], and mouse brains [79]. This chapter focuses on the mouse brain, demonstrating the successful reconstruction of the entire mouse brain with $(0.65\ \mu\text{m})^3$ voxels.

5.1 Introduction

Neuroimaging is critical for decoding the brain's structure-function relationship [1]. However, even for smaller mammals such as mice, comprehensive brain mapping requires imaging over multiple orders of magnitude. For example, the width of the entire mouse brain is on the order of 10 mm, the size of cells is typically on the order of μm , synaptic connections can be thinner than 100 nm, and morphological changes on the order of a few nm can effect brain circuit function [1]. Therefore, a combination of imaging techniques are used to visualize the three-dimensional cytoarchitecture the brain. Among these, virtual histology based on X-ray microtomography holds promise as a *post mortem* modality that can provide volumetric brain imaging with isotropic μm resolution [65–68, 71]. However, current results mostly explore brain volumes on the order of tens of mm^3 , while the volume of even the mouse brain is around $450\ \text{mm}^3$ [109]. Thus, the extension of microtomography for full-brain mapping has generated considerable interest in recent years [110–114].

While hard X-ray penetration of soft tissues theoretically allows for microtomography of entire centimeter-sized brains, the field-of-view (FOV) is typically limited by detector array size. Standard detector arrays consist of a few thousand pixels in each direction, e.g. the Hamamatsu Orca Flash 4.0 V2 employed at the ANATOMIX Beamline of Synchrotron SOLEIL [115] consists of a 2048×2048 array of $6.5\ \mu\text{m}$ -wide pixels. Using $10\times$ magnification and a single detector FOV, $0.65\ \mu\text{m}$ pixel size and about $2\ \mu\text{m}$ resolution can be achieved but with FOV of only $1.3 \times 1.3 \times 1.3\ \text{mm}^3$. Such a local tomography scan already holds rich microanatomical information, see Figure 5.1. Still, the volume of the mouse brain is about $200\times$ larger than the imaged volume, therefore the FOV must be significantly extended for brain mapping.

Translation of the sample along the axis of rotation allows for extension of FOV *via* helical scans or, more commonly, stitching reconstructions from several height steps. Extending the FOV orthogonal to the rotation axis can be accomplished by either stitching reconstructions of local tomography scans [116, 117] or building mosaic projections with a common center-of-rotation (COR) prior to reconstruction [110, 118]. The former allows for standard reconstruction provided by the beamline, though corrections are needed for well-known local tomography artefacts from truncated sinograms [119–121] and dedicated software for non-rigid stitching is required if the sample is deformed during acquisition [117]. The latter is considered to be more dose- and time-efficient [111], though it requires a dedicated pipeline for mosaic

stitching of projections and reconstruction of large datasets [110, 113, 118].

This chapter presents the development of a custom reconstruction pipeline for mosaic-style tomographic reconstruction of entire organs with cellular resolution. Here, we discuss acquisition, data treatment, and implementation of this reconstruction pipeline. Finally, we demonstrate the reconstruction of the entire mouse brain with $0.65\ \mu\text{m}$ -wide voxels.

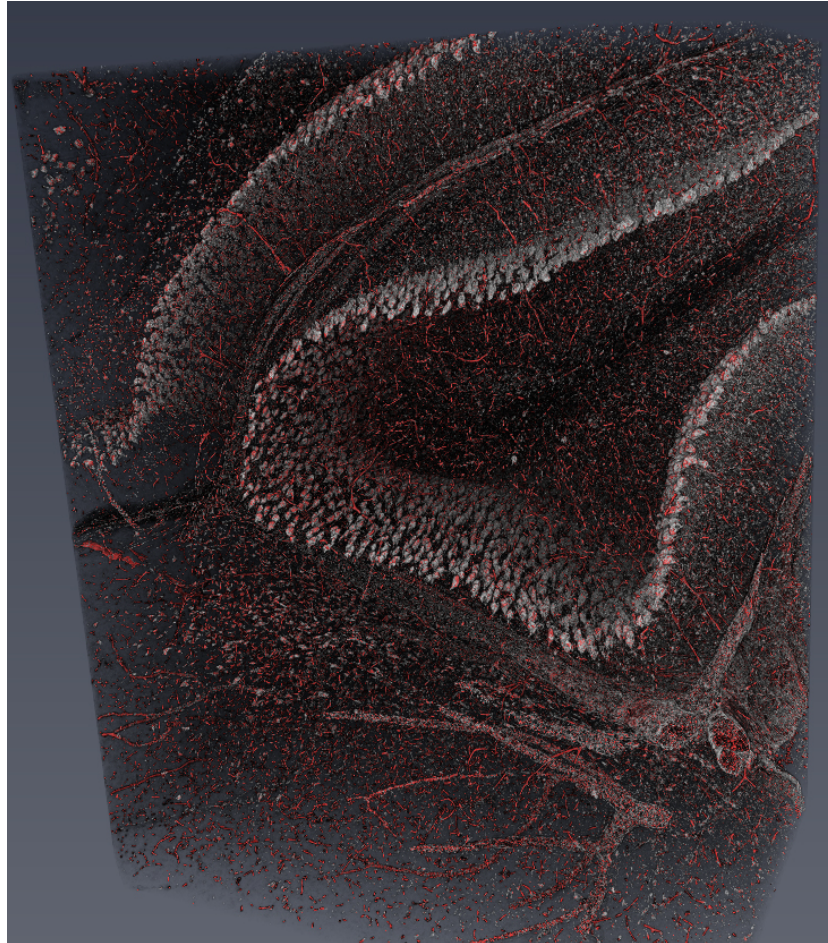


Figure 5.1: Volume rendering of a local tomography scan with $0.65\ \mu\text{m}$ -wide voxels within the cerebellum of a formalin-fixed mouse brain. The Purkinje cell layer (gray, cells are about $10\ \mu\text{m}$ in width) as well as the vasculature (red) are clearly visible. The rendering represents a cropped field-of-view of approximately $1\ \text{mm}^3$, while the volume of the entire mouse brain is around $450\ \text{mm}^3$. Measurements performed at the ANATOMIX Beamline [115] of Synchrotron SOLEIL (Gif-sur-Yvette, France). The volume rendering was made with *Amira 6.2.0* (Thermo Fisher Scientific Inc., Waltham, USA).

5.2 Materials and methods

5.2.1 Animals and tissue preparation

The brain of a one-year-old female C57BL/6JRj mouse (Janvier Labs, Le Genest-Saint-Isle, France) was extracted and transcardially perfused with 4% formaldehyde / phosphate buffered saline after sacrifice, then immersed in 4% formaldehyde / phosphate buffered saline. The mouse brain collected for this study was excess from

an experiment approved by the veterinary office of the Canton of Zurich (license number ZH067/17). For ethanol dehydration, the brain was immersed for two hours in 20 mL of each of 50%, 70%, 80%, 90%, and 100% ethanol (Carl Roth GmbH, Karlsruhe, Germany).

5.2.2 Extended-field microtomography acquisition

Imaging was performed on the ANATOMIX beamline at Synchrotron SOLEIL (Gif-sur-Yvette, France) [115]. A filtered white beam with effective mean photon energy of around 27 keV was used by setting the undulator gap to 5.5 mm and inserting 20 μm Au and 100 μm Cu filters into the beam path. The detector consisted of a 20 μm -thick LuAG scintillator coupled to a scientific CMOS camera (Hamamatsu Orca Flash 4.0 V2, 2048 \times 2048 pixels, 6.5 μm physical pixel size) *via* a lens system made of two photo objectives in tandem geometry resulting in a magnification factor of 10 and an effective pixel size of 0.65 μm [122]. The detector was placed 50 mm downstream of the sample for single-distance phase retrieval. This distance was selected based on $z_c = (2\Delta)^2/\lambda$ with pixel size Δ and wavelength λ to ensure that blurring from propagation-based phase contrast does not exceed two pixels [123]. The exposure time was set to 100 ms to fill half of the detector's dynamic range, which reduces severity of ring artefacts.

To cover the full width of the mouse brain, the detector's FOV had to be linearly extended by a factor of 8, which corresponds to a 64 \times larger reconstructed area. This was achieved with the acquisition of 4 rings, each consisting of a 360 $^\circ$ scan with offset COR, see Figure 5.2. The COR was offset by 0.6, 1.8, 3.0, and 4.2 mm for rings 1, 2, 3, and 4, respectively. Note that in this convention, 0 mm corresponds to the COR at the center of the detector FOV. Each ring scan consisted of 9000 projections. The acquisition of each ring took around 15 minutes, as a fly scan mode was used.

A total of 8 height steps were needed to cover the mouse brain from cerebellum to olfactory bulbs. Height steps were acquired with offset of 1.2 mm, corresponding to an overlap of about 200 pixels. The total scan time was slightly over 8 hours. Note that precise stage alignment is critical, as a reconstructed slice is 0.65 μm thick \times 10 mm wide.

5.2.3 Reconstruction of mosaic-style tomography data

The reconstruction pipeline has four main steps: (i) finding the COR and ring overlap positions; (ii) projection blending, ring artefact correction, and filtering for phase retrieval and/or noise reduction; (iii) tomographic reconstruction; and (iv) blending of height steps. These steps are laid out in greater detail in the following sections. The pipeline is built around a parameter file that contains information on the sample name, filtering, ring correction, output grayscale, and cropping options. This parameter file is accompanied by a table containing file paths to the raw data of the component ring scans. Each step of the pipeline is launched with only the parameter file as an input and is designed to run as batch jobs on either standard workstations or scientific computing infrastructure, e.g. with sciCORE at the University of Basel. Note that this reconstruction pipeline is not the one in use at ANATOMIX, which provides options for standard and off-axis reconstructions.

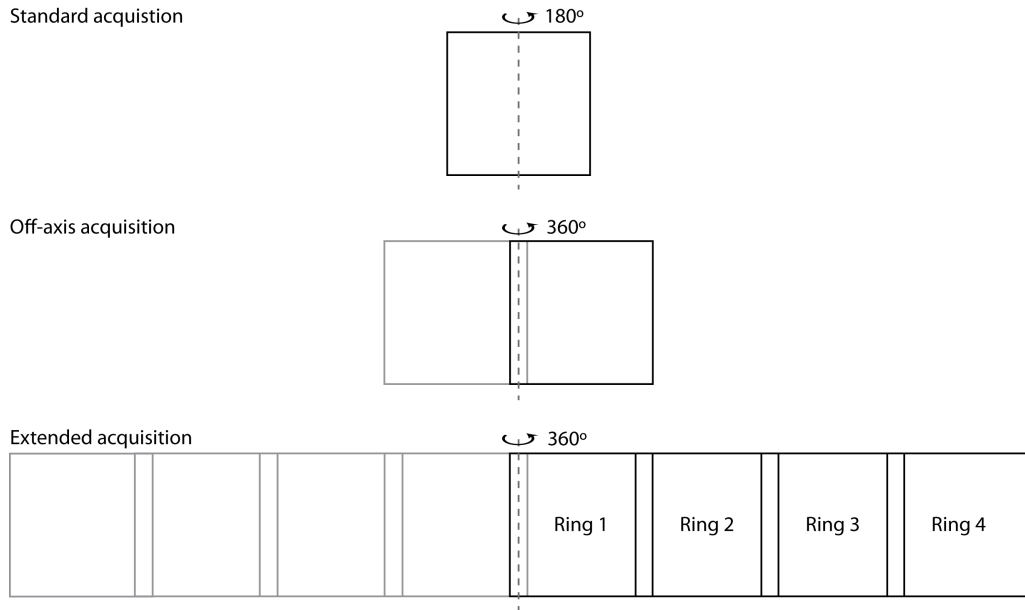


Figure 5.2: Lateral extension of the detector field-of-view (FOV) for microtomography. Standard tomographic acquisition involves 180° scans with the detector positioned such that the center-of-rotation (COR) of the object is projected onto the center of the detector FOV (top). The FOV is typically doubled by setting the detector position such that the COR to lies edge of the detector, often referred to as off-axis acquisition (middle). Acquiring subsequent “rings” with a common COR to create mosaic projections allows further extension of the FOV (bottom). For the measurements discussed in this chapter, FOV was increased by a factor of 8 linearly, corresponding to a factor of 64 in the reconstruction domain.

Center-of-rotation and overlap positions

The COR was found by maximizing cross-correlation in overlapping regions of projection pairs from the inner ring with rotation angles 180° apart. The mouse brain sample had relatively low contrast in projections, therefore 10 flat-field corrected projection pairs were used to increase robustness. Peaks in the cross-correlation curves were automatically identified and their prominence determined with the `Matlab` function `findpeaks`. The COR was selected from the prominence-weighted average positions of these peaks. Overlap positions between rings were also found by maximizing cross-correlation in overlapping regions of adjacent acquisitions. Again, prominence-weighted average peak positions from 10 flat-field corrected projection pairs were used to increase robustness. While the Eppendorf container holding the mouse brain was cylindrical, image content should be automatically detected when selecting projection pairs in the case of non-cylindrical samples where projections at certain rotation angles may have no sample in the FOV. The recorded motor position of the translation stage was used as an initial estimate to limit the search range for both COR and overlap positions between rings. The output of this step of the pipeline is a list of overlap positions that can be used to build mosaic projections.

Projection blending, ring artefact correction, and filtering of radiographic projections

The next step generates large FOV mosaic projections. Single FOV projections were flat-field corrected and phase retrieved with Paganin’s filter [64]. Projections

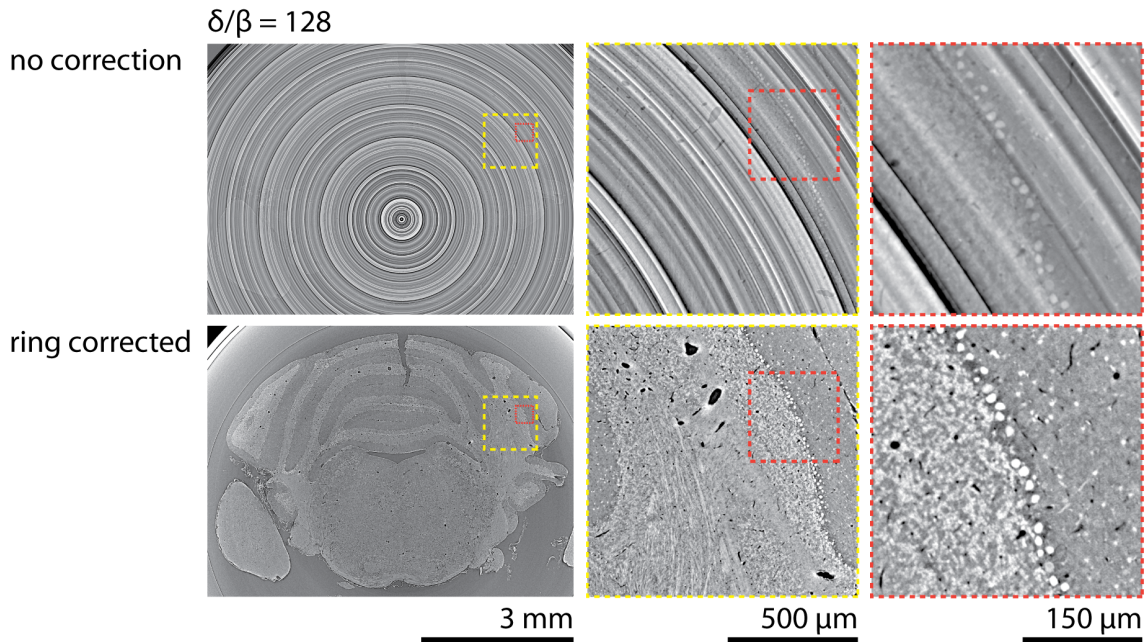


Figure 5.3: Ring correction employed for reconstruction of the mouse brain dataset. Here, reconstructions within the cerebellum after Paganin filtering with $\delta/\beta = 128$ are used for illustration. Ring artefacts were present in the reconstructions if no correction was applied (top). To reduce ring artefacts, the mean image of all flat-field corrected projections, offset by the mean value of that mean projection, was subtracted from each projection. This approach effectively removed ring artefacts (bottom). It is effective for homogenous samples, where weakly absorbing or phase shifting sample features “smear out” and only stationary structures responsible for rings remain in the mean projection.

were then combined with linear blending, i.e. $I_{\text{blend}} = \alpha I_r + (1 - \alpha) I_{r+1}$ with $\alpha \in [0, 1]$ linearly increasing through the overlap region, to create $8\times$ extended mosaic projections around 180° of rotation.

Ring artefacts were severe if no additional correction was applied, see Figure 5.3. The correction used for the mouse brain dataset was based on the mean of flat-field corrected projections over all rotation angles. This mean projection contained spot-like features that were the result of inhomogeneities that remained in fixed positions on the detector during acquisition. These inhomogeneities were the source of ring artefacts because they could not be fully removed by flat-field correction due to e.g. detector non-linearity. The mean projection was simply subtracted from all projections prior to reconstruction to remove ring artefacts. As the projections of the mouse brain dataset had relatively low contrast, sample features “smeared out” and were minimally effected by this subtraction. The mean projection subtraction introduced an offset that was added back as a scalar value corresponding to the mean of all pixels in the mean projection. Reconstructions of uncorrected and ring-artefact-corrected projections are compared in Figure 5.3.

The selection of both ring correction approach and filtering parameters *before* reconstruction of teravoxel-sized datasets are critical. Relatively fast previews were achieved by processing projections covering the full sample width but cropped in height to a stripe of e.g. 32 pixels. For the mouse brain, this was used to select

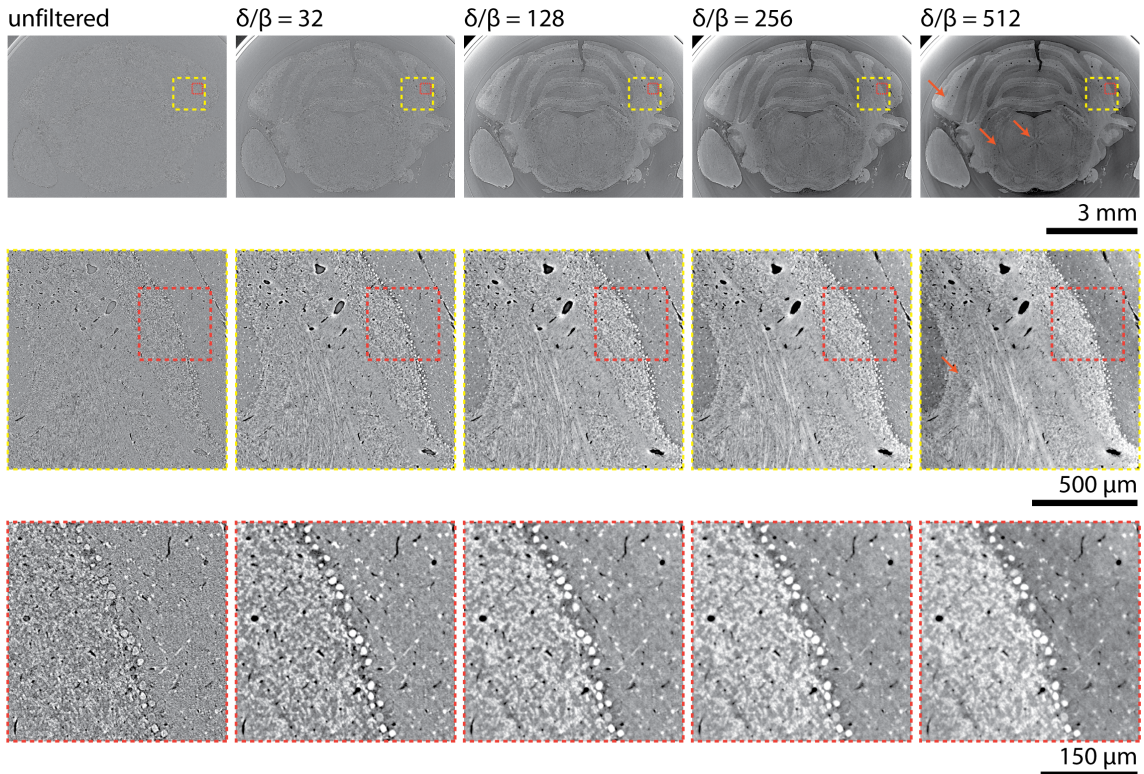


Figure 5.4: Selection of δ/β ratio for single distance phase retrieval. Cropped projections covering the cerebellum were ring corrected and phase retrieved with increasing δ/β (left to right) prior to reconstruction. The 4×4 binned full slice (top) as well as magnified views of unboxed regions-of-interest are shown (middle, bottom). Note that cupping and projection blending artefacts, indicated in the far right column with orange arrows, become more prominent at higher δ/β . All images were converted from [1st, 99th] percentiles to gray values in the range of [0, 255].

from a series of δ/β ratios for phase retrieval, see Figure 5.4. While the original intention of Paganin’s phase retrieval was for selection of δ/β based on *a priori* knowledge, this parameter is perhaps more often utilized to improve image quality or appearance of structures of interest [105]. This is thanks to the noise reduction properties of the filter, which comes at the expense of spatial resolution due to the Lorentzian shape of the Paganin filter in Fourier space [105]. In this experiment, *a priori* sample composition was not precisely known and model assumptions such as homogenous sample and monochromatic incident wave were not held. Thus, only semi-quantitative reconstructed values could be expected and an image processing view of the Paganin filter was considered, where δ/β was selected to improve image quality with minimal loss of spatial resolution. Increasing δ/β resulted in improved contrast-to-noise, with all tested values providing sufficient spatial resolution to visualize individual cells, e.g. within the granular and molecular layers (Figure 5.4 bottom row, left and right side of the images, respectively). With large δ/β , projection blending and cupping artefacts became more prominent (orange arrows).

The flat-field corrected, filtered, and blended projections as well as the mean of all projections were written to image files to be accessed for reconstruction. Each height step consisted of 4495 projections 14982×2048 in size, resulting in a data size of $4495 \times 117 \text{ MB} = 526 \text{ GB}$ at 32-bit precision. The projections were saved as

TIFFs with tiling such that 14982×32 strips could be quickly read for block-wise reconstruction.

Software	Algorithm	Time to reconstruct [s]				
		local 2048×2048	off-axis 4096×4096	2 rings 8192×8192	3 rings 12288×12288	4 rings 16384×16384
Matlab	<i>iradon</i>	3.7	30.0	238.6	833.8	1953.5
tomopy	<i>gridrec</i>	0.4	1.7	7.4	23.5	32.3
Speed-up factor		9.3	17.6	32.2	35.5	60.5

Table 5.1: Comparison of reconstruction speed with **Matlab**'s *iradon* (release R2020a), which is an implementation of a filtered backprojection, and **tomopy**'s *gridrec* (version 1.4.2). The speed-up factor represents the ratio of the former over the latter. The selected sizes represent acquisitions with increasing number of rings, ignoring overlap. A single sinogram was used with the number of projections equal to the grid width divided by 1.5, which is commonly used to avoid aliasing [32]. Sinograms were generated by replicating or cropping the mouse brain dataset and were composed of 32 bit floating point numbers. Tabulated values are the mean of five reconstructions of the same sinogram. Note that only the reconstruction was timed and file read/write were not considered. Reconstructions were performed on a workstation with an Intel® Xeon® 16 core CPU (E5-2637 v2, 3.50GHz) and 144 GB memory.

Tomographic reconstruction

Reconstruction was performed on blocks of 32 sinograms to avoid excessive memory consumption. While the first and second steps of the pipeline were written in **Matlab** (release R2020a, The MathWorks, Inc., Natick, USA), reconstruction based on **Matlab**'s built-in *filtered backprojection* algorithm (*iradon.m*) was limited for practical usage due to long reconstruction times. As a result, the open-source Python library **tomopy** (version 1.4.2) [124] was selected for its implementation of the *gridrec* reconstruction algorithm [125]. A comparison of reconstruction speeds for a range of dataset sizes was made and the results are presented in Table 5.1. For reconstruction of $8 \times$ extended field of view, represented in the table by 16384×16384 , **tomopy**'s *gridrec* was 60.5 times faster than **Matlab**'s *filtered backprojection*. For 2048 sinograms in one height step, this corresponds in a reduction of reconstruction time from 1111 hours (47 days) to 18.4 hours, although it should be noted that parallelization accelerates reconstruction times in both cases. Note that visual inspection showed no major differences in reconstruction quality between the two algorithms, see Figure 5.5.

The reconstruction section of the pipeline was thus written in Python (version 3.7.4). It read a block of sinograms, subtracted the mean image for ring correction, took the negative logarithm, performed tomographic reconstruction with **tomopy**'s *gridrec*, then cropped, re-scaled, and saved the reconstructed slices as a stack of TIFF images.

Height step blending

Overlap between height steps was determined using the open source registration toolbox **elastix** (version 4.9) [100, 101]. A translation transform was used with normalized correlation coefficient as a similarity metric. Height steps were combined using linear blending in the vertical direction within overlapping regions.

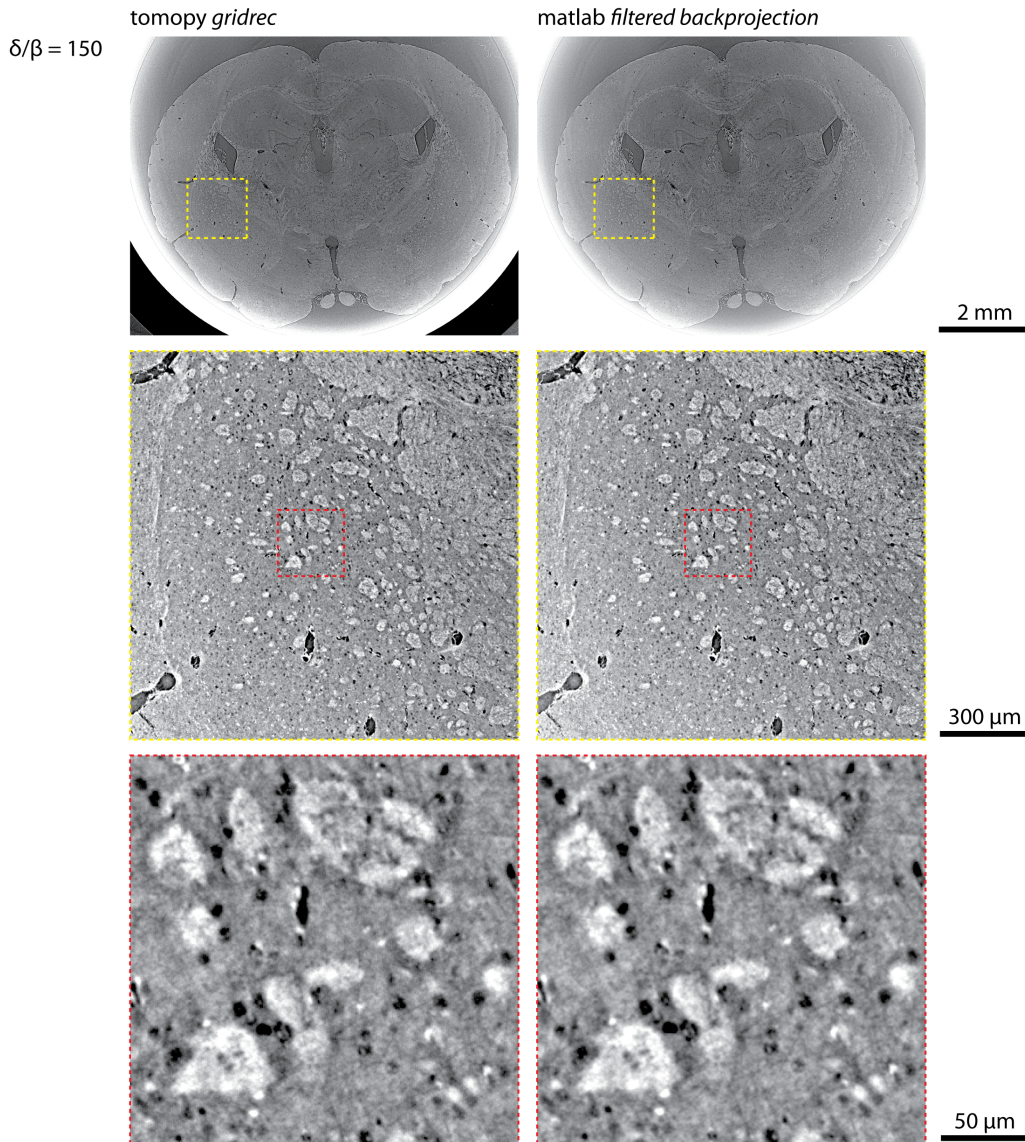


Figure 5.5: Comparison of reconstruction algorithms. The same 14982×4495 sinogram was reconstructed with `tomopy`'s `gridrec` (version 1.4.2) (left) and `Matlab`'s `filtered backprojection` (`iradon`, release R2020a) (right). The full brain coronal cross-section (top, binned 4×4) and unbinned magnified views within the caudate putamen (middle, bottom) are shown. All images are displayed with intensities from $[1^{\text{st}}, 99^{\text{th}}]$ percentiles mapped to gray values in the range of $[0, 255]$. Visual inspection reveals no discernible differences in image quality.

The full mouse brain, defined here from the top of the olfactory bulbs to the bottom of the cerebellum, was scanned with 8 height steps. The resulting stitched datasets contained $14982 \times 14982 \times 14784$ voxels, or 3.3 teravoxels. At 16-bit precision, the resulting datasets were 6.6 TB in size. It should be noted that this reflects the entire reconstructed FOV of 911 mm^3 . Cropping to more closely cover the approximately 450 mm^3 volume of the mouse brain will reduce data size, see e.g. Figure 5.6.

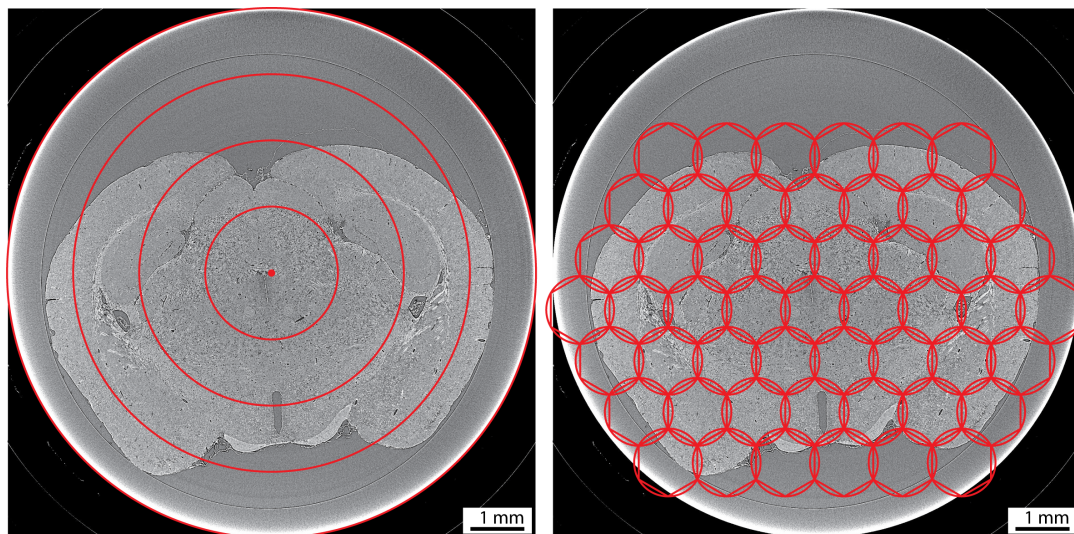


Figure 5.6: Illustration of microtomography of a full mouse brain with $0.65\ \mu\text{m}$ -wide voxels *via* mosaic tiling in the projection and reconstruction domains. The full coronal cross-sectional area of the mouse brain can be imaged by acquiring 4 offset center-of-rotation “rings” and stitching together the projections before reconstruction (left). Alternatively, local tomography scans can be stitched together after reconstruction, in this case approximately 50 local scans are needed (right). Note that the grid illustrating the local tomography approach (right) was not used for acquisition of the underlying image.

5.3 Results and discussion

Mosaic acquisition approaches

Mosaic tiling of both projections (hereafter referred to as projection blending) and local tomography reconstructions (hereafter reconstruction blending) have been suggested for large-volume microtomography [110–113]. The two approaches are illustrated in Figure 5.6, where 4 ring acquisitions are needed for projection blending and around 50 local tomography acquisitions are needed for reconstruction blending. The latter allows for direct reconstruction with the PyHST2-based [126] software provided by the ANATOMIX beamline [115]. The former requires a dedicated pipeline, as described above or in Ref. 110.

Angular sampling requirements for local tomography indicate that fewer projections are needed for aliasing artefact-free reconstructions [31,32] compared with projection blending. However, additional projections improve photon statistics, see Figure 5.7. Therefore, to achieve a similar signal-to-noise ratio, the number of projections for each local tomography scan must be the same as that used in each ring scan for projection blending. With this in mind, the reconstruction blending approach is significantly less time- and dose-efficient.

Another disadvantage of local tomography reconstruction is that the truncated sinograms must be padded to avoid cupping artefacts [119–121]. Here, local tomography scans were simulated by cropping the ring acquisition of the mouse brain around the center of rotation to produce a 2048×4495 truncated sinogram. Note that these sinograms reflect rotation about 360° . Sinograms were then padded on both sides and reconstructed, see Figure 5.8. To achieve artefact-free reconstructions, the truncated sinogram required padding of around 1000 pixels on both sides. More

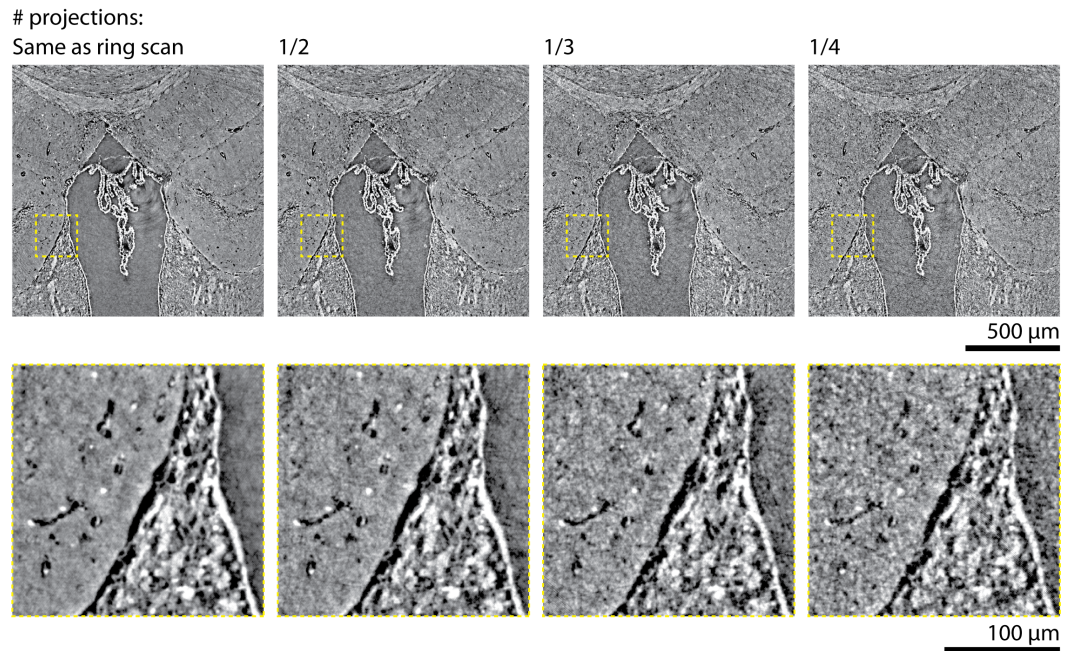


Figure 5.7: Angular sampling for local tomography scans. Local tomography acquisition was simulated by cropping projection-blended sinograms (14982×4495) about the center-of-rotation to produce truncated sinograms (2048×4495). Reconstructions with all 4495 projections as well as 1/2, 1/3, and 1/4 of the projections were reconstructed (left to right). While reconstructions with fewer projections did not have aliasing artefacts, the noise level increased. Magnified views are given to illustrate image quality (bottom row). Thus, local tomography acquisitions should have the same projection sampling as projection-blending ring acquisitions to obtain equal signal-to-noise ratio. Note that truncated sinograms were padded prior to reconstruction, see Figure 5.8. All images were converted from [1st, 99th] percentiles to gray values in the range of [0, 255].

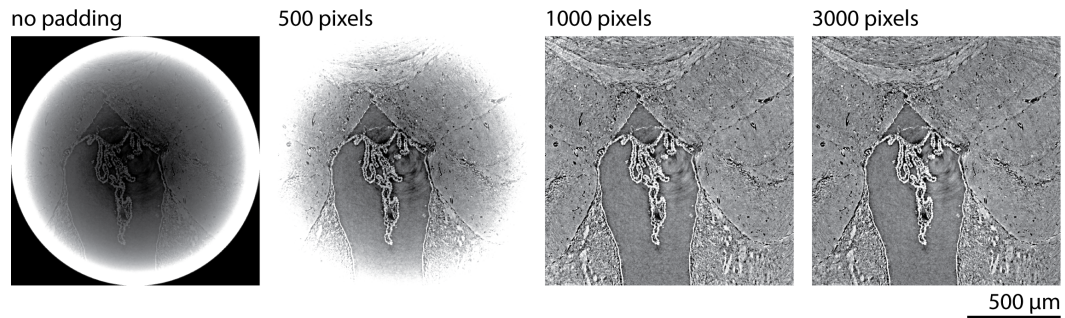


Figure 5.8: Padding to remove local tomography artefacts. Local tomography acquisition was simulated by cropping projection-blended sinograms (14982×4495) about the center-of-rotation to produce truncated sinograms (2048×4495). Increasing padding (left to right) removed the well-known cupping artefacts. Padding of 1000 pixels on both sides of the 2048-pixel-wide sinograms was sufficient to fully remove cupping. All images were converted from [1st, 99th] percentiles to gray values in the range of [0, 255].

padding is likely not necessary because the sample is relatively homogenous and low absorbing at the selected photon energy of about 27 keV. With this in mind, reconstruction blending requires reconstruction of 50 sinograms of size 4048×4495 , while projection blending requires reconstruction of a single sinogram of size 14982×4495 (i.e. 3.7×1 times larger than a single padded local sinogram).

Considerations for other samples

For the present imaging, the ethanol-dehydrated mouse brain was placed in an ethanol-filled Eppendorf container. This resulted in a relatively homogenous sample with cylindrical shape. For inhomogenous samples, an alternative ring artefact correction method may be needed. For the measured archaeological teeth [78], when the major axis of the approximately elliptical teeth was aligned with the beam direction, there was significant reflection of the beam which was captured in the mean projection. This resulted in generation of counter-rings. A similar case was seen in a slice of the mouse brain containing highly absorbing debris possibly from the skull, see Figure 5.9. In these cases, application of one or more ring artefact correction algorithms provided by the `tomopy` package [124] could be beneficial, for example those in Refs. [127, 128].

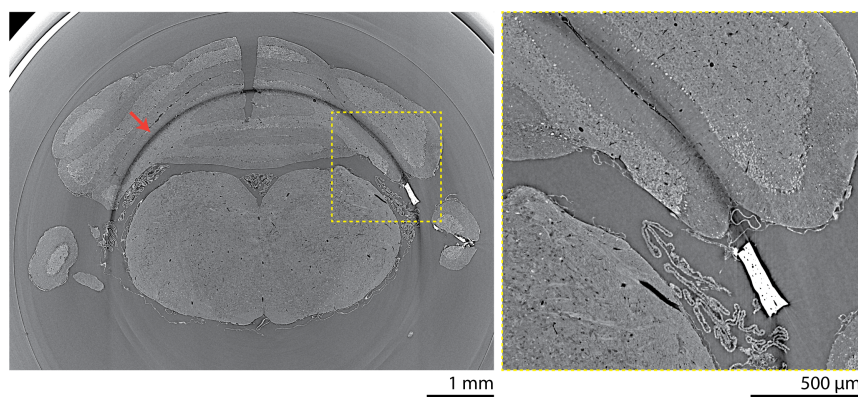


Figure 5.9: Counter-ring artefacts as a result of a piece of highly absorbing debris. A clear counter-ring (left side, red arrow) is created with radius equal to the distance of the debris from the center-of-rotation. A magnified view of the highly absorbing object, which is possibly part of the skull, is shown (yellow box, right). This highly absorbing debris contributes strongly to the mean projection, therefore generating a “shadow” of the object when the mean projection is subtracted from all projections. Only two instances of debris were found in the brain dataset, however an alternative ring correction would be necessary if highly absorbing materials were more common. Both images were converted from [1st, 99th] percentiles to gray values in the range of [0, 255].

It should also be noted overlap positions between ring acquisitions are found through cross-correlation. For non-cylindrical specimens, some projections do not have the sample in the field of view, particularly for outer rings. For example, see Figure 5.6, where the brain is not in the field of view for parts of the outermost ring. In this case, automatic selection of projections with image content will allow for more robust calculation of overlap positions.

Registration and segmentation of mosaic tomography data

Registration is an important tool for analysis of neuroimaging data and generation of brain atlases. Three-dimensional registration, particularly non-rigid registration, requires significant computational resources. In Chapter 3, the full mouse brain could only be non-rigidly registered after downsampling to 9.3 μm -wide voxels. Even then, B-spline grid spacing below 12 were not possible on a workstation with 144 GB RAM [80, 94]. These challenges could potentially be addressed with a hierarchical

approach with sub-volume registration for the full resolution steps.

Segmentation of anatomical regions can be challenging in label-free virtual histology. Terabyte-sized datasets require automated segmentation approaches. In certain cases, selection of an embedding material, see Chapter 3 (Refs. 79,93,94), can allow for simple semi-automatic segmentation. For example, fiber tracts can be segmented with region growing from a handful of manually defined seed points in an ethanol-dehydrated mouse brain. This is illustrated in Figure 5.10 based on the $3.1\ \mu\text{m}$ pixel size data found in Chapter 3 and Refs. 79,93,94. Automatic detection of cells [66,67] could also allow for determination of anatomical regions based on cell distributions [106–108]. Additionally, machine-learning based approaches have shown success for terabyte-scale microtomography segmentation, for example to segment 33729 glomeruli in a mouse kidney [129].

5.4 Conclusion

Extending the FOV of virtual histology is critical for brain mapping with true micrometer resolution. This chapter presents proof-of-concept imaging of an entire mouse brain with $0.65\ \mu\text{m}$ pixel size. This represents a $200\times$ increase in imaged volume compared with a single local tomography. Mosaic imaging methods were compared and a projection-blending approach was selected because of its time- and dose-efficiency. A dedicated data processing pipeline has been established for the reconstruction of these terabyte-sized datasets. This will enable novel quantification of brain microanatomy in health and disease. Going forward, the registration and segmentation of these large datasets will generate new challenges.

5.5 Acknowledgements

I would like to thank the following colleagues for their contributions to this section: Dr. Christine Tanner, Melissa Osterwalder, Dr. Georg Schulz, and Prof. Dr. Bert Müller of the Biomaterials Science Center, University of Basel; Dr. Timm Weitkamp and Dr. Mario Scheel of the ANATOMIX Beamline, Synchrotron SOLEIL; Marta Girona-Alarcón, Dr. Willy Kuo, and Prof. Dr. Vartan Kurtcuoglu of the Interface Group, Institute of Physiology, University of Zurich.

I would also like to thank Prof. Dr. Britta Engelhardt and her team at the Theodor Koch Institute, University of Bern for the inspiring scientific discussion and fruitful collaboration. Thanks to Dr. Virginia Meskenaite and Jeshua de Tenorio of the Institute of Physiology, University of Zurich for providing excess cadavers for sample extraction. Thanks to Prof. M.D. Ruslan Hlushchuk and his team at the Institute of Anatomy, University of Bern for supplying additional mice.

Beamtime at the ANATOMIX beamline was granted by Synchrotron SOLEIL under proposals 20190424 and 20200712. ANATOMIX is an Equipment of Excellence (EQUIPEX) funded by the Investments for the Future program of the French National Research Agency (ANR), project NanoimagesX, grant no. ANR-11-EQPX-0031. W.K. and V.K. acknowledge support from the Swiss National Science Foundation *via* NCCR Kidney.ch. V.K. acknowledges support from the Swiss National Science Foundation project no. 182683. G.R., C.T., M.O., and B.M. acknowledge support from the Swiss National Science Foundation project no. 185058.

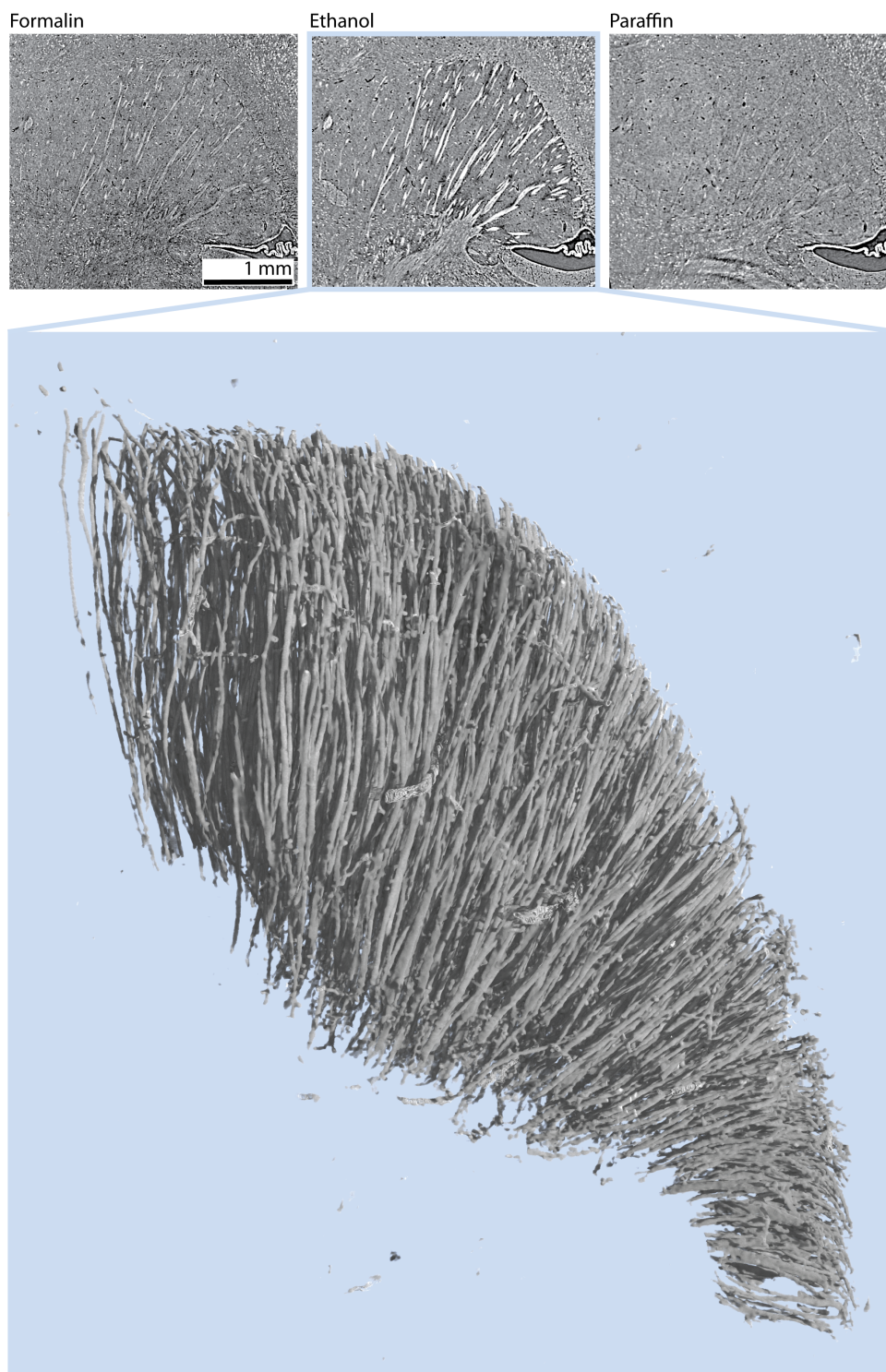


Figure 5.10: Ethanol dehydration allows for semi-automatic segmentation of fiber tracts illustrated with data from Chapter 3 (Refs. 79, 93, 94). Virtual sagittal slices through the $3.1\ \mu\text{m}$ -voxel datasets illustrate selection of embedding medium for contrast enhancement. The caudoputamen and fiber tracts are shown for registered datasets of the same formalin-fixed, ethanol-dehydrated, and paraffin-embedded brain (top). Semi-automatic segmentation based on region growing from a handful of manually defined seedpoints extracts the fiber tracts (bottom, volume rendering of segmentation). The grayscale range is given by the mean ± 2.5 standard deviations of the pixel intensities throughout the entire brain. Segmentation and volume rendering were done with VGStudio MAX 2.1 (Volume Graphics, Heidelberg, Germany).

6 Conclusions and Outlook

Single distance phase retrieval has allowed for X-ray virtual histology to routinely provide high soft tissue contrast with both synchrotron radiation and laboratory sources. Nevertheless, the underlying model assumptions such as monochromaticity or sample homogeneity are restrictive. Thus, in common usage, quantitative gray values are rarely achieved. Therefore, the primary goal should be the optimization of image quality considering the trade-off between contrast and spatial resolution. Future studies should explore performance of a larger group of filters across several samples with varying coherence, photon flux, and photon energy.

For high-resolution *post mortem* imaging, whether with histology, tissue clearing, electron microscopy, or virtual histology, tissue deformation is unavoidable. It was shown that microtomography can be used to quantify and correct these morphology changes. A similar methodology should be extended to microtomography of the mouse brain with sub- μm voxels to quantify changes in morphology and density at the sub-cellular level. An important next step is also the registration of high resolution virtual histology to *in vivo* or *in situ* magnetic resonance imaging. This will bring microanatomical information towards the living state and establish virtual histology as a valuable tool for atlas generation. It was also shown that tissue preparation can substantially improve X-ray contrast for neuroimaging. Standardization of tissue preparation within the virtual histology community could thus provide consistent, high image quality and more generalizable findings.

Despite virtual histology being well-established, it has not been widely applied in the field of neurological disorders. The presented study is among the first virtual histology investigations of mesial temporal lobe epilepsy and demonstrates its value for pathological investigation. The inherently three-dimensional information allows for unique quantification of morphological changes during epileptogenesis. Improved slice-to-volume registration will allow for direct validation with gold standard conventional histology. Additionally, streamlined segmentation will allow for extensive labelling to identify further morphological changes. Virtual histology is expected to provide more accurate morphological quantification than sparse two-dimensional sectioning or lower resolution magnetic resonance imaging, however this must be confirmed with a detailed quantification of segmentation accuracy and larger sample sizes.

Imaging of the entire mouse brain with $0.65\ \mu\text{m}$ pixel size was demonstrated with mosaic-style acquisition and a dedicated reconstruction pipeline. This offers vast amounts of microanatomical data, however processing the terabyte-sized data remains a major challenge. Both segmentation and registration of these huge datasets will present obstacles for more widespread adoption. Looking forward, the volume of the human brain is 3000 times larger than the mouse brain. Suitable preparation of the entire human brain for virtual histology has not been explored. Fixation and embedding will require months compared to several hours for the mouse. Contrast will again be an issue due to the higher photon energy required to penetrate the decimeter-sized human brain. Acquisition times, which were manageable at around ten hours for the mouse brain, will substantially increase. Finally, data size on the

petabyte scale will push the limits of currently available computing infrastructure. In conclusion, this thesis has presented several developments in methodology and applications for neuroimaging with hard X-ray microtomography-based virtual histology. Virtual histology has fulfilled much of its promise for large-scale volumetric brain imaging with cellular resolution, though the limits must still be explored. An important continuing goal is the identification of interdisciplinary collaborations to fully exploit its value for neuroscience.

Bibliography

- [1] J. W. Lichtman and W. Denk. “The Big and the Small: Challenges of Imaging the Brain’s Circuits.” *Science* 334(6056), (2011) 618–623. doi:10.1126/science.1209168.
- [2] S. Herculano-Houzel, B. Mota, and R. Lent. “Cellular scaling rules for rodent brains.” *Proceedings of the National Academy of Sciences* 103(32), (2006) 12138–12143. doi:10.1073/pnas.0604911103.
- [3] F. A. C. Azevedo, L. R. B. Carvalho, L. T. Grinberg, J. M. Farfel, R. E. L. Ferretti, R. E. P. Leite, W. J. Filho, R. Lent, and S. Herculano-Houzel. “Equal numbers of neuronal and nonneuronal cells make the human brain an isometrically scaled-up primate brain.” *Journal of Comparative Neurology* 513(5), (2009) 532–541. doi:10.1002/cne.21974.
- [4] J. O. S. H. Cleary and A. R. Guimarães. “Magnetic Resonance Imaging.” In L. M. McManus and R. N. Mitchell (Editors), “Pathobiology of Human Disease,” 3987–4004. Academic Press, San Diego, 2014. doi:10.1016/B978-0-12-386456-7.07609-7.
- [5] K. Amunts, C. Lepage, L. Borgeat, H. Mohlberg, T. Dickscheid, M.-É. Rousseau, S. Bludau, P.-L. Bazin, L. B. Lewis, A.-M. Oros-Peusquens, N. J. Shah, T. Lippert, K. Zilles, and A. C. Evans. “BigBrain: An Ultrahigh-Resolution 3D Human Brain Model.” *Science* 340(6139), (2013) 1472–1475. doi:10.1126/science.1235381.
- [6] H. Benveniste, K. Kim, L. Zhang, and G. A. Johnson. “Magnetic Resonance Microscopy of the C57BL Mouse Brain.” *NeuroImage* 11(6), (2000) 601–611. doi:10.1006/nimg.2000.0567.
- [7] A. E. Dorr, J. P. Lerch, S. Spring, N. Kabani, and R. M. Henkelman. “High resolution three-dimensional brain atlas using an average magnetic resonance image of 40 adult C57Bl/6J mice.” *NeuroImage* 42(1), (2008) 60–69. doi:10.1016/j.neuroimage.2008.03.037.
- [8] J. O. Cleary, F. K. Wiseman, F. C. Norris, A. N. Price, M. Choy, V. L. J. Tybulewicz, R. J. Ordidge, S. Brandner, E. M. C. Fisher, and M. F. Lythgoe. “Structural correlates of active-staining following magnetic resonance microscopy in the mouse brain.” *NeuroImage* 56(3), (2011) 974–983. doi:10.1016/j.neuroimage.2011.01.082.
- [9] G. M. Fatterpekar, T. P. Naidich, B. N. Delman, J. G. Aguinaldo, S. H. Gultekin, C. C. Sherwood, P. R. Hof, B. P. Drayer, and Z. A. Fayad. “Cytoarchitecture of the Human Cerebral Cortex: MR Microscopy of Excised Specimens at 9.4 Tesla.” *American Journal of Neuroradiology* 23(8), (2002) 1313–1321.
- [10] G. M. Fatterpekar, B. N. Delman, W. W. Boonn, S. H. Gultekin, Z. A. Fayad, P. R. Hoff, and T. P. Naidich. “MR microscopy of normal human brain.” *Magnetic Resonance Imaging Clinics of North America* 11(4), (2003) 641–653. doi:10.1016/S1064-9689(03)00071-0.
- [11] D. S. Novikov, E. Fieremans, S. N. Jespersen, and V. G. Kiselev. “Quantifying

- brain microstructure with diffusion MRI: Theory and parameter estimation.” *NMR in Biomedicine* 32(4), (2019) e3998. doi:10.1002/nbm.3998.
- [12] C. F. A. Culling. *Handbook of Histopathological and Histochemical Techniques: Including Museum Techniques*. Butterworth-Heinemann, 2013.
- [13] J. D. Bancroft. *Theory and Practice of Histological Techniques*. Elsevier Health Sciences, 2008.
- [14] R. Farhoodi, B. J. Lansdell, and K. P. Kording. “Quantifying How Staining Methods Bias Measurements of Neuron Morphologies.” *Frontiers in Neuroinformatics* 13, (2019) 36. doi:10.3389/fninf.2019.00036.
- [15] K. Milligan, A. Balwani, and E. Dyer. “Brain mapping at high resolutions: Challenges and opportunities.” *Current Opinion in Biomedical Engineering* 12, (2019) 126–131. doi:10.1016/j.cobme.2019.10.009.
- [16] J. Pichat, J. E. Iglesias, T. Yousry, S. Ourselin, and M. Modat. “A Survey of Methods for 3D Histology Reconstruction.” *Medical Image Analysis* 46, (2018) 73–105. doi:10.1016/j.media.2018.02.004.
- [17] M. Germann, A. Morel, F. Beckmann, A. Andronache, D. Jeanmonod, and B. Müller. “Strain fields in histological slices of brain tissue determined by synchrotron radiation-based micro computed tomography.” *Journal of Neuroscience Methods* 170(1), (2008) 149–155. doi:10.1016/j.jneumeth.2008.01.011.
- [18] P. S. Tsai, B. Friedman, A. I. Ifarraguerri, B. D. Thompson, V. Lev-Ram, C. B. Schaffer, Q. Xiong, R. Y. Tsien, J. A. Squier, and D. Kleinfeld. “All-Optical Histology Using Ultrashort Laser Pulses.” *Neuron* 39(1), (2003) 27–41. doi:10.1016/S0896-6273(03)00370-2.
- [19] T. Ragan, L. R. Kadiri, K. U. Venkataraju, K. Bahlmann, J. Sutin, J. Taranda, I. Arganda-Carreras, Y. Kim, H. S. Seung, and P. Osten. “Serial two-photon tomography for automated ex vivo mouse brain imaging.” *Nature Methods* 9(3), (2012) 255–258. doi:10.1038/nmeth.1854.
- [20] A. Li, H. Gong, B. Zhang, Q. Wang, C. Yan, J. Wu, Q. Liu, S. Zeng, and Q. Luo. “Micro-Optical Sectioning Tomography to Obtain a High-Resolution Atlas of the Mouse Brain.” *Science* 330(6009), (2010) 1404–1408. doi:10.1126/science.1191776.
- [21] J. Wu, Y. He, Z. Yang, C. Guo, Q. Luo, W. Zhou, S. Chen, A. Li, B. Xiong, T. Jiang, and H. Gong. “3D BrainCV: Simultaneous visualization and analysis of cells and capillaries in a whole mouse brain with one-micron voxel resolution.” *NeuroImage* 87, (2014) 199–208. doi:10.1016/j.neuroimage.2013.10.036.
- [22] S. W. Oh, J. A. Harris, L. Ng, B. Winslow, N. Cain, S. Mihalas, Q. Wang, C. Lau, L. Kuan, A. M. Henry, M. T. Mortrud, B. Ouellette, T. N. Nguyen, S. A. Sorensen, C. R. Slaughterbeck, W. Wakeman, Y. Li, D. Feng, A. Ho, E. Nicholas, K. E. Hirokawa, P. Bohn, K. M. Joines, H. Peng, M. J. Hawrylycz, J. W. Phillips, J. G. Hohmann, P. Wohnoutka, C. R. Gerfen, C. Koch, A. Bernard, C. Dang, A. R. Jones, and H. Zeng. “A mesoscale connectome of the mouse brain.” *Nature* 508(7495), (2014) 207–214. doi:10.1038/nature13186.
- [23] K. Chung, J. Wallace, S.-Y. Kim, S. Kalyanasundaram, A. S. Andalman, T. J. Davidson, J. J. Mirzabekov, K. A. Zalocusky, J. Mattis, A. K. Denisin, S. Pak, H. Bernstein, C. Ramakrishnan, L. Grose, V. Gradinaru, and

- K. Deisseroth. “Structural and molecular interrogation of intact biological systems.” *Nature* 497(7449), (2013) 332–337. doi:10.1038/nature12107.
- [24] K. Chung and K. Deisseroth. “CLARITY for mapping the nervous system.” *Nature Methods* 10(6), (2013) 508–513. doi:10.1038/nmeth.2481.
- [25] D. S. Richardson and J. W. Lichtman. “Clarifying Tissue Clearing.” *Cell* 162(2), (2015) 246–257. doi:10.1016/j.cell.2015.06.067.
- [26] M. Helmstaedter, K. L. Briggman, and W. Denk. “High-accuracy neurite reconstruction for high-throughput neuroanatomy.” *Nature Neuroscience* 14(8), (2011) 1081–1088. doi:10.1038/nn.2868.
- [27] S. Mikula, J. Binding, and W. Denk. “Staining and embedding the whole mouse brain for electron microscopy.” *Nature Methods* 9(12), (2012) 1198–1201. doi:10.1038/nmeth.2213.
- [28] K. L. Briggman and D. D. Bock. “Volume electron microscopy for neuronal circuit reconstruction.” *Current Opinion in Neurobiology* 22(1), (2012) 154–161. doi:10.1016/j.conb.2011.10.022.
- [29] A. L. Eberle, S. Mikula, R. Schalek, J. Lichtman, M. L. K. Tate, and D. Zeidler. “High-resolution, high-throughput imaging with a multibeam scanning electron microscope.” *Journal of Microscopy* 259(2), (2015) 114–120. doi:10.1111/jmi.12224.
- [30] W. Yin, D. Brittain, J. Borseth, M. E. Scott, D. Williams, J. Perkins, C. S. Own, M. Murfitt, R. M. Torres, D. Kapner, G. Mahalingam, A. Bleckert, D. Castelli, D. Reid, W.-C. A. Lee, B. J. Graham, M. Takeno, D. J. Bum-barger, C. Farrell, R. C. Reid, and N. M. da Costa. “A petascale automated imaging pipeline for mapping neuronal circuits with high-throughput transmission electron microscopy.” *Nature Communications* 11(1), (2020) 4949. doi:10.1038/s41467-020-18659-3.
- [31] S. R. Stock. *MicroComputed Tomography: Methodology and Applications*. CRC Press, Boca Raton, 2018. doi:10.1201/9781420058772.
- [32] A. C. Kak and M. Slaney. *Principles of Computerized Tomographic Imaging*. Classics in Applied Mathematics. Society for Industrial and Applied Mathematics, 2001. doi:10.1137/1.9780898719277.
- [33] M.-C. Zdora. “Principles of X-ray Imaging.” In M.-C. Zdora (Editor), “X-Ray Phase-Contrast Imaging Using Near-Field Speckles,” Springer Theses, 11–57. Springer International Publishing, Cham, 2021. doi:10.1007/978-3-030-66329-2_2.
- [34] R. Mizutani, A. Takeuchi, K. Uesugi, M. Ohyama, S. Takekoshi, R. Y. Osamura, and Y. Suzuki. “Three-dimensional microtomographic imaging of human brain cortex.” *Brain Research* 1199, (2008) 53–61. doi:10.1016/j.brainres.2008.01.029.
- [35] A. Lareida, F. Beckmann, A. Schrott-Fischer, R. Glueckert, W. Freysinger, and B. Müller. “High-resolution X-ray tomography of the human inner ear: Synchrotron radiation-based study of nerve fibre bundles, membranes and ganglion cells.” *Journal of Microscopy* 234(1), (2009) 95–102. doi:10.1111/j.1365-2818.2009.03143.x.

- [36] T. Böhm, K. Joseph, M. Kirsch, R. Moroni, A. Hilger, M. Osenberg, I. Manke, M. Johnston, T. Stieglitz, U. G. Hofmann, C. A. Haas, and S. Thiele. “Quantitative synchrotron X-ray tomography of the material-tissue interface in rat cortex implanted with neural probes.” *Scientific Reports* 9(1), (2019) 7646. doi:10.1038/s41598-019-42544-9.
- [37] G. E. Barbone, A. Bravin, A. Mittone, M. J. Kraiger, M. Hrabě de Angelis, M. Bossi, E. Ballarini, V. Rodriguez-Menendez, C. Ceresa, G. Cavalletti, and P. Coan. “Establishing sample-preparation protocols for X-ray phase-contrast CT of rodent spinal cords: Aldehyde fixations and osmium impregnation.” *Journal of Neuroscience Methods* 339, (2020) 108744. doi:10.1016/j.jneumeth.2020.108744.
- [38] R. Anderson and A. M. Maga. “A Novel Procedure for Rapid Imaging of Adult Mouse Brains with MicroCT Using Iodine-Based Contrast.” *PLOS ONE* 10(11), (2015) e0142974. doi:10.1371/journal.pone.0142974.
- [39] M. d. C. Fonseca, B. H. S. Araujo, C. S. B. Dias, N. L. Archilha, D. P. A. Neto, E. Cavalheiro, H. Westfahl, A. J. R. da Silva, and K. G. Franchini. “High-resolution synchrotron-based X-ray microtomography as a tool to unveil the three-dimensional neuronal architecture of the brain.” *Scientific Reports* 8(1), (2018) 12074. doi:10.1038/s41598-018-30501-x.
- [40] L. Jiang, C. Li, M. Li, X. Yin, T. Wu, C. Duan, Y. Cao, H. Lu, and J. Hu. “Simultaneous 3D Visualization of the Microvascular and Neural Network in Mouse Spinal Cord Using Synchrotron Radiation Micro-Computed Tomography.” *Neuroscience Bulletin* doi:10.1007/s12264-021-00715-7.
- [41] M. Busse, M. Müller, M. A. Kimm, S. Ferstl, S. Allner, K. Achterhold, J. Herzen, and F. Pfeiffer. “Three-dimensional virtual histology enabled through cytoplasm-specific X-ray stain for microscopic and nanoscopic computed tomography.” *Proceedings of the National Academy of Sciences* 115(10), (2018) 2293–2298. doi:10.1073/pnas.1720862115.
- [42] W. Kuo, N. A. Le, B. Spingler, R. H. Wenger, A. Kipar, U. Hetzel, G. Schulz, B. Müller, and V. Kurtcuoglu. “Simultaneous Three-Dimensional Vascular and Tubular Imaging of Whole Mouse Kidneys With X-ray μ CT.” *Microscopy and Microanalysis* 26(4), (2020) 731–740. doi:10.1017/S1431927620001725.
- [43] G. Schulz, T. Weitkamp, I. Zanette, F. Pfeiffer, F. Beckmann, C. David, S. Rutishauser, E. Reznikova, and B. Müller. “High-resolution tomographic imaging of a human cerebellum: Comparison of absorption and grating-based phase contrast.” *Journal of The Royal Society Interface* 7(53), (2010) 1665–1676. doi:10.1098/rsif.2010.0281.
- [44] U. Bonse and M. Hart. “An x-ray interferometer.” *Applied Physics Letters* 6(8), (1965) 155–156. doi:10.1063/1.1754212.
- [45] A. Momose. “Recent Advances in X-ray Phase Imaging.” *Japanese Journal of Applied Physics* 44(9R), (2005) 6355. doi:10.1143/JJAP.44.6355.
- [46] C. David, B. Nöhammer, H. H. Solak, and E. Ziegler. “Differential x-ray phase contrast imaging using a shearing interferometer.” *Applied Physics Letters* 81(17), (2002) 3287–3289. doi:10.1063/1.1516611.
- [47] A. Momose, S. Kawamoto, I. Koyama, Y. Hamaiishi, K. Takai, and Y. Suzuki.

- “Demonstration of X-Ray Talbot Interferometry.” *Japanese Journal of Applied Physics* 42(7B), (2003) L866. doi:10.1143/JJAP.42.L866.
- [48] T. Weitkamp, A. Diaz, C. David, F. Pfeiffer, M. Stamparoni, P. Cloetens, and E. Ziegler. “X-ray phase imaging with a grating interferometer.” *Optics Express* 13(16), (2005) 6296–6304. doi:10.1364/OPEX.13.006296.
- [49] F. Pfeiffer, T. Weitkamp, O. Bunk, and C. David. “Phase retrieval and differential phase-contrast imaging with low-brilliance X-ray sources.” *Nature Physics* 2(4), (2006) 258–261. doi:10.1038/nphys265.
- [50] S. Berujon, H. Wang, and K. Sawhney. “X-ray multimodal imaging using a random-phase object.” *Physical Review A* 86(6), (2012) 063813. doi:10.1103/PhysRevA.86.063813.
- [51] K. S. Morgan, D. M. Paganin, and K. K. W. Siu. “X-ray phase imaging with a paper analyzer.” *Applied Physics Letters* 100(12), (2012) 124102. doi:10.1063/1.3694918.
- [52] I. Zanette, T. Zhou, A. Burvall, U. Lundström, D. H. Larsson, M. Zdora, P. Thibault, F. Pfeiffer, and H. M. Hertz. “Speckle-Based X-Ray Phase-Contrast and Dark-Field Imaging with a Laboratory Source.” *Physical Review Letters* 112(25), (2014) 253903. doi:10.1103/PhysRevLett.112.253903.
- [53] M.-C. Zdora, P. Thibault, T. Zhou, F. J. Koch, J. Romell, S. Sala, A. Last, C. Rau, and I. Zanette. “X-ray Phase-Contrast Imaging and Metrology through Unified Modulated Pattern Analysis.” *Physical Review Letters* 118(20), (2017) 203903. doi:10.1103/PhysRevLett.118.203903.
- [54] A. Olivo and R. Speller. “A coded-aperture technique allowing x-ray phase contrast imaging with conventional sources.” *Applied Physics Letters* 91(7), (2007) 074106. doi:10.1063/1.2772193.
- [55] P. C. Diemoz, M. Endrizzi, C. E. Zapata, Z. D. Pešić, C. Rau, A. Bravin, I. K. Robinson, and A. Olivo. “X-Ray Phase-Contrast Imaging with Nanoradian Angular Resolution.” *Physical Review Letters* 110(13), (2013) 138105. doi:10.1103/PhysRevLett.110.138105.
- [56] E. Förster, K. Goetz, and P. Zaumseil. “Double crystal diffractometry for the characterization of targets for laser fusion experiments.” *Kristall und Technik* 15(8), (1980) 937–945. doi:10.1002/crat.19800150812.
- [57] T. J. Davis, D. Gao, T. E. Gureyev, A. W. Stevenson, and S. W. Wilkins. “Phase-contrast imaging of weakly absorbing materials using hard X-rays.” *Nature* 373(6515), (1995) 595–598. doi:10.1038/373595a0.
- [58] D. Chapman, W. Thomlinson, R. E. Johnston, D. Washburn, E. Pisano, N. Gmür, Z. Zhong, R. Menk, F. Arfelli, and D. Sayers. “Diffraction enhanced x-ray imaging.” *Physics in Medicine and Biology* 42(11), (1997) 2015–2025. doi:10.1088/0031-9155/42/11/001.
- [59] A. Snigirev, I. Snigireva, V. Kohn, S. Kuznetsov, and I. Schelokov. “On the possibilities of x-ray phase contrast microimaging by coherent high-energy synchrotron radiation.” *Review of Scientific Instruments* 66(12), (1995) 5486–5492. doi:10.1063/1.1146073.
- [60] P. Cloetens, R. Barrett, J. Baruchel, J.-P. Guigay, and M. Schlenker. “Phase

- objects in synchrotron radiation hard x-ray imaging.” *Journal of Physics D: Applied Physics* 29(1), (1996) 133–146. doi:10.1088/0022-3727/29/1/023.
- [61] K. A. Nugent, T. E. Gureyev, D. F. Cookson, D. Paganin, and Z. Barnea. “Quantitative Phase Imaging Using Hard X Rays.” *Physical Review Letters* 77(14), (1996) 2961–2964. doi:10.1103/PhysRevLett.77.2961.
- [62] S. W. Wilkins, T. E. Gureyev, D. Gao, A. Pogany, and A. W. Stevenson. “Phase-contrast imaging using polychromatic hard X-rays.” *Nature* 384(6607), (1996) 335–338. doi:10.1038/384335a0.
- [63] P. Cloetens, W. Ludwig, J. Baruchel, D. Van Dyck, J. Van Landuyt, J. P. Guigay, and M. Schlenker. “Holotomography: Quantitative phase tomography with micrometer resolution using hard synchrotron radiation x rays.” *Applied Physics Letters* 75(19), (1999) 2912–2914. doi:10.1063/1.125225.
- [64] D. Paganin, S. C. Mayo, T. E. Gureyev, P. R. Miller, and S. W. Wilkins. “Simultaneous phase and amplitude extraction from a single defocused image of a homogeneous object.” *Journal of Microscopy* 206(1), (2002) 33–40. doi:10.1046/j.1365-2818.2002.01010.x.
- [65] E. L. Dyer, W. G. Roncal, J. A. Prasad, H. L. Fernandes, D. Gürsoy, V. D. Andrade, K. Fezzaa, X. Xiao, J. T. Vogelstein, C. Jacobsen, K. P. Körding, and N. Kasthuri. “Quantifying Mesoscale Neuroanatomy Using X-Ray Microtomography.” *eNeuro* 4(5). doi:10.1523/ENEURO.0195-17.2017.
- [66] S. E. Hieber, C. Bikis, A. Khimchenko, G. Schweighauser, J. Hench, N. Chicherova, G. Schulz, and B. Müller. “Tomographic brain imaging with nucleolar detail and automatic cell counting.” *Scientific Reports* 6(1), (2016) 32156. doi:10.1038/srep32156.
- [67] M. Töpferwien, F. van der Meer, C. Stadelmann, and T. Salditt. “Three-dimensional virtual histology of human cerebellum by X-ray phase-contrast tomography.” *Proceedings of the National Academy of Sciences* 115(27), (2018) 6940–6945. doi:10.1073/pnas.1801678115.
- [68] M. Töpferwien, F. van der Meer, C. Stadelmann, and T. Salditt. “Correlative x-ray phase-contrast tomography and histology of human brain tissue affected by Alzheimer’s disease.” *NeuroImage* 210, (2020) 116523. doi:10.1016/j.neuroimage.2020.116523.
- [69] L. Massimi, I. Bukreeva, G. Santamaria, M. Fratini, A. Corbelli, F. Brun, S. Fumagalli, L. Maugeri, A. Pacureanu, P. Cloetens, N. Pieroni, F. Fiordaliso, G. Forloni, A. Uccelli, N. Kerlero de Rosbo, C. Balducci, and A. Cedola. “Exploring Alzheimer’s disease mouse brain through X-ray phase contrast tomography: From the cell to the organ.” *NeuroImage* 184, (2019) 490–495. doi:10.1016/j.neuroimage.2018.09.044.
- [70] J. Albers, S. Pacilé, M. A. Markus, M. Wiart, G. Vande Velde, G. Tromba, and C. Dullin. “X-ray-Based 3D Virtual Histology—Adding the Next Dimension to Histological Analysis.” *Molecular Imaging and Biology* 20(5), (2018) 732–741. doi:10.1007/s11307-018-1246-3.
- [71] A. Khimchenko, H. Deyhle, G. Schulz, G. Schweighauser, J. Hench, N. Chicherova, C. Bikis, S. E. Hieber, and B. Müller. “Extending two-dimensional histology into the third dimension through conven-

- tional micro computed tomography.” *NeuroImage* 139, (2016) 26–36. doi:10.1016/j.neuroimage.2016.06.005.
- [72] M. Töpperwien, A. Markus, F. Alves, and T. Salditt. “Contrast enhancement for visualizing neuronal cytoarchitecture by propagation-based x-ray phase-contrast tomography.” *NeuroImage* 199, (2019) 70–80. doi:10.1016/j.neuroimage.2019.05.043.
- [73] A. T. Kuan, J. S. Phelps, L. A. Thomas, T. M. Nguyen, J. Han, C.-L. Chen, A. W. Azevedo, J. C. Tuthill, J. Funke, P. Cloetens, A. Pacureanu, and W.-C. A. Lee. “Dense neuronal reconstruction through X-ray holographic nano-tomography.” *Nature Neuroscience* 23(12), (2020) 1637–1643. doi:10.1038/s41593-020-0704-9.
- [74] A. Khimchenko, C. Bikis, A. Pacureanu, S. E. Hieber, P. Thalmann, H. Deyhle, G. Schweighauser, J. Hench, S. Frank, M. Müller-Gerbl, G. Schulz, P. Cloetens, and B. Müller. “Hard X-Ray Nanoholotomography: Large-Scale, Label-Free, 3D Neuroimaging beyond Optical Limit.” *Advanced Science* 5(6), (2018) 1700694. doi:10.1002/advs.201700694.
- [75] M. Du, Z. Di, D. Gürsoy, R. P. Xian, Y. Kozorovitskiy, and C. Jacobsen. “Upscaling X-ray nanoimaging to macroscopic specimens.” *Journal of Applied Crystallography* 54(2), (2021) 386–401. doi:10.1107/S1600576721000194.
- [76] P. P. Mitra. “The Circuit Architecture of Whole Brains at the Mesoscopic Scale.” *Neuron* 83(6), (2014) 1273–1283. doi:10.1016/j.neuron.2014.08.055.
- [77] A. Migga, B. Müller, and G. Schulz. “Laboratory-based phase tomography with micron resolution.” In “Developments in X-Ray Tomography XIII,” volume 11840, 118400T. International Society for Optics and Photonics, 2021. doi:10.1117/12.2597926.
- [78] C. Tanner, G. Rodgers, G. Schulz, M. Osterwalder, G. Mani-Caplazi, G. Hotz, M. Scheel, T. Weitkamp, and B. Müller. “Extended-field synchrotron microtomography for non-destructive analysis of incremental lines in archeological human teeth cementum.” In “Developments in X-Ray Tomography XIII,” volume 11840, 1184019. International Society for Optics and Photonics, 2021. doi:10.1117/12.2595180.
- [79] G. Rodgers, C. Tanner, G. Schulz, A. Migga, T. Weitkamp, W. Kuo, M. Scheel, M. Osterwalder, V. Kurtcuoglu, and B. Müller. “Impact of fixation and paraffin embedding on mouse brain morphology: A synchrotron radiation-based tomography study.” In “Developments in X-Ray Tomography XIII,” volume 11840, 118400P. International Society for Optics and Photonics, 2021. doi:10.1117/12.2595144.
- [80] G. Rodgers, G. Schulz, W. Kuo, M. Scheel, V. Kurtcuoglu, T. Weitkamp, B. Müller, and C. Tanner. “Non-rigid registration to determine strain fields during mouse brain fixation and embedding.” In “Bioinspiration, Biomimetics, and Bioreplication XI,” volume 11586, 115860I. International Society for Optics and Photonics, 2021. doi:10.1117/12.2583632.
- [81] J. Engel. “Mesial Temporal Lobe Epilepsy: What Have We Learned?” *The Neuroscientist* 7(4), (2001) 340–352. doi:10.1177/107385840100700410.
- [82] B. S. Meldrum, R. A. Vigouroux, P. Rage, and J. B. Brierley. “Hippocam-

- pal lesions produced by prolonged seizures in paralyzed artificially ventilated baboons.” *Experientia* 29(5), (1973) 561–563. doi:10.1007/BF01926665.
- [83] J. Engel. “Report of the ILAE Classification Core Group.” *Epilepsia* 47(9), (2006) 1558–1568. doi:10.1111/j.1528-1167.2006.00215.x.
- [84] M. Thom. “Review: Hippocampal sclerosis in epilepsy: A neuropathology review.” *Neuropathology and Applied Neurobiology* 40(5), (2014) 520–543. doi:10.1111/nan.12150.
- [85] M. C. Walker. “Hippocampal Sclerosis: Causes and Prevention.” *Seminars in Neurology* 35(03), (2015) 193–200. doi:10.1055/s-0035-1552618.
- [86] P. Ryvlin and P. Kahane. “The hidden causes of surgery-resistant temporal lobe epilepsy: Extratemporal or temporal plus? editorial review.” *Current Opinion in Neurology* 18(2), (2005) 125–127. doi:10.1097/01.wco.0000162852.22026.6f.
- [87] A. Sierra, O. Gröhn, and A. Pitkänen. “Imaging microstructural damage and plasticity in the hippocampus during epileptogenesis.” *Neuroscience* 309, (2015) 162–172. doi:10.1016/j.neuroscience.2015.04.054.
- [88] P. Janz, N. Schwaderlapp, K. Heining, U. Häussler, J. G. Korvink, D. von Elverfeldt, J. Hennig, U. Egert, P. LeVan, and C. A. Haas. “Early tissue damage and microstructural reorganization predict disease severity in experimental epilepsy.” *eLife* 6, (2017) e25742. doi:10.7554/eLife.25742.
- [89] E. Ferrante and N. Paragios. “Slice-to-volume medical image registration: A survey.” *Medical Image Analysis* 39, (2017) 101–123. doi:10.1016/j.media.2017.04.010.
- [90] J. Kowalski, M. Geuting, S. Paul, S. Dieni, J. Laurens, S. Zhao, A. Drakew, C. A. Haas, M. Frotscher, and I. Vida. “Proper Layering Is Important for Precisely Timed Activation of Hippocampal Mossy Cells.” *Cerebral Cortex* 20(9), (2010) 2043–2054. doi:10.1093/cercor/bhp267.
- [91] M. Marx, C. Haas, and U. Häussler. “Differential vulnerability of interneurons in the epileptic hippocampus.” *Frontiers in Cellular Neuroscience* 7, (2013) 167. doi:10.3389/fncel.2013.00167.
- [92] U. Häussler, L. Bielefeld, U. P. Froriep, J. Wolfart, and C. A. Haas. “Septotemporal Position in the Hippocampal Formation Determines Epileptic and Neurogenic Activity in Temporal Lobe Epilepsy.” *Cerebral Cortex* 22(1), (2012) 26–36. doi:10.1093/cercor/bhr054.
- [93] G. Rodgers, W. Kuo, G. Schulz, M. Scheel, A. Migga, C. Bikis, C. Tanner, V. Kurtcuoglu, T. Weitkamp, and B. Müller. “Virtual histology of an entire mouse brain from formalin fixation to paraffin embedding. Part 1: Data acquisition, anatomical feature segmentation, tracking global volume and density changes.” *Journal of Neuroscience Methods* 364, (2021) 109354. doi:10.1016/j.jneumeth.2021.109354.
- [94] G. Rodgers, C. Tanner, G. Schulz, A. Migga, W. Kuo, C. Bikis, M. Scheel, V. Kurtcuoglu, T. Weitkamp, and B. Müller. “Virtual histology of an entire mouse brain from formalin fixation to paraffin embedding. Part 2: Volumetric strain fields and local contrast changes.” *Journal of Neuroscience Methods* 365, (2022) 109385. doi:10.1016/j.jneumeth.2021.109385.

-
- [95] M. Lévesque and M. Avoli. “The kainic acid model of temporal lobe epilepsy.” *Neuroscience & Biobehavioral Reviews* 37(10, Part 2), (2013) 2887–2899. doi:10.1016/j.neubiorev.2013.10.011.
- [96] C. Heinrich, N. Nitta, A. Flubacher, M. Müller, A. Fahrner, M. Kirsch, T. Freiman, F. Suzuki, A. Depaulis, M. Frotscher, and C. A. Haas. “Reelin Deficiency and Displacement of Mature Neurons, But Not Neurogenesis, Underlie the Formation of Granule Cell Dispersion in the Epileptic Hippocampus.” *Journal of Neuroscience* 26(17), (2006) 4701–4713. doi:10.1523/JNEUROSCI.5516-05.2006.
- [97] P. Janz, S. Savanthrapadian, U. Häussler, A. Kiliyas, S. Nestel, O. Kretz, M. Kirsch, M. Bartos, U. Egert, and C. A. Haas. “Synaptic Remodeling of Entorhinal Input Contributes to an Aberrant Hippocampal Network in Temporal Lobe Epilepsy.” *Cerebral Cortex* 27(3), (2017) 2348–2364. doi:10.1093/cercor/bhw093.
- [98] C. Rau, T. Weitkamp, A. Snigirev, C. G. Schroer, J. Tümmeler, and B. Lengeler. “Recent developments in hard X-ray tomography.” *Nuclear Instruments and Methods in Physics Research Section A: Accelerators, Spectrometers, Detectors and Associated Equipment* 467-468, (2001) 929–931. doi:10.1016/S0168-9002(01)00528-9.
- [99] P. Thalmann, C. Bikis, G. Schulz, P. Paleo, A. Mirone, A. Rack, S. Siegrist, E. Cörek, J. Huwyler, and B. Müller. “Removing ring artefacts from synchrotron radiation-based hard x-ray tomography data.” In “Developments in X-Ray Tomography XI,” volume 10391, 1039114. International Society for Optics and Photonics, 2017. doi:10.1117/12.2274236.
- [100] D. Shamonin, E. Bron, B. Lelieveldt, M. Smits, S. Klein, and M. Staring. “Fast Parallel Image Registration on CPU and GPU for Diagnostic Classification of Alzheimer’s Disease.” *Frontiers in Neuroinformatics* 7, (2014) 50. doi:10.3389/fninf.2013.00050.
- [101] S. Klein, M. Staring, K. Murphy, M. A. Viergever, and J. P. W. Pluim. “Elastix: A Toolbox for Intensity-Based Medical Image Registration.” *IEEE Transactions on Medical Imaging* 29(1), (2010) 196–205. doi:10.1109/TMI.2009.2035616.
- [102] E. S. Lein, M. J. Hawrylycz, N. Ao, M. Ayres, A. Bensinger, A. Bernard, A. F. Boe, M. S. Boguski, K. S. Brockway, E. J. Byrnes, L. Chen, L. Chen, T.-M. Chen, M. Chi Chin, J. Chong, B. E. Crook, A. Czaplinska, C. N. Dang, S. Datta, N. R. Dee, A. L. Desaki, T. Desta, E. Diep, T. A. Dolbeare, M. J. Donelan, H.-W. Dong, J. G. Dougherty, B. J. Duncan, A. J. Ebbert, G. Eichele, L. K. Estin, C. Faber, B. A. Facer, R. Fields, S. R. Fischer, T. P. Fliss, C. Frensley, S. N. Gates, K. J. Glattfelder, K. R. Halverson, M. R. Hart, J. G. Hohmann, M. P. Howell, D. P. Jeung, R. A. Johnson, P. T. Karr, R. Kawal, J. M. Kidney, R. H. Knapik, C. L. Kuan, J. H. Lake, A. R. Laramee, K. D. Larsen, C. Lau, T. A. Lemon, A. J. Liang, Y. Liu, L. T. Luong, J. Michaels, J. J. Morgan, R. J. Morgan, M. T. Mortrud, N. F. Mosqueda, L. L. Ng, R. Ng, G. J. Orta, C. C. Overly, T. H. Pak, S. E. Parry, S. D. Pathak, O. C. Pearson, R. B. Puchalski, Z. L. Riley, H. R. Rockett, S. A. Rowland, J. J. Royall, M. J. Ruiz, N. R. Sarno, K. Schaffnit, N. V. Shapovalova, T. Sivisay,

- C. R. Slaughterbeck, S. C. Smith, K. A. Smith, B. I. Smith, A. J. Sodt, N. N. Stewart, K.-R. Stumpf, S. M. Sunkin, M. Sutram, A. Tam, C. D. Teemer, C. Thaller, C. L. Thompson, L. R. Varnam, A. Visel, R. M. Whitlock, P. E. Wohnoutka, C. K. Wolkey, V. Y. Wong, M. Wood, M. B. Yaylaoglu, R. C. Young, B. L. Youngstrom, X. Feng Yuan, B. Zhang, T. A. Zwingman, and A. R. Jones. “Genome-wide atlas of gene expression in the adult mouse brain.” *Nature* 445(7124), (2007) 168–176. doi:10.1038/nature05453.
- [103] P. A. Yushkevich, J. Piven, H. C. Hazlett, R. G. Smith, S. Ho, J. C. Gee, and G. Gerig. “User-guided 3D active contour segmentation of anatomical structures: Significantly improved efficiency and reliability.” *NeuroImage* 31(3), (2006) 1116–1128. doi:10.1016/j.neuroimage.2006.01.015.
- [104] P. Thurner, F. Beckmann, and B. Müller. “An optimization procedure for spatial and density resolution in hard X-ray micro-computed tomography.” *Nuclear Instruments and Methods in Physics Research Section B: Beam Interactions with Materials and Atoms* 225(4), (2004) 599–603. doi:10.1016/j.nimb.2004.05.027.
- [105] G. Rodgers, G. Schulz, H. Deyhle, W. Kuo, C. Rau, T. Weitkamp, and B. Müller. “Optimizing contrast and spatial resolution in hard x-ray tomography of medically relevant tissues.” *Applied Physics Letters* 116(2), (2020) 023702. doi:10.1063/1.5133742.
- [106] T. J. LaGrow, M. G. Moore, J. A. Prasad, M. A. Davenport, and E. L. Dyer. “Approximating Cellular Densities from High-Resolution Neuroanatomical Imaging Data.” In “2018 40th Annual International Conference of the IEEE Engineering in Medicine and Biology Society (EMBC),” 1–4. IEEE, Honolulu, HI, 2018. doi:10.1109/EMBC.2018.8512220.
- [107] J. A. Prasad, A. H. Balwani, E. C. Johnson, J. D. Miano, V. Sampathkumar, V. De Andrade, K. Fezzaa, M. Du, R. Vescovi, C. Jacobsen, K. P. Kording, D. Gürsoy, W. Gray Roncal, N. Kasthuri, and E. L. Dyer. “A three-dimensional thalamocortical dataset for characterizing brain heterogeneity.” *Scientific Data* 7(1), (2020) 358. doi:10.1038/s41597-020-00692-y.
- [108] A. Balwani, J. Miano, R. Liu, L. Kitchell, J. A. Prasad, E. C. Johnson, W. Gray-Roncal, and E. L. Dyer. “Multi-Scale Modeling of Neural Structure in X-Ray Imagery.” In “2021 IEEE International Conference on Image Processing (ICIP),” 141–145. 2021. doi:10.1109/ICIP42928.2021.9506174.
- [109] Y. Ma, P. R. Hof, S. C. Grant, S. J. Blackband, R. Bennett, L. Slatest, M. D. McGuigan, and H. Benveniste. “A three-dimensional digital atlas database of the adult C57BL/6J mouse brain by magnetic resonance microscopy.” *Neuroscience* 135(4), (2005) 1203–1215. doi:10.1016/j.neuroscience.2005.07.014.
- [110] R. Vescovi, M. Du, V. de Andrade, W. Scullin, D. Gürsoy, and C. Jacobsen. “TomoSaiC: Efficient acquisition and reconstruction of teravoxel tomography data using limited-size synchrotron X-ray beams.” *Journal of Synchrotron Radiation* 25(5), (2018) 1478–1489. doi:10.1107/S1600577518010093.
- [111] M. Du, R. Vescovi, K. Fezzaa, C. Jacobsen, and D. Gürsoy. “X-ray tomography of extended objects: A comparison of data acquisition approaches.” *JOSA A* 35(11), (2018) 1871–1879. doi:10.1364/JOSAA.35.001871.

-
- [112] A. Miettinen, I. V. Oikonomidis, A. Bonnin, and M. Stampanoni. “NRStitcher: Non-rigid stitching of terapixel-scale volumetric images.” *Bioinformatics* 35(24), (2019) 5290–5297. doi:10.1093/bioinformatics/btz423.
- [113] N. T. Vo, R. C. Atwood, M. Drakopoulos, and T. Connolley. “Data processing methods and data acquisition for samples larger than the field of view in parallel-beam tomography.” *Optics Express* 29(12), (2021) 17849–17874. doi:10.1364/OE.418448.
- [114] S. Foxley, V. Sampathkumar, V. De Andrade, S. Trinkle, A. Sorokina, K. Norwood, P. La Riviere, and N. Kasthuri. “Multi-modal imaging of a single mouse brain over five orders of magnitude of resolution.” *NeuroImage* 238, (2021) 118250. doi:10.1016/j.neuroimage.2021.118250.
- [115] T. Weitkamp, M. Scheel, J. L. Giorgetta, V. Joyet, V. L. Roux, G. Cauchon, T. Moreno, F. Polack, A. Thompson, and J. P. Samama. “The tomography beamlineANATOMIXat Synchrotron SOLEIL.” *Journal of Physics: Conference Series* 849, (2017) 012037. doi:10.1088/1742-6596/849/1/012037.
- [116] A. Kyrieleis, M. Ibson, V. Titarenko, and P. J. Withers. “Image stitching strategies for tomographic imaging of large objects at high resolution at synchrotron sources.” *Nuclear Instruments and Methods in Physics Research Section A: Accelerators, Spectrometers, Detectors and Associated Equipment* 607(3), (2009) 677–684. doi:10.1016/j.nima.2009.06.030.
- [117] A. Miettinen, I. V. Oikonomidis, A. Bonnin, and M. Stampanoni. “NRStitcher: Non-rigid stitching of terapixel-scale volumetric images.” *Bioinformatics* 35(24), (2019) 5290–5297. doi:10.1093/bioinformatics/btz423.
- [118] R. F. C. Vescovi, M. B. Cardoso, and E. X. Miqueles. “Radiography registration for mosaic tomography.” *Journal of Synchrotron Radiation* 24(3), (2017) 686–694. doi:10.1107/S1600577517001953.
- [119] A. Kyrieleis, V. Titarenko, M. Ibson, T. Connolley, and P. J. Withers. “Region-of-interest tomography using filtered backprojection: Assessing the practical limits.” *Journal of Microscopy* 241(1), (2011) 69–82. doi:10.1111/j.1365-2818.2010.03408.x.
- [120] J. C. da Silva, M. Guizar-Sicairos, M. Holler, A. Diaz, J. A. van Bokhoven, O. Bunk, and A. Menzel. “Quantitative region-of-interest tomography using variable field of view.” *Optics Express* 26(13), (2018) 16752–16768. doi:10.1364/OE.26.016752.
- [121] A.-L. Robisch, J. Frohn, and T. Salditt. “Iterative micro-tomography of biopsy samples from truncated projections with quantitative gray values.” *Physics in Medicine & Biology* 65(23), (2020) 235034. doi:10.1088/1361-6560/abc22f.
- [122] K. Desjardins, A. Carcy, J.-L. Giorgetta, C. Meneglier, M. Scheel, and T. Weitkamp. “Design of Indirect X-Ray Detectors for Tomography on the Anatomix Beamline.” In “Mechanical Eng.~Design of Synchrotron Radiation Equipment and Instrumentation (MEDSI’18), Paris, France, 25-29 June 2018,” 355–357. JACOW Publishing, Geneva, Switzerland, 2018. doi:10.18429/JACoW-MEDSI2018-THPH09.
- [123] T. Weitkamp, D. Haas, D. Wegrzynek, and A. Rack. “ANKAphase: Software for single-distance phase retrieval from inline X-ray phase-contrast

- radiographs.” *Journal of Synchrotron Radiation* 18(4), (2011) 617–629. doi:10.1107/S0909049511002895.
- [124] D. Gürsoy, F. De Carlo, X. Xiao, and C. Jacobsen. “TomoPy: A framework for the analysis of synchrotron tomographic data.” *Journal of Synchrotron Radiation* 21(5), (2014) 1188–1193. doi:10.1107/S1600577514013939.
- [125] F. Marone and M. Stampanoni. “Regridding reconstruction algorithm for real-time tomographic imaging.” *Journal of Synchrotron Radiation* 19(6), (2012) 1029–1037. doi:10.1107/S0909049512032864.
- [126] A. Mirone, E. Brun, E. Gouillart, P. Tafforeau, and J. Kieffer. “The PyHST2 hybrid distributed code for high speed tomographic reconstruction with iterative reconstruction and a priori knowledge capabilities.” *Nuclear Instruments and Methods in Physics Research Section B: Beam Interactions with Materials and Atoms* 324, (2014) 41–48. doi:10.1016/j.nimb.2013.09.030.
- [127] B. Münch, P. Trtik, F. Marone, and M. Stampanoni. “Stripe and ring artifact removal with combined wavelet — Fourier filtering.” *Optics Express* 17(10), (2009) 8567–8591. doi:10.1364/OE.17.008567.
- [128] N. T. Vo, R. C. Atwood, and M. Drakopoulos. “Superior techniques for eliminating ring artifacts in X-ray micro-tomography.” *Optics Express* 26(22), (2018) 28396–28412. doi:10.1364/OE.26.028396.
- [129] W. Kuo, D. Rossinelli, G. Schulz, R. H. Wenger, S. Hieber, B. Müller, and V. Kurtcuoglu. “Terabyte-scale supervised 3D training and benchmarking dataset of the mouse kidney.” *arXiv:2108.02226 [physics, q-bio]* .

Acknowledgments

Firstly, I would like to thank Bert Müller, who I have known for nearly five years and who has supported me the entire time. I came for a lecture, then took a semester project, then stayed for a Master's thesis, and now the PhD, so I can safely say that I have learned a lot from you. Thank you for always being available, for giving me so many opportunities, and for providing me with both guidance and freedom.

Thank you to Georg Schulz, who introduced me to the field and has given me valuable supervision since I first arrived at the BMC. I have learned a lot from you over the years. Thanks for all of the weekends and night shifts together at beamtimes and for all of the last minute deadlines we managed to pull off. It has been great to work with you all this time.

Thank you to Christine Tanner, who arrived at the BMC not a minute too soon. Thank you for your valuable scientific input, you have elevated all of our shared projects. Thanks also for your almost constant availability and for your guidance. It has been a pleasure to work with you.

Thank you to Melissa Osterwalder, who has helped make our team so rewarding. Thank you to Christos Bikis, who gave me the opportunity to work on his projects from the beginning and who has continued to share his ideas and projects with me. Thank you to Hans Deyhle, who only overlapped with me at the beginning but nonetheless gave valuable supervision in the early days of my PhD. Thank you to Alexandra Migga, who provided helpful discussion from a new perspective, I hope I did not wear you out with segmentations. Thanks also to Bekim Osmani, Tino Töpfer, Thomas Pfohl, Jeannette von Jackowski, Guido Sigron, Sofiya Matviyukiv, Matej Siketanc, Marzia Buscema, Prabitha Urwyler, and many more who I overlapped with during my time at the BMC. I enjoyed many coffees, lunches, dinners, kicker games, beers, *etc.* with you all.

I would also like to thank Willy Kuo for his support with numerous experiments and at many beamtimes. Your input has been very valuable across many projects. Thank you to Marta Girona-Alarcón, who I began working with towards the end of my PhD through a lucky coincidence, it has been fun and motivating to work together. Thanks also to Vartan Kurtcuoglu for his guidance and for welcoming me into his collaborations.

Thank you to Timm Weitkamp for your valuable scientific input across multiple shared projects. Thanks also for all of the support during our experiments at ANATOMIX. Thanks also to Mario Scheel, whose expertise was critical for the success of our beamtimes at ANATOMIX. It has been a pleasure to work with both of you.

Thanks to Jan Stephan Bolten and Jörg Huwyler for their support and collaboration.

I would also like to thank Prof. Dr. Britta Engelhardt and her team at the Theodor Koch Institute, University of Bern for the inspiring scientific discussion and fruitful collaboration.

I would like to thank Christoph Rau, Shashidara Marathe, and everyone at the I13 Imaging beamline for their support during our beamtimes.

Thank you to Felix Beckmann and Julian Moosmann for valuable discussions and support during experiments at DESY.

I would like to thank Ernst Meyer for serving as a co-referee and Julia Herzen for serving as an external expert.

Thank you to Christine Tanner, Melissa Osterwalder, Georg Schulz, and Bert Müller for proof-reading sections of this thesis. Thanks to Bert Müller for German translations.

Thank you to Hsin-Zon Tsai, whose mentoring and support at Berkeley helped me immensely to reach where I am today.

I would also like to thank all of the family and friends who have helped in small and big ways over the past few years. Thanks to Miguel Silva Toledo for his friendship and the occasional mattress to sleep on during trips to Hamburg. Thanks to the entire Heinzer-D'Intino family for welcoming me and giving me a local family here in Switzerland. Thanks to my parents, Anne and Kevin, whose love and support made all of this possible in the first place. Finally, I want to thank Lisa for being there with me the whole time. I couldn't have done it without you!

Curriculum Vitae

Personal Information

Family Name: Rodgers
First Name: Griffin
Citizenship: United States of America
Date of Birth: 11.05.1994

Education

- 2019 - 2021** Ph.D. Candidate in Physics
University of Basel
Thesis: Hard X-ray microtomography for virtual histology of the brain with cellular resolution
Advisors: Prof. Dr. Bert Müller
Prof. Dr. Ernst Meyer
- 2016 - 2018** M.Sc. Physics
ETH Zürich
Thesis: Developments in Hard X-ray Phase Contrast Imaging for Biomedical Studies
Advisors: Prof. Dr. Bert Müller
Prof. Dr. Tony Lomax
- 2012 - 2015** B.A. Physics
University of California, Berkeley

Research

- 2017 - 2021** Biomaterials Science Center
Department of Biomedical Engineering, University of Basel
- Ph.D. thesis
- Intern
- M.Sc. thesis
- Semester project
- 2013 - 2016** Crommie Group
Department of Physics, University of California, Berkeley
- Summer undergraduate research fellowship
- Undergraduate research apprenticeship program
- Undergraduate research assistant